Scanning Probe Microscopy—Principle of Operation, Instrumentation, and Probes

2

Bharat Bhushan and Othmar Marti

Abstract

Since the introduction of the Scanning Tunneling Microscope (STM) in 1981 and Atomic Force Microscope (AFM) in 1985, many variations of probe-based microscopies, referred to as Scanning Probe Microscopes (SPM), have been developed. While the pure imaging capabilities of SPM techniques are dominated by the application of these methods at their early development stages, the physics of probe-sample interactions and the quantitative analyses of tribological, electronic, magnetic, biological, and chemical surfaces have now become of increasing interest. In this chapter, we introduce various STM and AFM designs, various operating modes, various probes (tips), and AFM instrumentation and analyses.

Keywords

Scanning probe microscopy · Atomic force microscopy · Scanning tunneling microscopy · Friction force microscopy · Electrical properties · Mechanical properties · Nanotribology · Nanomechanics

2.1 Introduction

The Scanning Tunneling Microscope (STM) developed by Dr. Gerd Binnig and his colleagues in 1981 at the IBM Zurich Research Laboratory, Rueschlikon, Switzerland, is the first instrument capable of directly obtaining three-dimensional (3D) images of solid surfaces with atomic resolution (Binnig et al. 1982). G. Binnig and H. Rohrer received a Nobel Prize in Physics in 1986 for their discovery. STMs can only be used to study surfaces that are electrically conductive to

B. Bhushan (✉)
Nanoprobe Laboratory for Bio- and Nanotechnology and Biomimetics, The Ohio State University, 201 W. 19th Ave., W390 Scott Laboratory, Columbus, OH 43210, USA
e-mail: Bhushan.2@osu.edu

O. Marti
Abteilung Experimentelle Physik, Universitaet Ulm, Albert-Einstein-Allee 11, 89069 Ulm, Germany
e-mail: othmar.marti@uni-ulm.de

B. Bhushan (ed.), *Nanotribology and Nanomechanics*,
DOI 10.1007/978-3-319-51433-8_2

some degree. Based on their design of the STM, Binnig et al. developed in 1985 an Atomic Force Microscope (AFM) to measure ultrasmall forces (less than 1 μN) present between the AFM tip surface and the sample surface (Binnig et al. 1986; also see Binnig et al. 1987). AFMs can be used for measurement of all engineering surfaces that may be either electrically conductive or insulating. AFM has become a popular surface profiler for topographic and normal force measurements on the micro to nanoscale.

AFMs have been modified in order to measure both normal and lateral forces, and are called Lateral Force Microscope (LFM) or Friction Force Microscope (FFM) (Mate et al. 1987; Erlandsson et al. 1988; Marti et al. 1990; Meyer and Amer 1990b; Bhushan and Ruan 1994; Bhushan et al. 1995; Bhushan 1999a, 2011). FFMs further have been modified to measure lateral forces in two orthogonal directions (Fujisawa et al. 1994a, b; Grafstrom et al. 1994; Overney et al. 1994; Warmack et al. 1994). A number of researchers have continued to improve the AFM/FFM designs and used them to measure adhesion and friction of solid and liquid surfaces on micro- and nanoscales (Burnham et al. 1990, 1991; Frisbie et al. 1994; Bhushan et al. 1995; Koinkar and Bhushan 1996; Scherer et al. 1997, 1999; Bhushan and Sundararajan 1998; Krotil et al. 1999; Bhushan and Dandavate 2000; Bhushan 1997, 1999a, 2001a, b, 2005, 2008, 2011, 2013a, b; Reinstaedtler et al. 2003). AFMs have been used for scratching, wear, and measurements of elastic/plastic mechanical properties (such as indentation hardness and modulus of elasticity) (Burnham and Colton 1989; Maivald et al. 1991; Bhushan et al. 1994, 1995, 1996; Bhushan and Koinkar 1994; DeVecchio and Bhushan 1997; Scherer et al. 1997; Bhushan and Sundararajan 1998; Bhushan 1997, 1999a, b, 2001a, b, c, 2005, 2008, 2011, 2013a, b; Amelio et al. 2001; Bhushan and Qi 2003; Kasai et al. 2004; Reinstaedtler et al. 2005).

AFMs have been used for manipulation of individual atoms of Xenon (Eigler and Schweizer 1990), molecules (Weisenhorn et al. 1990), silicon surfaces (Lyo and Avouris 1991), and polymer surfaces (Leung and Goh 1992). STMs have been used for formation of nanofeatures by localized heating or by inducing chemical reactions under the STM tip (Abraham et al. 1986; Silver et al. 1987; Kobayashi et al. 1993) and nanomachining (Parkinson 1990). AFMs have been used for nanofabrication (Majumdar et al. 1992; Bhushan et al. 1994; Bhushan 1995, 1999a; Tsau et al. 1994) and nanomachining (Delawski and Parkinson 1992).

STMs and AFMs are used at extreme magnifications ranging from 10^3 to $10^9\times$ in x, y, and z directions for imaging macro to atomic dimensions with high resolution information and for spectroscopy. These instruments can be used in any environment such as ambient air (Binnig et al. 1986; Bhushan and Blackman 1991), various gases (Burnham et al. 1990), liquid (Marti et al. 1987; Drake et al. 1989; Binggeli et al. 1993), vacuum (Binnig et al. 1982; Meyer and Amer 1988), low temperatures (lower than about 100 K) (Coombs and Pethica 1986; Kirk et al. 1988; Giessibl et al. 1991; Albrecht et al. 1992; Hug et al. 1993), and high temperatures (Basire and Ivanov 2000; Liu and Bhushan 2002). Imaging in liquid allows the study of live biological samples and also eliminates water capillary forces present in ambient air present at the tip-sample interface. Low temperature (liquid helium temperatures) imaging is useful for the study of biological and organic materials and the study of low-temperature phenomena such as superconductivity or charge-density waves. Low-temperature operation is also advantageous for high-sensitivity force mapping due to the reduction in thermal vibration. STMs and AFMs also have been used to image liquids such as liquid crystals and lubricant molecules on graphite surfaces (Foster and Frommer 1988; Smith et al. 1989, 1990; Andoh et al. 1992).

The pure imaging capabilities of variations of probe-based microscope techniques, referred to as Scanning Probe Microscopy (SPM), have dominated the application of these methods at their early development stages. However, the physics and chemistry of probe-sample interactions and the quantitative analyses of tribological, electronic, magnetic, biological, and

chemical surfaces now have become of increasing interest. Nanoscale science and technology are strongly driven by SPMs, which allow investigation and manipulation of surfaces down to the atomic scale. With growing understanding of the underlying interaction mechanisms, SPMs have found application in many fields outside basic research fields. In addition, various derivatives of all these methods have been developed for special applications, some of them targeting far beyond microscopy.

A family of instruments based on STMs and AFMs, SPMs have been developed for various applications of scientific and industrial interest. These include STM, AFM, FFM (or LFM), scanning electrostatic force microscopy (SEFM) (Martin et al. 1987; Stern et al. 1988), scanning force acoustic microscopy (SFAM) [or atomic force acoustic microscopy (AFAM)] (Yamanaka et al. 1994; Yamanaka and Tomita 1995; Rabe et al. 1996; Scherer et al. 1997, 1999; Amelio et al. 2001; Reinstaedtler et al. 2005), scanning magnetic microscopy (SMM) [or magnetic force microscopy (MFM)] (Martin and Wickramasinghe 1987; Rugar et al. 1990; Schoenenberger and Alvarado 1990; Hartmann 1999; Avila and Bhushan 2010), scanning near field optical microscopy (SNOM) (Pohl et al. 1984; Betzig et al. 1991, 1992; Barbara et al. 1999), scanning thermal microscopy (SThM) (Williams and Wickramasinghe 1986, 1990; Majumdar 1999), scanning electrochemical microscopy (SEcM) (Husser et al. 1989), scanning Kelvin Probe microscopy (SKPM) (Martin et al. 1988; Nonnenmacher et al. 1991; Weaver and Abraham 1991; DeVecchio and Bhushan 1998; Bhushan and Goldade 2000), scanning chemical potential microscopy (SCPM) (Williams and Wickramasighe 1990), scanning ion conductance microscopy (SICM) (Hansma et al. 1989; Prater et al. 1991), and scanning capacitance microscopy (SCM) (Matey and Blanc 1985; Martin et al. 1988; Williams 1999; Lee et al. 2002). The subfamily of instruments that measure forces (e.g., AFM, FFM, SEFM, SFAM, and SMM) also are referred to as scanning force microscopes (SFM). Although these instruments offer atomic resolution and are ideal for basic research, they are most often used for cutting edge industrial applications that do not require atomic resolution.

Commercial production of SPMs started with STM in 1987 and AFM in 1989 by Digital Instruments Inc. (now Bruker Instruments. Inc.). For comparisons of SPMs with other microscopes, see Table 2.1 (Bruker Instruments, Inc.). Numbers of these instruments are equally divided into U.S., Japan, and Europe with industry/university and Government lab splits of about 50/50, 70/30, and 30/70, respectively. It is clear that research and industrial applications of SPMs are rapidly expanding. For various examples, see Bhushan et al. (2004, 2007, 2008), Bhushan and Fuchs (2006, 2007, 2009), Bhushan and Kawata (2007), Fuchs and Bhushan (2010), Bhushan (2010–2013, 2011).

This chapter presents an overview of STM and AFM with various operating modes and various probes (tips) used in these instruments. Then, details on AFM instrumentation and analyses are given.

Table 2.1 Comparison of various conventional microscopes with SPMs in 2015

	Optical	SEM/TEM	Confocal	SPM
Magnification	10^3	10^7	10^4	10^9
Instrument price (U.S. $)	~$20 k	~$500 k	~$60 k	~$150 k
Technology age	200 years	50 years	30 years	30 years
Applications	Ubiquitous	Science & technology	New & unfolding	Science & technology
Approximate market 2015	$2 B	$1.5 B	$400 M	$600 M

2.2 Scanning Tunneling Microscope

The principle of electron tunneling was proposed by Giaever (1960). He proposed that if an electrical potential difference is applied to two metals separated by a thin insulating film, a current will flow across the barrier because of the ability of electrons to penetrate it. To be able to measure this tunneling current, the two metals must be spaced no more than 10 nm apart. Binnig et al. (1982) introduced vacuum tunneling combined with lateral scanning. The vacuum provides the ideal barrier for tunneling. The lateral scanning allows surface imaging with exquisite resolution —lateral less than 1 nm and vertical less than 0.1 nm—sufficient to define the position of single atoms. The very high vertical resolution is obtained because the tunneling current varies exponentially with the distance between the metal tip and the scanned surface acting as two electrodes. Typically, tunneling current decreases by a factor of 2 as the separation is increased by 0.2 nm. Very high lateral resolution depends upon the sharp tips. Binnig et al. (1982) overcame two key obstacles for damping external vibrations and for moving the tunneling probe in close proximity to the sample. Their instrument is called the scanning tunneling microscope (STM). Today's STMs can be used in the ambient environment for atomic-scale image of surfaces. Excellent reviews on this subject are presented by Hansma and Tersoff (1987), Sarid and Elings (1991), Durig et al. (1992); Frommer (1992), Guntherodt and Wiesendanger (1992), Wiesendanger and Guntherodt (1992), Bonnell (1993), Marti and Amrein (1993), Stroscio and Kaiser (1993), and Guntherodt et al. (1995).

The principle of STM is straightforward. A sharp metal tip (one electrode of the tunnel junction) is brought close enough (0.3–1 nm) to the surface to be investigated (second electrode) that, at a convenient operating voltage (10 mV–1 V), the tunneling current varies from 0.2 to 10 nA, which is measurable. The tip is scanned over a surface at a distance of 0.3–1 nm, while the tunneling current between it and the surface is sensed. The STM can be operated in either the constant current mode or the constant height mode, Fig. 2.1. The left-hand column of Fig. 2.1 shows the basic constant current mode of operation. A feedback network changes the height of the tip z to keep the current constant. The displacement of the tip given by the voltage applied to the piezoelectric drives then yields a topographic map of the surface. Alternatively, in the constant height mode, a metal tip can be scanned across a surface at nearly constant height and constant voltage while the current is monitored, as shown in the right-hand column of Fig. 2.1. In this case, the feedback network responds only rapidly enough to keep the average current constant. The constant current mode is used generally for atomic-scale images. This mode is not practical for rough surfaces. A three-dimensional picture [z(x, y)] of a surface consists of multiple scans [z(x)] displayed laterally from each other in the y direction. It should be noted that if different atomic species are present in a sample, the different atomic species within a sample may produce different tunneling currents for a given bias voltage. Thus, the height data may not be a direct representation of the topography of the surface of the sample.

2.2.1 Binnig et al.'s Design

Figure 2.2 shows a schematic of one of Binnig and Rohrer's designs for operation in ultrahigh vacuum (Binnig et al. 1982; Binnig and Rohrer 1983). The metal tip was fixed to rectangular piezodrives P_x, P_y, and P_z made out of commercial piezoceramic material for scanning. The sample is mounted on either superconducting magnetic levitation or two-stage spring system to achieve a stability of the gap width of about 0.02 nm. The tunnel current J_T is a sensitive function of the gap width d that is $J_T \propto V_T \exp(-A\phi^{1/2}d)$, where V_T is the bias voltage, ϕ is the average barrier height (work function) and the constant $A = 1.025\ eV^{-1/2}\ Å^{-1}$. With a work function of a few eV, J_T changes by an order of magnitude for every angstrom change of d. If the current is kept constant to within, for example, 2%, then the gap d remains constant to within 1 pm. For operation in the constant current

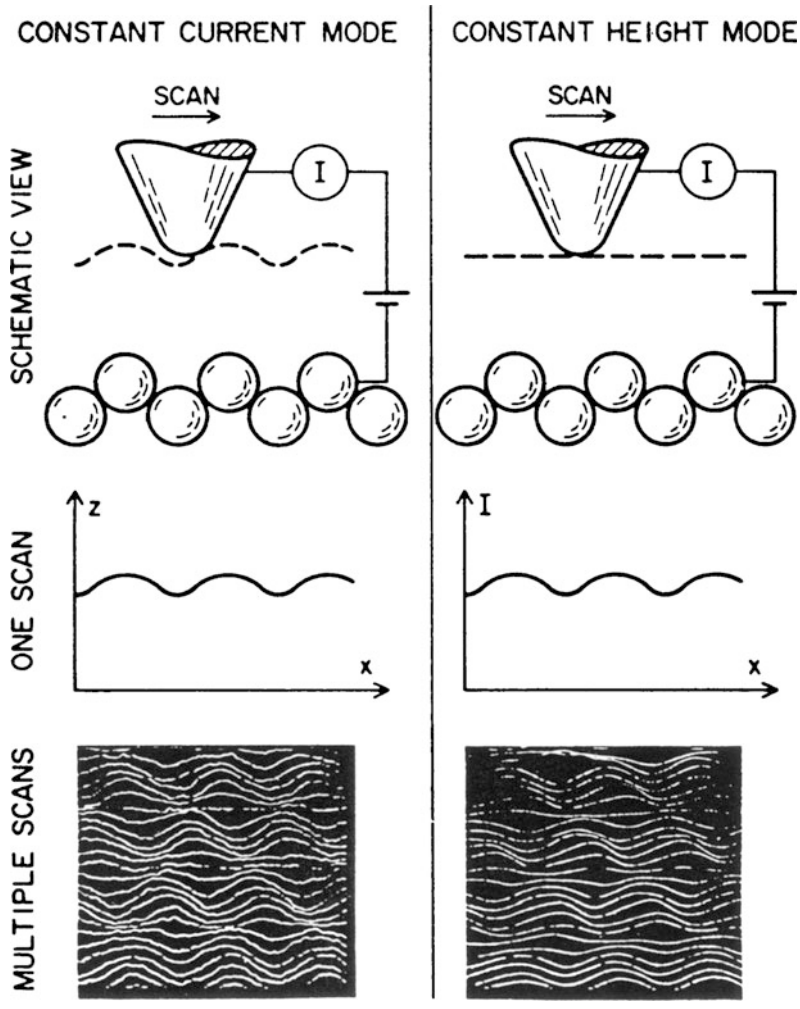

Fig. 2.1 STM can be operated in either the constant-current or the constant-height mode. The images are of graphite in air (Hansma and Tersoff 1987)

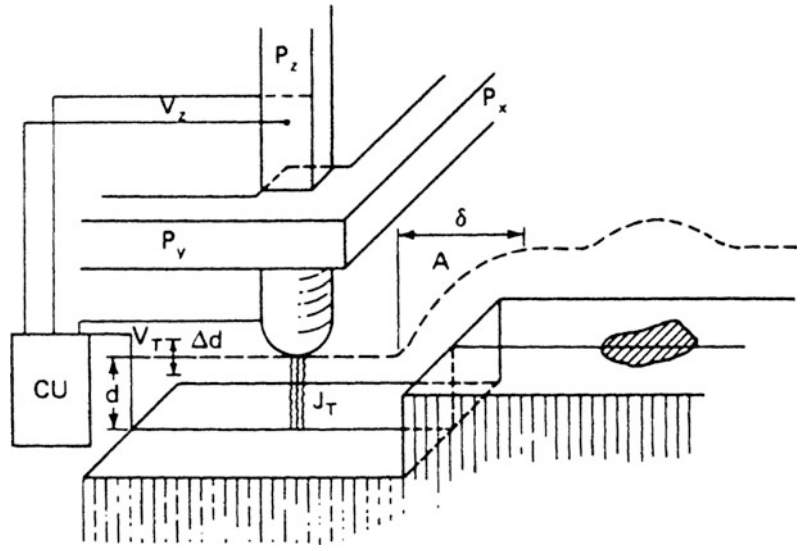

Fig. 2.2 Principle of operation of the STM made by Binnig and Rohrer (1983)

mode, the control unit (CU) applies a voltage V_z to the piezo P_z such that J_T remains constant when scanning the tip with P_y and P_x over the surface. At a constant work function ϕ, $V_z(V_x, V_y)$ yields the roughness of the surface z(x, y) directly, as illustrated at a surface step at A. Smearing the step, δ (lateral resolution) is on the order of $(R)^{1/2}$, where R is the radius of the curvature of the tip. Thus, a lateral resolution of about 2 nm requires tip radii on the order of 10 nm. A 1-mm-diameter solid rod ground at one end at roughly 90° yields overall tip radii of only a few hundred nm, but with closest protrusion of rather sharp microtips on the relatively dull end yields a lateral resolution of about 2 nm. In situ sharpening of the tips by gently touching the surface brings the resolution down to the 1-nm range; by applying high fields (on the order of 10^8 V/cm). For example, applications of high field for half an hour, resolutions considerably below 1 nm could be reached. Most experiments were done with tungsten wires either ground or etched to a radius typically in the range of 0.1–10 μm. In some cases, in situ processing of the tips was done for further reduction of tip radii.

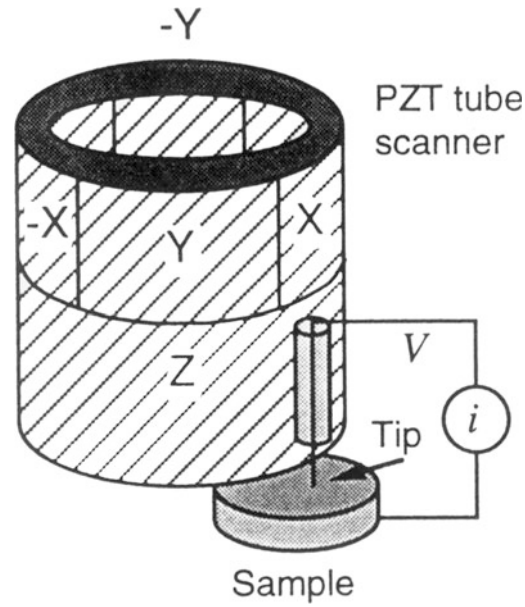

Fig. 2.3 Principle of operation of a commercial STM, a sharp tip attached to a piezoelectric tube scanner is scanned on a sample

2.2.2 Commercial STMs

There are a number of commercial STMs available on the market. In 1987, Digital Instruments, Inc. (now Bruker Instruments) located in Santa Barbara, CA, introduced the first commercial STM, the Nanoscope I. In a later-model Nanoscope IV STM for operation in ambient air, the sample is held in position while a piezoelectric crystal in the form of a cylindrical tube (referred to as PZT tube scanner) scans the sharp metallic probe over the surface in a raster pattern while sensing and outputting the tunneling current to the control station, Fig. 2.3. The digital signal processor (DSP) calculates the desired separation of the tip from the sample by sensing the tunneling current flowing between the sample and the tip. The bias voltage applied between the sample and the tip encourages the tunneling current to flow. The DSP completes the digital feedback loop by outputting the desired voltage to the piezoelectric tube. The STM operates in both the "constant height" and "constant current" modes depending on a parameter selection in the control panel. In the constant current mode, the feedback gains are set high, the tunneling tip closely tracks the sample surface, and the variation in the tip height required to maintain constant tunneling current is measured by the change in the voltage applied to the piezo tube. In the constant height mode, the feedback gains are set low, the tip remains at a nearly constant height as it sweeps over the sample surface, and the tunneling current is imaged.

Physically, the Nanoscope STM consists of three main parts: the head, which houses the piezoelectric tube scanner for three dimensional motion of the tip and the preamplifier circuit (FET input amplifier) mounted on top of the head for the tunneling current; the base on which the sample is mounted; and the base support, which supports the base and head (Bhushan 1999a). The base accommodates samples up to 10 mm by 20 and 10 mm in thickness. Scan sizes available for the STM are 0.7 μm (for atomic resolution), 12, 75 and 125 μm^2.

The scanning head controls the three dimensional motion of tip. The removable head consists of a piezo tube scanner, about 12.7 mm in diameter, mounted into an invar shell used to minimize vertical thermal drifts because of good thermal match between the piezo tube and the Invar. The piezo tube has separate electrodes for X, Y and Z which are driven by separate drive circuits. The electrode configuration (Fig. 2.3) provides x and y motions which are perpendicular to each other, minimizes horizontal and vertical coupling, and provides good sensitivity. The vertical motion of the tube is controlled by the Z electrode which is driven by the feedback loop. The x and y scanning motions are each controlled by two electrodes which are driven by voltages of same magnitudes, but opposite signs. These electrodes are called −Y, −X, +Y, and +X. Applying complimentary voltages allows a short, stiff tube to provide a good scan range without large voltages. The motion of the tip due to external vibrations is proportional to the square of the ratio of vibration frequency to the resonant frequency of the tube. Therefore, to minimize the tip vibrations, the resonant frequencies of the tube are high about 60 kHz in the vertical direction and about 40 kHz in the horizontal direction. The tip holder is a stainless steel tube with a 300 μm inner diameter for 250 μm diameter tips, mounted in ceramic in order to keep the mass on the end of the tube low. The tip is mounted either on the front edge of the tube (to keep mounting mass low and resonant frequency high) (Fig. 2.3) or the center of the tube for large range scanners, namely 75 and 125 μm (to preserve the symmetry of the scanning). This commercial STM accepts any tip with a 250 μm diameter shaft. The piezotube requires X-Y calibration which is carried out by imaging an appropriate calibration standard. Cleaved graphite is used for the small-scan length head while two dimensional grids (a gold plated ruling) can be used for longer range heads.

The Invar base holds the sample in position, supports the head, and provides coarse X-Y motion for the sample. A spring-steel sample clip with two thumb screws holds the sample in place. An x-y translation stage built into the base allows the sample to be repositioned under the tip. Three precision screws arranged in a triangular pattern support the head and provide coarse and fine adjustment of the tip height. The base support consists of the base support ring and the motor housing. The stepper motor enclosed in the motor housing allows the tip to be engaged and withdrawn from the surface automatically.

Samples to be imaged with STM must be conductive enough to allow a few nanoamperes of current to flow from the bias voltage source to the area to be scanned. In many cases, nonconductive samples can be coated with a thin layer of a conductive material to facilitate imaging. The bias voltage and the tunneling current depend on the sample. Usually they are set at a standard value for engagement and fine-tuned to enhance the quality of the image. The scan size depends on the sample and the features of interest. A maximum scan rate of 122 Hz can be used. The maximum scan rate is usually related to the scan size. Scan rate above 10 Hz is used for small scans (typically 60 Hz for atomic-scale imaging with a 0.7 μm scanner). The scan rate should be lowered for large scans, especially if the sample surfaces are rough or contain large steps. Moving the tip quickly along the sample surface at high scan rates with large scan sizes will usually lead to a tip crash. Essentially, the scan rate should be inversely proportional to the scan size (typically 2–4 Hz for 1 μm, 0.5–1 Hz for 12 μm, and 0.2 Hz for 125 μm scan sizes). Scan rate in length/time, is equal to scan length divided by the scan rate in Hz. For example, for 10 μm × 10 μm scan size scanned at 0.5 Hz, the scan rate is 10 μm/s. Typically, 256 × 256 data formats are most commonly used. The lateral resolution at larger scans is approximately equal to scan length divided by 256.

Figure 2.4 shows an example of STM images of an evaporated C_{60} film on gold-coated freshly-cleaved mica taken at room temperature and ambient pressure (Bhushan et al. 1993). Images with atomic resolution at two scan sizes are obtained. Next we describe STM designs which are available for special applications.

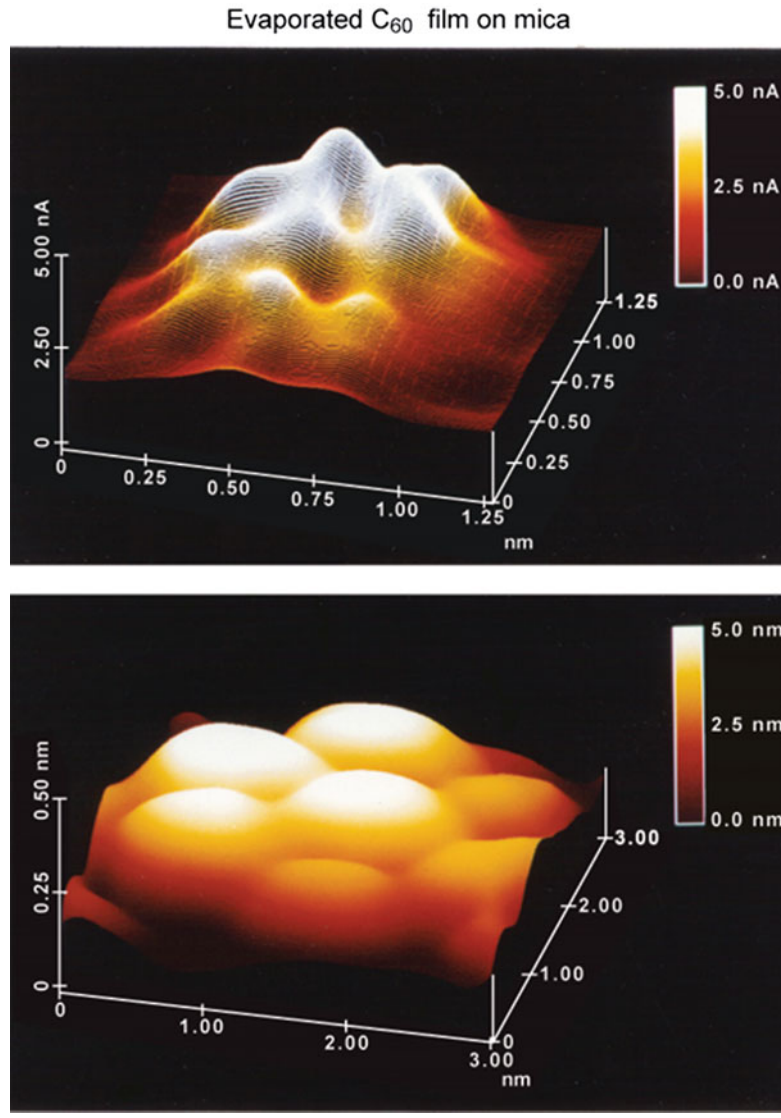

Fig. 2.4 STM images of evaporated C_{60} film on a gold-coated freshly-cleaved mica using a mechanically sheared Pt-Ir (80-20) tip in constant height mode (Bhushan et al. 1993)

2.2.2.1 Electrochemical STM

Electrochemical STM is used to perform and monitor the electrochemical reactions inside the STM. It includes a microscope base with an integral potentiostat, a short head with a 0.7 μm scan range and a differential preamp and the software required to operate the potentiostat and display the result of electrochemical reaction.

2.2.2.2 Standalone STM

Standalone STMs, which rest directly on the sample, are able to scan large samples. They are similar to the standard STM, except the sample base has been eliminated.

2.2.3 STM Probe Construction

The STM probe should have a cantilever integrated with a sharp metal tip with a low aspect ratio (tip length/tip shank) to minimize flexural vibrations. Ideally, the tip should be atomically sharp, but in practice, most tip preparation methods produce a tip with a rather ragged profile and that

consists of several asperities with the one closest to the surface responsible for tunneling. STM cantilevers with sharp tips are typically fabricated from metal wires of tungsten (W), platinum-iridium (Pt-Ir), or gold (Au) and sharpened by grinding, cutting with a wire cutter or razor blade, field emission/evaporator, ion milling, fracture, or electrochemical polishing/etching (Nicolaides et al. 1988; Ibe et al. 1990). The two most commonly used tips are made from either a Pt-Ir (80/20) alloy or tungsten wire. Iridium is used to provide stiffness. The Pt-Ir tips are generally mechanically formed and are readily available. The tungsten tips are etched from tungsten wire with an electrochemical process, for example by using 1 molar KOH solution with a platinum electrode in an electrochemical cell at about 30 V. In general, Pt-Ir tips provide better atomic resolution than tungsten tips, probably due to the lower reactivity of Pt. But tungsten tips are more uniformly shaped and may perform better on samples with steeply sloped features. The tungsten wire diameter used for the cantilever is typically 250 μm with the radius of curvature ranging from 20 to 100 nm and a cone angle ranging from 10° to 60°, Fig. 2.5. The wire can be bent in an L shape, if required for use in the instrument. For calculations of normal spring constant and natural frequency of round cantilevers, see Sarid and Elings (1991).

For imaging of deep trenches, high-aspect-ratio controlled geometry (CG) Pt-Ir probes are used,

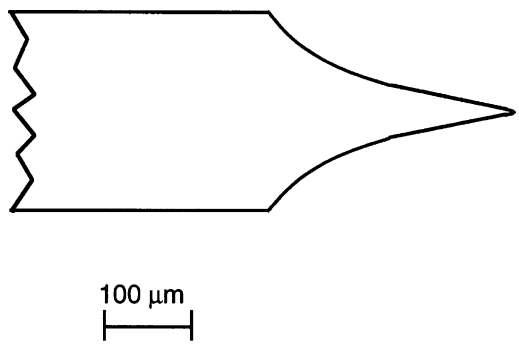

Fig. 2.5 Schematic of a typical tungsten cantilever with a sharp tip produced by electrochemical etching

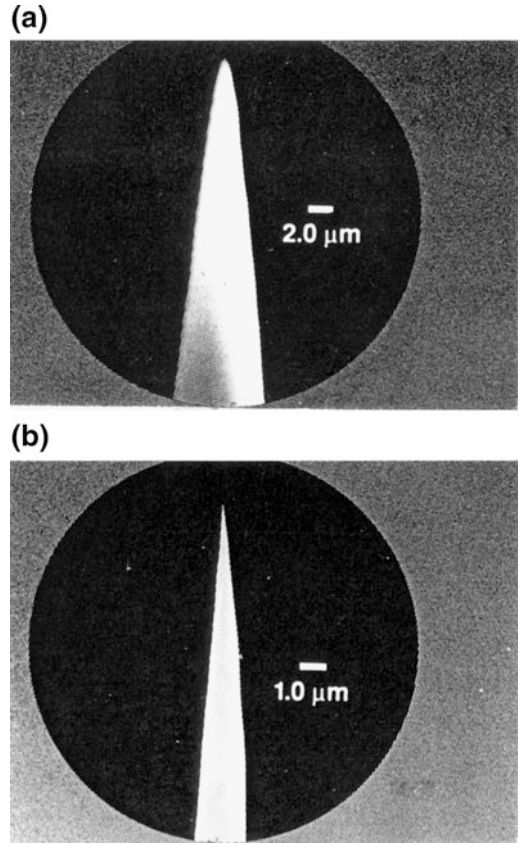

Fig. 2.6 Schematics of (**a**) CG Pt-Ir probe, and (**b**) CG Pt-Ir FIB milled probe

Fig. 2.6. These probes are electrochemically etched from Pt-Ir (80/20) wire and polished to a specific shape which is consistent from tip to tip. Probes have a full cone angle of approximately 15° and a tip radius of less than 50 nm. For imaging of very deep trenches (>0.25 μm) and nanofeatures, focused ion beam (FIB) milled CG probes with an extremely sharp tip (radius <5 nm) are used. For electrochemistry, Pt/Ir probes are coated with a nonconducting film (not shown in the figure).

Pt alloy and W tips are very sharp and have high resolution, but are fragile and sometimes break when contacting a surface. Diamond tips have been used by Kaneko and Oguchi (1990). The diamond tip made conductive by boron ion implantation is found to be chip resistant.

2.3 Atomic Force Microscope

Like the STM, AFM relies on a scanning technique to produce very high resolution, 3-D images of sample surfaces. AFM measures ultrasmall forces (less than 1 nN) present between the AFM tip surface and a sample surface. These small forces are measured by measuring the motion of a very flexible cantilever beam having an ultrasmall mass. While STM requires that the surface to be measured be electrically conductive, AFM is capable of investigating surfaces of both conductors and insulators on an atomic scale if suitable techniques for measurement of cantilever motion are used. In the operation of high resolution AFM, the sample is generally scanned, rather than the tip as in STM, because AFM measures the relative displacement between the cantilever surface and reference surface, and any cantilever movement would add vibrations. For measurements of large samples, AFMs are available where the tip is scanned and the sample is stationary. As long as the AFM is operated in the so-called contact mode, little if any vibration is introduced.

The AFM combines the principles of the STM and the stylus profiler, Fig. 2.7. In an AFM, the force between the sample and tip is detected rather than the tunneling current to sense the proximity of the tip to the sample. The AFM can be used either in static or dynamic mode. In the static mode, also referred to as repulsive mode or contact mode (Binnig et al. 1986), a sharp tip at the end of a cantilever is brought in contact with a sample surface. During initial contact, the atoms at the end of the tip experience a very weak repulsive force due to electronic orbital overlap with the atoms in the sample surface. The force acting on the tip causes a cantilever deflection which is measured by tunneling, capacitive, or optical detectors. The deflection can be measured to within 0.02 nm, so for typical cantilever spring constant of 10 N/m a force as low as 0.2 nN (corresponding normal pressure $\sim$200 MPa for a Si_3N_4 tip with radius of about 50 nm against single-crystal silicon) can be detected. (To put these number in perspective, individual atoms and human hair are typically fraction of a nanometer and about 75 μm in diameter, respectively, and an eyelash and a drop of water have a mass of about 100 nN and 10 μN, respectively.)

In the dynamic mode of operation for the AFM, also referred to as attractive force imaging or noncontact imaging mode (noncontact-AFM or nc-AFM operation), the tip is brought in close proximity (within a few nm) to, and not in contact with the sample (Giessibl et al. 2011; Schirmeisen et al. 2011). The cantilever is deliberately vibrated either in amplitude

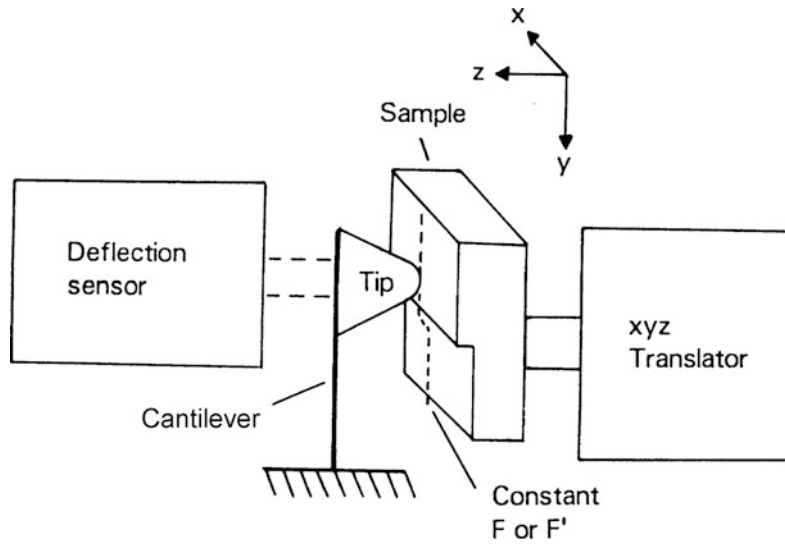

Fig. 2.7 Principle of operation of the AFM. Sample mounted on a piezoelectric scanner is scanned against a short tip and the cantilever deflection is measured, mostly, using a laser deflection technique. Force (contact mode) or force gradient (noncontact mode) is measured during scanning

modulation (AM) mode (Martin et al. 1987) or frequency modulation (FM) mode (Martin et al. 1987; Sarid and Elings 1991; Giessibl 1995; Anczykowski et al. 1996). Very weak van der Waals attractive forces are present at the tip-sample interface. In this technique, the normal pressure exerted at the interface is close to zero (desirable to avoid any surface deformation). In the two modes, surface topography is measured by laterally scanning the sample under the tip while simultaneously measuring the separation-dependent force or force gradient (derivative) between the tip and the surface, Fig. 2.7.

In the contact (static) mode, the interaction force between tip and sample is measured by measuring the cantilever deflection. In the noncontact (or dynamic) mode, the force gradient is obtained by vibrating the cantilever and measuring the shift of resonant frequency of the cantilever. To obtain topographic information, the interaction force is either recorded directly, or used as a control parameter for a feedback circuit that maintains the force or force derivative at a constant value. With an AFM operated in the contact mode, topographic images with a vertical resolution of less than 0.1 nm (as low as 0.01 nm) and a lateral resolution of about 0.2 nm have been obtained (Albrecht and Quate 1987; Binnig et al. 1987; Marti et al. 1987; Alexander et al. 1989; Meyer and Amer 1990a; Weisenhorn et al. 1991; Ruan and Bhushan 1994b). With a 0.01 nm displacement sensitivity, 10 nN–1 pN forces are measurable. These forces are comparable to the forces associated with chemical bonding, e.g., 0.1 μN for an ionic bond and 10 pN for a hydrogen bond (Binnig et al. 1986). For further reading, see Rugar and Hansma (1990), Sarid (1991), Sarid and Elings (1991), Binnig (1992), Durig et al. (1992); Frommer (1992), Meyer (1992), Marti and Amrein (1993), Guntherodt et al. (1995) and Wickramasinghe (2000).

Lateral forces being applied at the tip during scanning in the contact mode affect roughness measurements (den Boef 1991). To minimize effects of friction and other lateral forces in the topography measurements in contact-mode AFMs and to measure topography of soft surfaces, AFMs can be operated in the so-called or tapping mode or amplitude modulation mode (Maivald et al. 1991; Radmacher et al. 1992).

STM is ideal for atomic-scale imaging. To obtain atomic resolution with AFM, the spring constant of the cantilever should be weaker than the equivalent spring between atoms. For example, the vibration frequencies ω of atoms bound in a molecule or in a crystalline solid are typically 10^{13} Hz or higher. Combining this with the mass of the atoms m, on the order of 10^{-25} kg, gives interatomic spring constants k, given by $\omega^2 m$, on the order of 10 N/m (Rugar and Hansma 1990). (For comparison, the spring constant of a piece of household aluminum foil that is 4 mm long and 1 mm wide is about 1 N/m.) Therefore, a cantilever beam with a spring constant of about 1 N/m or lower is desirable. Tips have to be as sharp as possible. Tips with a radius ranging from 20 to 50 nm are commonly available.

Atomic resolution cannot be achieved with these tips at the normal load in the nN range. Atomic structures at these loads have been obtained from lattice imaging or by imaging of the crystal periodicity. Reported data show either perfectly ordered periodic atomic structures or defects on a larger lateral scale, but no well-defined, laterally-resolved, atomic-scale defects like those seen in images routinely obtained with STM. Interatomic forces with one or several atoms in contact are 20–40 or 50–100 pN, respectively. Thus, atomic resolution with AFM is only possible with a sharp tip on a flexible cantilever at a net repulsive force of 100 pN or lower (Ohnesorge and Binnig 1993). Upon increasing the force from 10 pN, Ohnesorge and Binnig (1993) observed that monoatomic steplines were slowly wiped away and a perfectly ordered structure was left. This observation explains why mostly defect-free atomic resolution has been observed with AFM. Note that for atomic-resolution measurements, the cantilever should not be too soft to avoid jumps. Further note that measurements in the noncontact imaging mode may be desirable for imaging with atomic resolution.

The key component in AFM is the sensor for measuring the force on the tip due to its

interaction with the sample. A cantilever (with a sharp tip) with extremely low spring constants is required for high vertical and lateral resolutions at small forces (0.1 nN or lower), but at the same time, a high resonant frequency (about 10–100 kHz) is necessary in order to minimize the sensitivity to vibration noise from the building near 100 Hz. This requires a spring with extremely low vertical spring constant (typically 0.05–1 N/m) as well as low mass (on the order of 1 ng). Today, the most advanced AFM cantilevers are microfabricated from silicon or silicon nitride using photolithographic techniques. (For further details on cantilevers, see a later section). Typical lateral dimensions are on the order of 100 μm, with the thicknesses on the order of 1 μm. The force on the tip due to its interaction with the sample is sensed by detecting the deflection of the compliant lever with a known spring constant. This cantilever deflection (displacement smaller than 0.1 nm) has been measured by detecting tunneling current similar to that used in STM in the pioneering work of Binnig et al. (1986) and later used by Giessibl et al. (1991), by capacitance detection (Neubauer et al. 1990; Goddenhenrich et al. 1990), piezoresistive detection (Stahl et al. 1994; Kassing and Oesterschulze 1997), and by four optical techniques namely (1) by optical interferometry (Mate et al. 1987; Erlandsson et al. 1988; Mate 1992; Jarvis et al. 1993) and with the use of optical fibers (Rugar et al. 1989; Albrecht et al. 1992), (2) by optical polarization detection (Schoenenberger and Alvarado 1989, 1990), (3) by laser diode feedback (Sarid et al. 1988), and (4) by optical (laser) beam deflection (Meyer and Amer 1988, 1990a, b; Alexander et al. 1989; Marti et al. 1990). Schematics of the four more commonly used detection systems are shown in Fig. 2.8. The tunneling method originally used by Binnig et al. (1986) in the first version of AFM uses a second tip to monitor the deflection of the cantilever with its force sensing tip. Tunneling is rather sensitive to contaminants, and the interaction between the tunneling tip and the rear side of the cantilever can become comparable to the interaction between the tip and sample. Tunneling is rarely used and is mentioned earlier for historical purposes. Giessibl et al. (1991) have used it for a low temperature AFM/STM design. In contrast to tunneling, other deflection sensors are far away from the cantilever at distances of microns to tens of mm. The optical techniques are believed to be more sensitive, reliable, and easily implemented detection methods than others (Sarid and Elings 1991; Meyer 1992). Optical beam deflection method has the largest working distance, is insensitive to distance changes, and is capable of measuring angular changes (friction forces). Therefore, it is

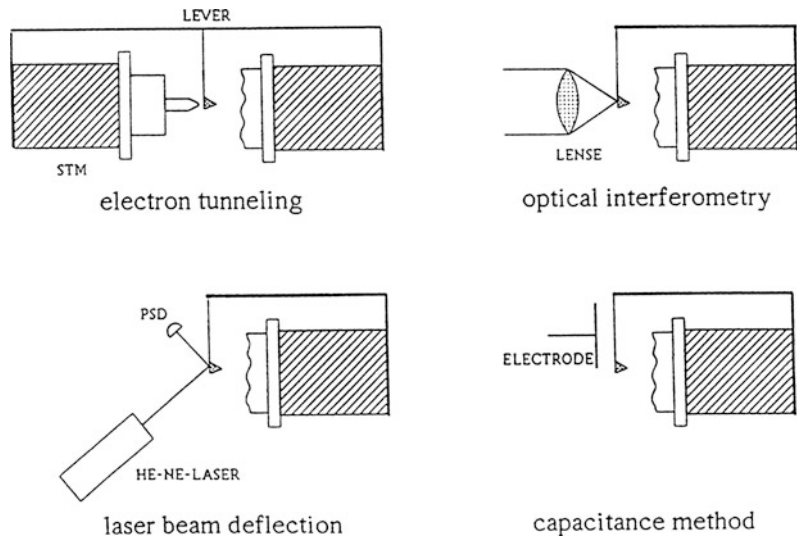

Fig. 2.8 Schematics of the four detection systems for measurement of cantilever deflection. In each set up, the sample mounted on piezoelectric body is shown on the *right*, the cantilever in the middle, and the corresponding deflection sensor on the *left* (Meyer 1992)

the most commonly used in the commercial SPMs.

Almost all SPMs use piezo translators to scan the sample or, alternatively, to scan the tip. An electric field applied across a piezoelectric material causes a change in the crystal structure, with expansion in some directions and contraction in others. A net change in volume also occurs (Ashcroft and Mermin 1976). The first STM used a piezo tripod for scanning (Binnig et al. 1982). The piezo tripod is one way to generate three-dimensional movement of a tip attached to its center. However, the tripod needs to be fairly large ($\sim$50 mm) to get a suitable range. Its size and asymmetric shape makes it susceptible to thermal drift. Tube scanners are widely used in AFMs (Binnig and Smith 1986). These provide ample scanning range within a small size. Control electronics systems for AFMs can use either analog or digital feedback. Digital feedback circuits are better suited for ultra-low noise operation.

Images from AFMs need to be processed. An ideal AFM is a noise free device that images a sample with perfect tips of known shape and has perfect linear scanning piezo. In reality, scanning devices are affected by distortions for which corrections must be made. The distortions can be linear and nonlinear. Linear distortions mainly result from imperfections in the machining of the piezo translators, causing cross talk between the Z-piezo to the X- and Y-piezos, and vice versa. Nonlinear distortions mainly result because of presence of hysteresis loop in piezoelectric ceramics. These may also result if the scan frequency approaches the upper frequency limit of the X- and Y-drive amplifiers or the upper frequency limit of the feedback loop (z-component). In addition, electronic noise may be present in the system. The noise is removed by digital filtering in the real space (Park and Quate 1987) or in the spatial frequency domain (Fourier space) (Cooley and Tukey 1965).

Processed data consists of many tens of thousands of points per plane (or data set). The output of the first STM and AFM images were recorded on an X-Y chart recorder, with z-value plotted against the tip position in the fast scan direction. Chart recorders have slow response so computers are used for display of the data. The data are displayed as wire mesh display or gray scale display (with at least 64 shades of gray).

2.3.1 Binnig et al.'s Design

In the first AFM design developed by Binnig et al. (1986), AFM images were obtained by measurement of the force on a sharp tip created by the proximity to the surface of the sample mounted on a 3-D piezoelectric scanner. Tunneling current between STM tip and the backside of the cantilever beam with attached tip was measured to obtain the normal force. This force was kept at a constant level with a feedback mechanism. The STM tip was also mounted on a piezoelectric element to maintain the tunneling current at a constant level.

2.3.2 Commercial AFM

A review of early designs of AFMs is presented by Bhushan (1999a). There are a large number of commercial AFMs available on the market. Major manufacturers of AFMs for use in ambient environment are: Bruker Instruments, Inc. (formerly Digital Instruments Inc. and later Veeco Instruments Inc.), Santa Barbara, California; Agilent Technologies, Santa Clara, California, Park Systems Corp., Suwon, Korea; Asylum Research, Santa Clara, California; NT-MDT Spectrum Instruments, Moscow Russia; Nanosurf AF, Liestal, Switzerland; Seiko Instruments, Japan; and Olympus, Japan. A major manufacturer for AFM/STMs for use in UHV and low temperature (LT) environment is Scienta Omicron GMBH, Taunusstein, Germany.

We describe here two typical commercial AFMs—small sample and large sample AFMs—for operation in the contact mode, produced by Bruker Instruments, Santa Barbara, CA, with scanning lengths ranging from about 0.7 μm (for atomic resolution) to about 125 μm (Alexander et al. 1989; Bhushan and Ruan 1994; Ruan and Bhushan 1994a, b). The original design of these

AFMs comes from Meyer and Amer (1988). Basically, the AFM scans the sample in a raster pattern while outputting the cantilever deflection error signal to the control station. The cantilever deflection (or the force) is measured using laser deflection technique, Fig. 2.9. The DSP in the workstation controls the z-position of the piezo based on the cantilever deflection error signal.

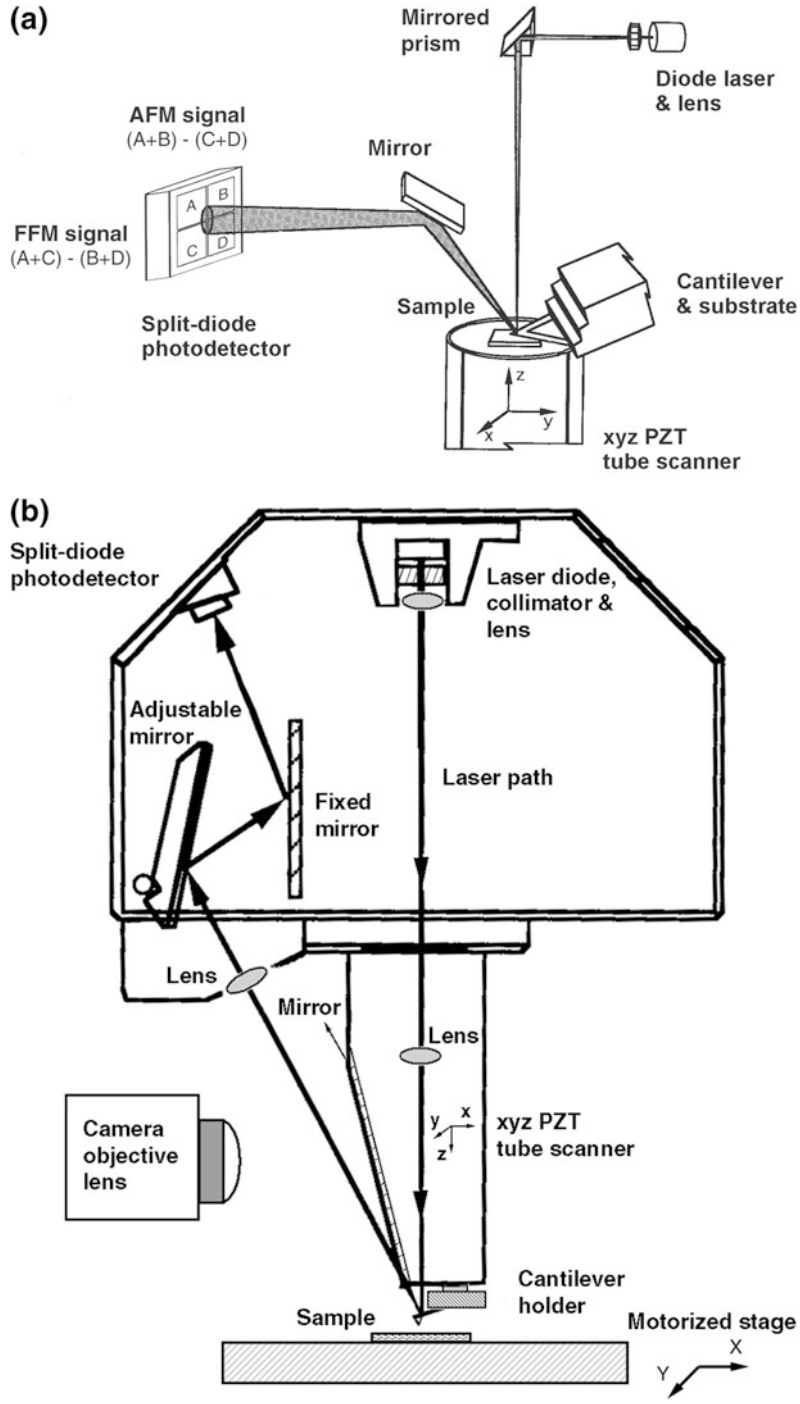

Fig. 2.9 Principles of operation of (**a**) a commercial small sample AFM/FFM, and (**b**) a large sample AFM/FFM

The AFM operates in both the "constant height" and "constant force" modes. The DSP always adjusts the height of the sample under the tip based on the cantilever deflection error signal, but if the feedback gains are low, the piezo remains at a nearly "constant height" and the cantilever deflection data is collected. With the high gains, the piezo height changes to keep the cantilever deflection nearly constant (therefore the force is constant) and the change in piezo height is collected by the system.

To describe further the operation principles of the small-sample commercial AFM shown in Fig. 2.9a, the sample, generally no larger than 10 mm × 10 mm, is mounted on a PZT tube scanner which consists of separate electrodes to scan precisely the sample in the x-y plane in a raster pattern, and to move the sample in the vertical (z) direction. A sharp tip at the free end of a flexible cantilever is brought in contact with the sample. Features on the sample surface cause the cantilever to deflect in the vertical and lateral directions as the sample moves under the tip. A laser beam from a diode laser (5 mW max peak output at 670 nm) is directed by a prism onto the back of a cantilever near its free end, tilted downward at about 10° with respect to the horizontal plane. The reflected beam from the vertex of the cantilever is directed through a mirror onto a quad photodetector (split photodetector with four quadrants) (commonly called position-sensitive detector or PSD, produced by Silicon Detector Corp., Camarillo, California). The differential signal from the top and bottom photodiodes provides the AFM signal, which is a sensitive measure of the cantilever vertical deflection. Topographic features of the sample cause the tip to deflect in the vertical direction as the sample is scanned under the tip. This tip deflection will change the direction of the reflected laser beam, changing the intensity difference between the top and bottom sets of photodetectors (AFM signal). In the AFM operating mode called the height mode, for topographic imaging or for any other operation in which the applied normal force is to be kept a constant, a feedback circuit is used to modulate the voltage applied to the PZT scanner to adjust the height of the PZT. This ensures that the cantilever vertical deflection (given by the intensity difference between the top and bottom detector), and consequently normal load, will remain constant during scanning. The PZT height variation is thus a direct measure of the surface roughness of the sample.

In a large sample AFM, both force sensors using optical deflection method and scanning unit are mounted on the microscope head, Fig. 2.9b. Because of vibrations added by cantilever movement, lateral resolution of this design is somewhat poorer than the design in Fig. 2.9a in which the sample is scanned instead of cantilever beam. The advantage of the large sample AFM is that large samples can be measured readily.

Most AFMs can be used for topography measurements in the so-called tapping mode (intermittent contact mode), also referred to as dynamic force microscopy in the amplitude mode (AM) mentioned earlier. In the tapping mode, during scanning over the surface, the cantilever/tip assembly is sinusoidally vibrated by a piezo mounted above it, and the oscillating tip slightly taps the surface at the resonant frequency of the cantilever (70–400 kHz) with a constant (20–100 nm) oscillating amplitude introduced in the vertical direction with a feedback loop keeping the average normal force constant, Fig. 2.10. The oscillating amplitude is kept large enough so that the tip does not get stuck to the sample because of adhesive attractions. The tapping mode is used in topography measurements to minimize effects of friction and other lateral forces to measure topography of soft surfaces.

Topographic measurements are made at any scanning angle. At a first instance, scanning angle may not appear to be an important parameter. However, the friction force between the tip and the sample will affect the topographic measurements in a parallel scan (scanning along the long axis of the cantilever). Therefore a perpendicular scan may be more desirable. Generally, one picks a scanning angle that gives the same topographic data in both directions. This angle may be slightly different than that for the perpendicular scan.

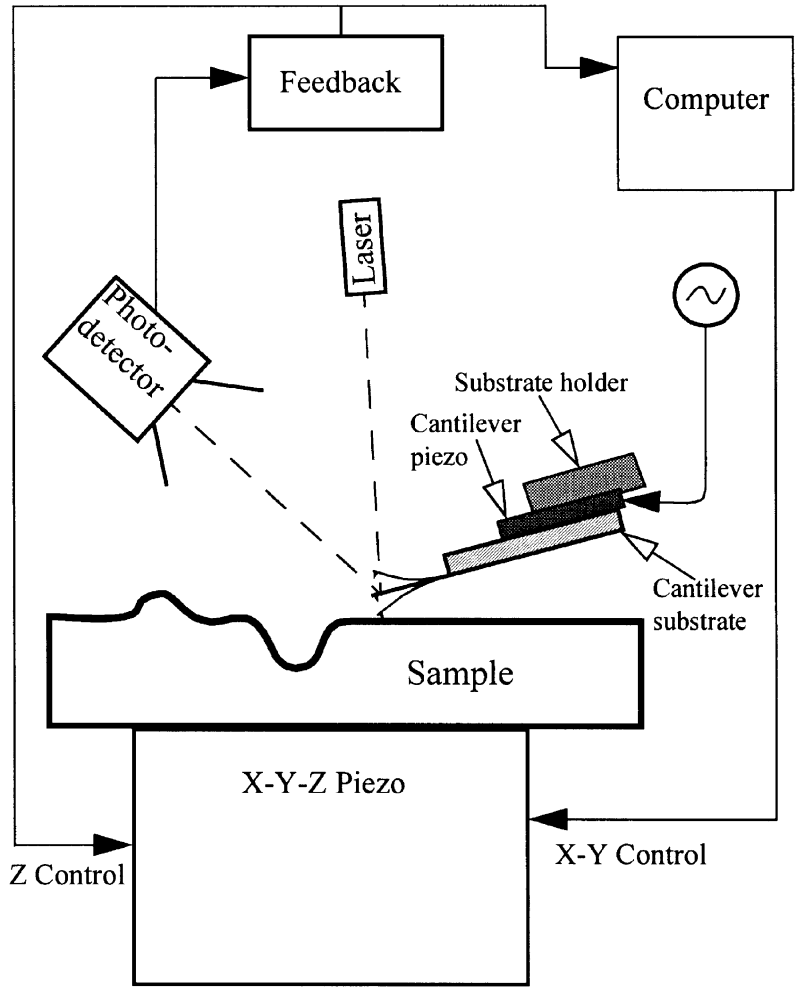

Fig. 2.10 Schematic of tapping mode used for surface roughness measurements

For measurement of friction force being applied at the tip surface during sliding, left hand and right hand sets of quadrants of the photodetector are used. In the so-called friction mode, the sample is scanned back and forth in a direction orthogonal to the long axis of the cantilever beam. A friction force between the sample and the tip will produce a twisting of the cantilever. As a result, the laser beam will be reflected out of the plane defined by the incident beam and the beam reflected vertically from an untwisted cantilever. This produces an intensity difference of the laser beam received in the left hand and right hand sets of quadrants of the photodetector. The intensity difference between the two sets of detectors (FFM signal) is directly related to the degree of twisting and hence to the magnitude of the friction force. This method provides three-dimensional maps of friction force. One problem associated with this method is that any misalignment between the laser beam and the photodetector axis introduces error in the measurement. However, by following the procedures developed by Ruan and Bhushan (1994a) in which the average FFM signal for the sample scanned in two opposite directions is subtracted from the friction profiles of each of the two scans, the misalignment effect is eliminated. By following the friction force calibration procedures developed by Ruan and Bhushan (1994a), voltages corresponding to friction forces can be converted to force units. The coefficient of

friction is obtained from the slope of friction force data measured as a function of normal loads typically ranging from 10 to 150 nN. This approach eliminates any contributions due to adhesive forces (Bhushan et al. 1994). For calculation of the coefficient of friction based on a single point measurement, friction force should be divided by the sum of applied normal load and intrinsic adhesive force. Furthermore, note that for a single asperity contact, the coefficient of friction is not independent of load. For further details, refer to a later section.

The tip is scanned in such a way that its trajectory on the sample forms a triangular pattern, Fig. 2.11. Scanning speeds in the fast and slow scan directions depend on the scan area and scan frequency. Scan sizes ranging from less than 1 nm × 1 nm to 125 μm × 125 μm and scan rates from less than 0.5–122 Hz typically can be used. Higher scan rates are used for smaller scan lengths. For example, scan rates in the fast and slow scan directions for an area of 10 μm × 10 m scanned at 0.5 Hz are 10 μm/s and 20 nm/s, respectively.

We now describe the construction of a small sample AFM in more detail. It consists of three main parts: the optical head that senses the cantilever deflection, a PZT tube scanner that controls the scanning motion of the sample mounted on its one end, and the base that supports the scanner and head and includes circuits for the deflection signal, Fig. 2.12a. The AFM connects directly to a control system. The optical head

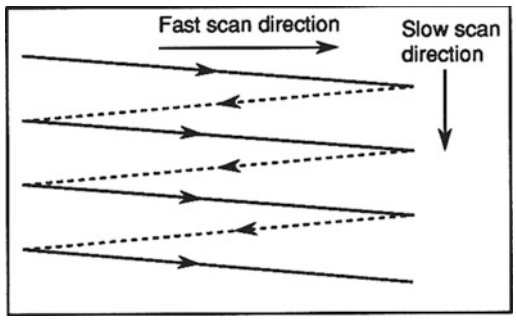

Fig. 2.11 Schematic of triangular pattern trajectory of the AFM tip as the sample is scanned in two dimensions. During imaging, data are recorded only during scans along the *solid scan lines*

consists of laser diode stage, photodiode stage preamp board, cantilever mount and its holding arm, and deflection beam reflecting mirror, Fig. 2.12b. The laser diode stage is a tilt stage used to adjust the position of the laser beam relative to the cantilever. It consists of the laser diode, collimator, focusing lens, baseplate, and the X and Y laser diode positioners. The positioners are used to place the laser spot on the end of the cantilever. The photodiode stage is an adjustable stage used to position the photodiode elements relative to the reflected laser beam. It consists of the split photodiode, the base plate, and the photodiode positioners. The deflection beam reflecting mirror is mounted on the upper left in the interior of the head which reflects the deflected beam toward the photodiode. The cantilever mount is a metal (for operation in air) or glass (for operation in water) block which holds the cantilever firmly at the proper angle, Fig. 2.12d. Next, the tube scanner consists of an Invar cylinder holding a single tube made of piezoelectric crystal which provides the necessary three-dimensional motion to the sample. Mounted on top of the tube is a magnetic cap on which the steel sample puck is placed. The tube is rigidly held at one end with the sample mounted on the other end of the tube. The scanner also contains three fine-pitched screws which form the mount for the optical head. The optical head rests on the tips of the screws which are used to adjust the position of the head relative to the sample. The scanner fits into the scanner support ring mounted on the base of the microscope, Fig. 2.12c. The stepper motor is controlled manually with the switch on the upper surface of the base and automatically by the computer during the tip engage and tip-withdraw processes.

The scan sizes available for these instruments are 0.7, 12, and 125 μm. The scan rate must be decreased as the scan size is increased. A maximum scan rate of 122 Hz can be used. Scan rates of about 60 Hz should be used for small scan lengths (0.7 μm). Scan rates of 0.5–2.5 Hz should be used for large scans on samples with tall features. High scan rates help reduce drift, but they can only be used on flat samples with

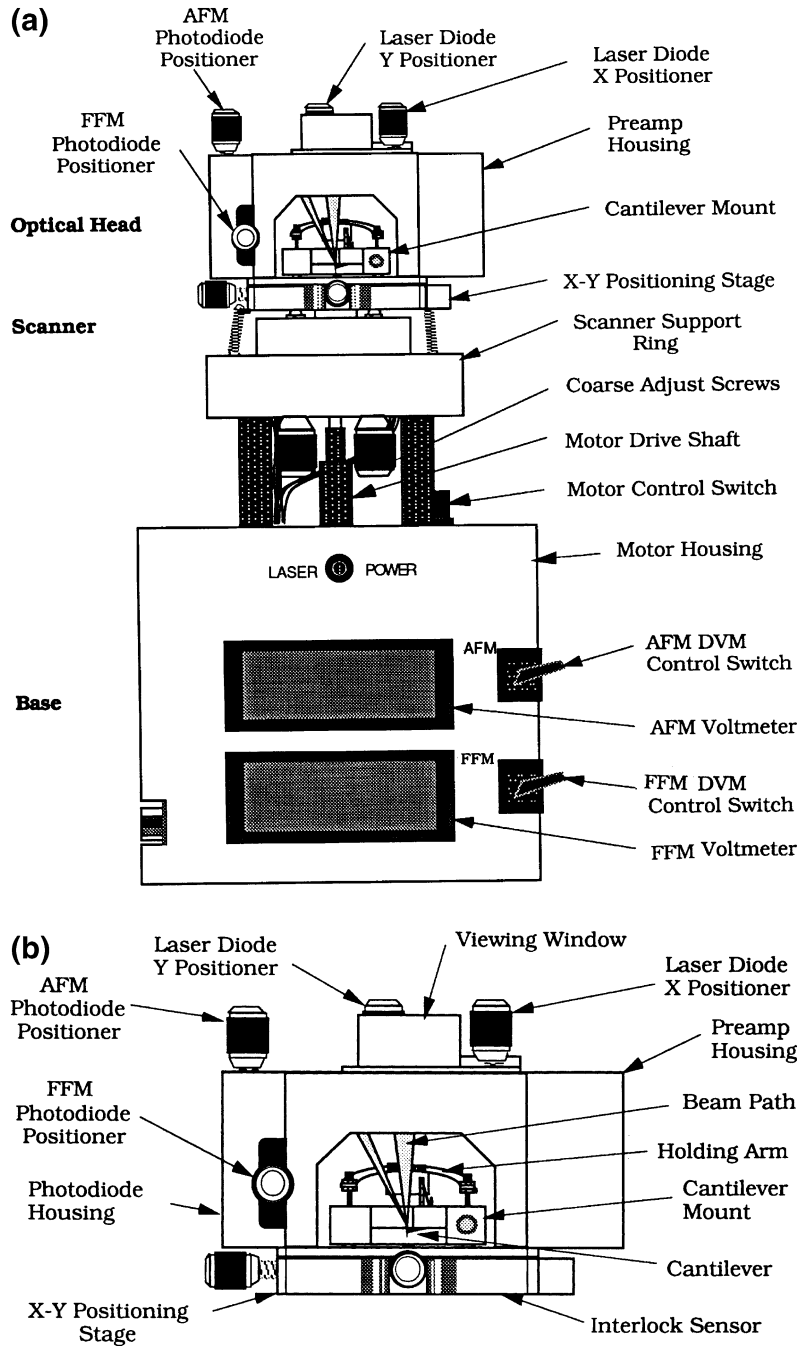

Fig. 2.12 Schematics of a commercial Multimode AFM/FFM made by Bruker Instruments Inc. (**a**) front view, (**b**) optical head, (**c**) base, and (**d**) cantilever substrate mounted on cantilever mount (not to scale)

small scan sizes. Scan rate, or scanning speed in length/time in the fast scan direction, is equal to twice the scan length times the scan rate in Hz, and in the slow direction, it is equal to scan length times the scan rate in Hz divided by number of data points in the transverse direction. For example, for 10 μm × 10 μm scan size scanned at 0.5 Hz, the scan rates in the fast and slow scan directions are 10 μm/s and 20 nm/s, respectively. Normally 256 × 256 data points

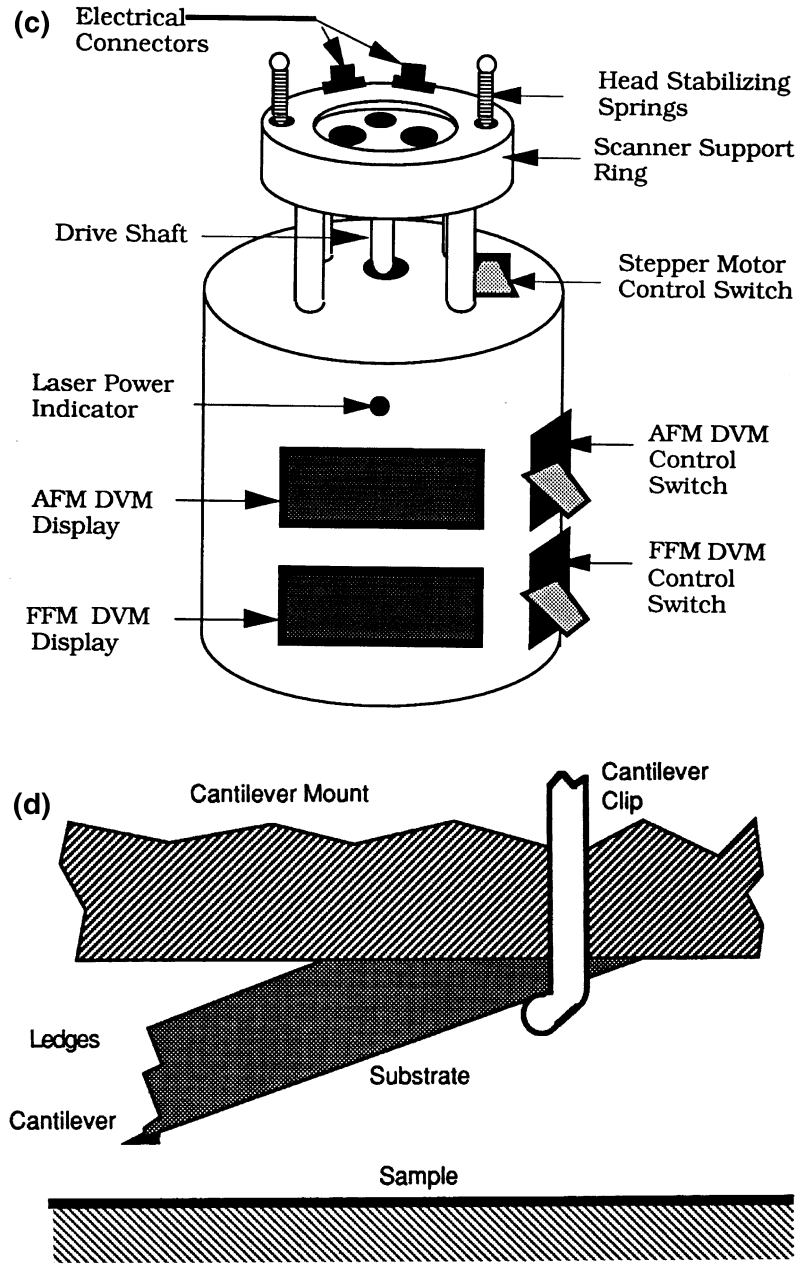

Fig. 2.12 (continued)

are taken for each image. The lateral resolution at larger scans is approximately equal to scan length divided by 256. The piezo tube requires x-y calibration, which is carried out by imaging an appropriate calibration standard. Cleaved graphite is used for small scan heads while two-dimensional grids (a gold plating ruling) can be used for longer range heads.

Examples of AFM images of freshly-cleaved highly-oriented pyrolytic (HOP) graphite and mica surfaces are shown in Fig. 2.13 (Albrecht and Quate 1987; Marti et al. 1987; Ruan and Bhushan 1994b). Images with near atomic resolution are obtained.

Force calibration mode is used to study interaction between the cantilever and the sample

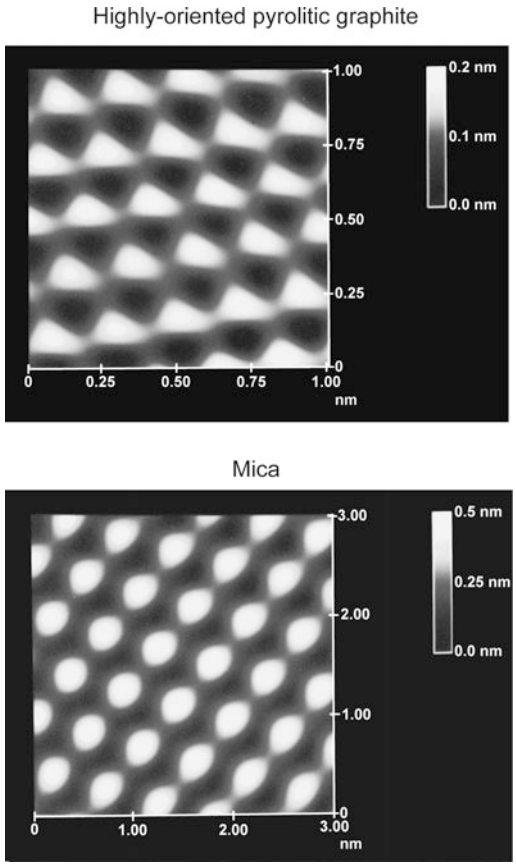

Fig. 2.13 Typical AFM images of freshly-cleaved highly-oriented pyrolytic graphite and mica surfaces taken using a square pyramidal Si_3N_4 tip

surface. In the force calibration mode, the X and Y voltages applied to the piezo tube are held at zero, and a sawtooth voltage is applied to the Z electrode of the piezo tube, Fig. 2.14a. The force measurement starts with the sample far away and the cantilever in its rest position. As a result of the applied voltage, the sample is moved up and down relative to the stationary cantilever tip. As the piezo moves the sample up and down, the cantilever deflection signal from the photodiode is monitored. The force-distance curve, a plot of the cantilever tip deflection signal as a function of the voltage applied to the piezo tube, is obtained. Figure 2.14b shows a typical force-distance curve showing the various features of the curve. The arrow heads reveal the direction of piezo travel. As the piezo extends, it approaches the tip, which is at this point in free air and hence shows no deflection. This is indicated by the flat portion of the curve. As the tip approaches the sample within a few nanometers (point A), an attractive force exists between the atoms of the tip surface and the atoms of the sample surface. The tip is pulled towards the sample and contact occurs at point B on the graph. From this point on, the tip is in contact with the surface and as the piezo further extends, the tip gets further deflected. This is represented by the sloped portion of the curve. As the piezo retracts, the tip goes beyond the zero deflection (flat) line into the adhesive regime because of attractive forces (van der Waals forces and long range meniscus forces). At point C in the graph, the tip snaps free of the adhesive forces, and is in free air again. The horizontal distance between points B and C along the retrace line gives the distance moved by the tip in the adhesive regime. This distance multiplied by the stiffness of the cantilever gives the adhesive force. Incidentally, the horizontal shift between the loading and unloading curves results from the hysteresis in the PZT tube (Bhushan 1999a).

2.3.2.1 Multimode Capabilities

The multimode AFM can be used for topography measurements in the contact mode and AM or tapping, mode as described earlier. It also can be used for measurements of lateral (friction) force, electric force gradients, and magnetic force gradients.

The multimode AFM using a grounded conducting tip can measure electric field gradients by oscillating the tip near its resonant frequency. When the lever encounters a force gradient from the electric field, the effective spring constant of the cantilever is altered, changing its resonant frequency. Depending on which side of the resonance curve is chosen, the oscillation amplitude of the cantilever increases or decreases due to the shift in the resonant frequency. By recording the amplitude of the cantilever, an image revealing the strength of the electric field gradient is obtained.

In a magnetic force microscope (MFM) used with a magnetically-coated tip, static cantilever

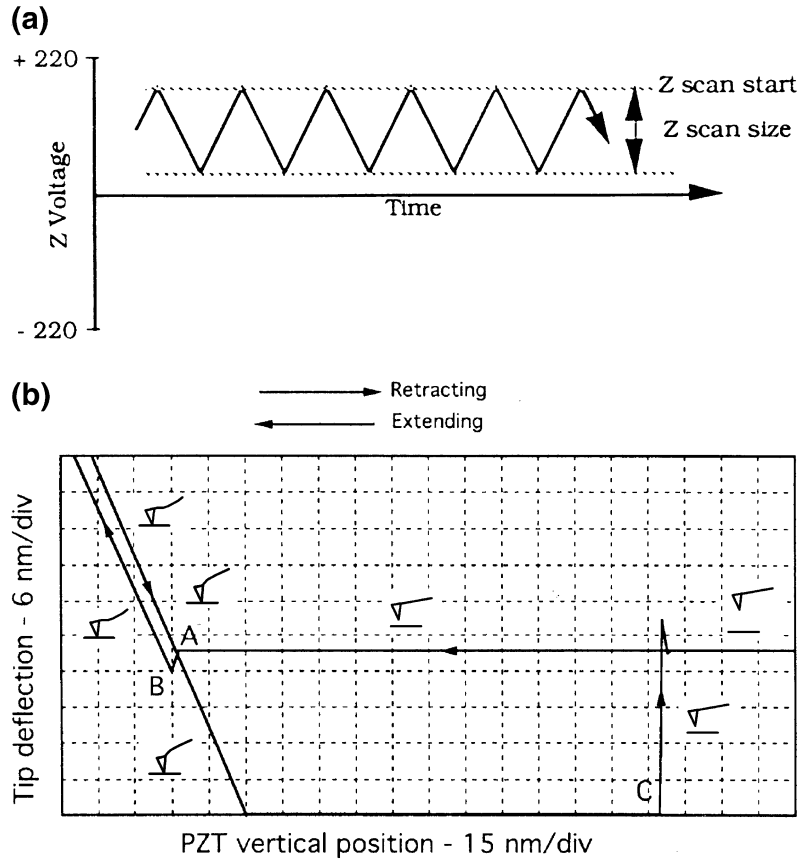

Fig. 2.14 (**a**) Force calibration Z waveform, and (**b**) a typical force-distance curve for a tip in contact with a sample. Contact occurs at point B; tip breaks free of adhesive forces at point C as the samples moves away from the tip

deflection is detected that occurs when a magnetic field exerts a force on the tip and the MFM images of magnetic materials can be produced. MFM sensitivity can be enhanced by oscillating the cantilever near its resonant frequency. When the tip encounters a magnetic force gradient, the effective spring constant, and hence the resonant frequency, is shifted. By driving the cantilever above or below the resonant frequency, the oscillation amplitude varies as the resonance shifts. An image of magnetic field gradients is obtained by recording the oscillation amplitude as the tip is scanned over the sample.

Topographic information is separated from the electric field gradients and magnetic field images by using a so-called lift mode. Measurements in lift mode are taken in two passes over each scan line. On the first pass, topographical information is recorded in the standard tapping mode where the oscillating cantilever lightly taps the surface. On the second pass, the tip is lifted to a user-selected separation (typically 20–200 nm) between the tip and local surface topography. By using the stored topographical data instead of the standard feedback, the separation remains constant without sensing the surface. At this height, cantilever amplitudes are sensitive to electric field force gradients or relatively weak but long-range magnetic forces without being influenced by topographic features. Two-pass measurements are taken for every scan line, producing separate topographic and magnetic force images.

2.3.2.2 Electrochemical AFM

This option allows study of electrochemical reactions in the AFM. It includes a potentiostat, a fluid cell with a transparent cantilever holder and electrodes, and the software required to operate the potentiostat and display the results of the electrochemical reaction.

2.3.3 AFM Probe Construction

Various probes (cantilevers and tips) are used for AFM studies. The cantilever stylus used in the AFM should meet the following criteria: (1) low normal spring constant (stiffness), (2) a high resonant frequency, (3) a high quality factor of the cantilever Q, (4) high lateral spring constant (stiffness), (5) short cantilever length, (6) incorporation of components (such as mirror) for deflection sensing, and (7) a sharp protruding tip (Albrecht et al. 1990). In order to register a measurable deflection with small forces, the cantilever must flex with a relative low force (on the order of few nN) requiring vertical spring constants of 10^{-2} to 10^{2} N/m for atomic resolution in the contact profiling mode. The data rate or imaging rate in the AFM is limited by the mechanical resonant frequency of the cantilever. To achieve a large imaging bandwidth, the AFM cantilever should have resonant frequency greater than about 10 kHz (preferably 30–100 kHz) in order to make the cantilever the least sensitive part of the system. Fast imaging rates are not just a matter of convenience, since the effects of thermal drifts are more pronounced with slow-scanning speeds. The combined requirements of a low spring constant and a high resonant frequency is met by reducing the mass of the cantilever. The quality factor Q ($=\omega_R/(c/m)$ where ω_R is the resonant frequency of the damped oscillator, c is the damping constant, and m is the mass of the oscillator) should have a high value for some applications. For example, resonance curve detection is a sensitive modulation technique for measuring small force gradients in noncontact imaging. Increasing the Q increases the sensitivity of the measurements. Mechanical Q values of 100–1000 are typical. In contact modes, Q is less important. A high lateral spring constant in the cantilever is desirable to reduce the effect of lateral forces in the AFM as frictional forces can cause appreciable lateral bending of the cantilever. Lateral bending results in error in the topography measurements. For friction measurements, cantilevers with less lateral rigidity are preferred. A sharp protruding tip must be formed at the end of the cantilever to provide a well-defined interaction with the sample over a small area. The tip radius should be much smaller than the radii of corrugations in the sample in order for these to be measured accurately. The lateral spring constant depends critically on the tip length. Additionally, the tip should be centered at the free end.

In the past, cantilevers have been cut by hand from thin metal foils or formed from fine wires. Tips for these cantilevers were prepared by attaching diamond fragments to the ends of the cantilevers by hand, or, in the case of wire cantilevers, electrochemically etching the wire to a sharp point. Several cantilever geometries for wire cantilevers have been used. The simplest geometry is the L-shaped cantilever, usually made by bending a wire at a 90° angle. Other geometries include single-V and double-V geometries with a sharp tip attached at the apex of V, and double-X configuration with a sharp tip attached at the intersection (Marti et al. 1988; Burnham and Colton 1989). These cantilevers can be constructed with high vertical spring constants. For example, a double-cross cantilever with an effective spring constant of 250 N/m was used by Burnham and Colton (1989). The small size and low mass needed in the AFM make hand fabrication of the cantilever a difficult process with poor reproducibility. Conventional microfabrication techniques are ideal for constructing planar thin-film structures which have submicron lateral dimensions. Triangular (V-shaped) cantilevers have improved (higher) lateral spring constants in comparison to rectangular cantilevers. In terms of spring constants, triangular cantilevers are approximately equivalent to two rectangular cantilevers in parallel (Albrecht et al. 1990). Although the macroscopic radius of a photolithographically patterned corner is seldom much less than about 50 nm, microscopic asperities on the etched surface provide tips with near atomic dimensions.

Cantilevers and tips have been used from a whole range of materials. Most common are cantilevers/tips made of Si_3N_4, Si, and stainless steel/diamond. Besides the geometry, the material parameters that determine the resonant frequency of the cantilever are Young's modulus

Table 2.2 Relevant properties of commonly used materials for cantilevers and diamond used in the some tips

Property	Diamond (for tips)	Si_3N_4	Si	Stainless steel	W	Ir
Young's Modulus (E) (GPa)	900–1050	310	130–188	210	350	530
Density (ρg) (kg/m^3)	3515	3180	2330	8050	19,310	–
Microhardness (GPa)	78.4–102	19.6	9–10	2–4	3.2	~3
Speed of sound ($\sqrt{E/\rho}$) (m/s)	17,000	9900	8200	5080	4250	5300

and density. Table 2.2 shows the relevant properties of commonly used materials and the speed of sound, indicative of the resonant frequency for a cantilever beam. Hardness is important to judge the durability of the tips, and is also listed in the table. Materials used for STM cantilevers are also included.

Silicon nitride cantilevers with integrated tips are less expensive than those made of other materials. They are very rugged and well suited to imaging in almost all environments. They are especially compatible to organic and biological materials. Microfabricated silicon nitride triangular beams with integrated square pyramidal tips made of plasma-enhanced chemical vapor deposition (PECVD) are the most commonly used (Albrecht et al. 1990). Figure 2.15a shows a schematic example of four cantilever beams, each with different sizes and spring constants, arranged in pairs, attached to a borosilicate glass substrate (Pyrex) and marketed by various manufacturers including Bruker Instruments, Inc. Each pair of triangular cantilevers measures 115 and 193 μm from the substrate to the apex, with base widths of 122 and 205 μm respectively. These cantilevers are commercially available with wide (top) and narrow (bottom) legs, all in the same thickness of 0.6 μm. Calculated spring constant and measured natural frequencies for each of the configurations are listed in Table 2.3. The most commonly used cantilever beam is the 115 μm-long, wide-legged cantilever (vertical spring constant = 0.58 N/m). Cantilevers with smaller spring constants should be used on softer samples. Pyramidal tips are highly symmetric with ends having a radius of about 20–50 nm. The tip side walls have a slope of 35°, and the length of the edges of the tip at the cantilever base is about 4 μm.

An alternative to silicon nitride cantilevers with integrated tips are microfabricated single-crystal silicon cantilevers with integrated tips. Si tips are sharper than Si_3N_4 tips because they are directly formed by the anisotropic etch in single-crystal Si rather than using an etch pit as a mask for deposited materials (Wolter et al. 1991). Etched single-crystal n-type silicon rectangular cantilevers with square pyramidal tips with a lower radius of less than 10 nm for contact and tapping mode (tapping mode etched silicon probe or TESP) AFMs are commercially available from various manufacturers including Bruker Instruments, Inc., Fig. 2.15b. Spring constants and resonant frequencies are also presented in the Fig. 2.15b.

Commercial triangular Si_3N_4 cantilevers have a typical width-thickness ratio of 10–30, which results in 100–1000 times stiffer spring constants in the lateral direction compared to the normal direction. Therefore these cantilevers are not well suited for torsion. For friction measurements, the torsional spring constant should be minimized in order to be sensitive to lateral forces. Rather long cantilevers with small thicknesses and large tip lengths are most suitable. Rectangular beams have lower torsional spring constants in comparison to the triangular (V-shaped) cantilevers. Table 2.4 lists the spring constants (with full length of the beam used) in three directions of typical rectangular beams. We note that lateral and torsional spring constants are about two orders of magnitude larger than the normal spring constants. A cantilever beam required for the tapping mode is quite stiff and may not be sensitive enough for friction measurements. Meyer et al. (1992) used a specially designed rectangular silicon cantilever with length = 200 m, width = 21 μm, thickness = 0.4 μm, tip

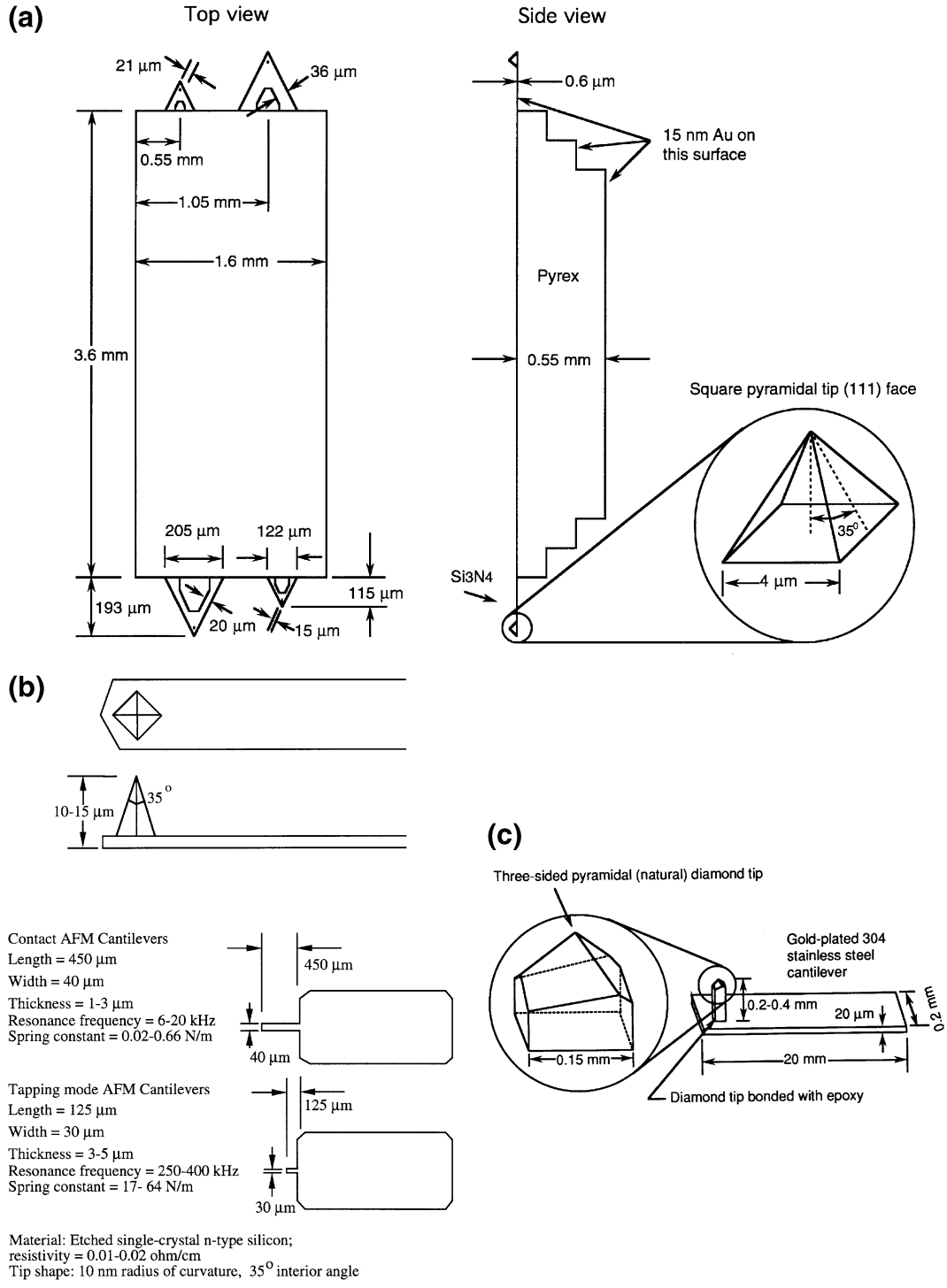

Fig. 2.15 Schematics of (**a**) triangular cantilever beam with square pyramidal tips made of PECVD Si_3N_4, (**b**) rectangular cantilever beams with square pyramidal tips made of etched single-crystal silicon, and (**c**) rectangular cantilever stainless steel beam with three-sided pyramidal natural diamond tip

Table 2.3 Measured vertical spring constants and natural frequencies of triangular (V-shaped) cantilevers made of PECVD Si_3N_4 (Data provided by Bruker Instruments, Inc.)

Cantilever dimension	Spring constant (k_z) (N/m)	Natural frequency (ω_0) (kHz)
115 μm long, narrow leg	0.38	40
115 μm long, wide leg	0.58	40
193 μm long, narrow leg	0.06	13–22
193 μm long, wide leg	0.12	13–22

Table 2.4 Vertical (k_z), lateral (k_y), and torsional (k_{yT}) spring constants of rectangular cantilevers made of Si (IBM) and PECVD Si_3N_4 (Bruker Instruments, Inc.)

Dimensions/stiffness	Si cantilever	Si_3N_4 cantilever
Length (L) (μm)	100	100
Width (b) (μm)	10	20
Thickness (h) (μm)	1	0.6
Tip length (ℓ) (μm)	5	3
k_z (N/m)	0.4	0.15
k_y (N/m)	40	175
k_{yT} (N/m)	120	116
ω_0 (kHz)	~90	~65

Note $k_z = Ebh^3/4L^3$, $k_y = Eb^3h/4\ell^3$, $k_{yT} = Gbh^3/3L\ell^2$, and $\omega_o = [k_z/(m_c + 0.24\ bhL\rho)]^{1/2}$ where E is Young's modulus, G is the modulus of rigidity [=E/2(1 + ν), where ν is the Poisson's ratio], ρ is the mass density of the cantilever, and m_c is the concentrated mass of the tip (~4 ng) (Sarid and Elings 1991). For Si, E = 130 GPa, $\rho g = 2300\ kg/m^3$, and ν = 0.3. For Si_3N_4, E = 150 GPa, $\rho g = 3100\ kg/m^3$, and ν = 0.3

length = 12.5 μm, and shear modulus = 50 GPa, giving a normal spring constant of 0.007 N/m and torsional spring constant of 0.72 N/m which gives a lateral force sensitivity of 10 pN and an angle of resolution of 10^{-7} rad. With this particular geometry, sensitivity to lateral forces could be improved by about a factor of 100 compared with commercial V-shaped Si_3N_4 or rectangular Si or Si_3N_4 cantilevers used by Meyer and Amer (1990b) with torsional spring constant of ~100 N/m. Ruan and Bhushan (1994a) and Bhushan and Ruan (1994) used 115 μm-long, wide-legged V-shaped cantilevers made of Si_3N_4 for friction measurements.

For scratching, wear, and indentation studies, single-crystal natural diamond tips ground to the shape of a three-sided pyramid with an apex angle of either 60° or 80° whose point is sharpened to a radius of about 100 nm are commonly used (Bhushan et al. 1994; Bhushan 1999a) (Fig. 2.15c). The tips are bonded with conductive epoxy to a gold-plated 304 stainless steel spring sheet (length = 20 mm, width = 0.2 mm, thickness = 20–60 μm) which acts as a cantilever. Free length of the spring is varied to change the beam stiffness. The normal spring constant of the beam ranges from about 5 to 600 N/m for a 20 μm thick beam. The tips are produced by various manufacturers including R-DEC Co., Tsukuba, Japan. SEM micrographs of silicon nitride, single-crystal silicon, and natural diamond tips are shown in Fig. 2.16.

For imaging within trenches by AFM, high aspect ratio tips are used. Examples of the two probes are shown in Fig. 2.17. The high-aspect ratio tip (Hart) probes are produced by starting with a conventional Si_3N_4 pyramidal probe. Through a combination of focused ion beam (FIB) and high-resolution scanning electron microscopy (SEM) techniques, a thin filament is

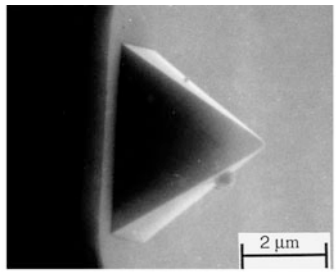

Square pyramidal silicon nitride tip

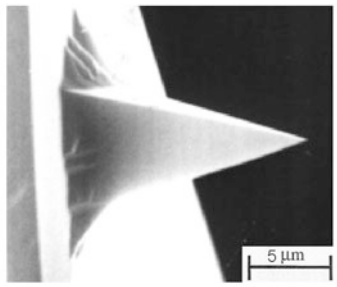

Square pyramidal single-crystal silicon tip

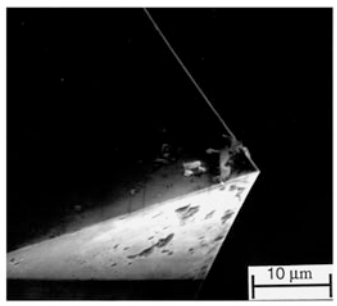

Three-sided pyramidal natural diamond tip

Fig. 2.16 SEM micrographs of a square-pyramidal PECVD Si_3N_4 tip, a square pyramidal etched single-crystal silicon tip, and a three-sided pyramidal natural diamond tip

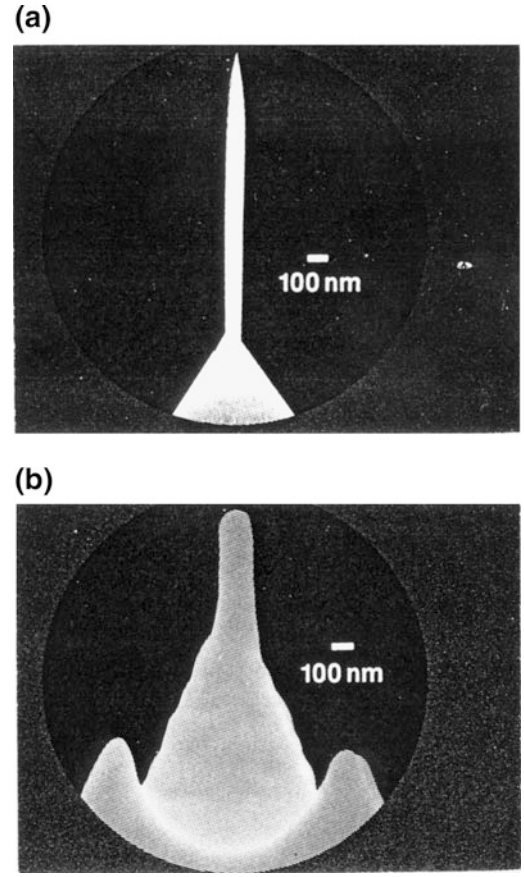

Fig. 2.17 Schematics of (**a**) HART Si_3N_4 probe, and (**b**) FIB milled Si_3N_4 probe

grown at the apex of the pyramid. The probe filament is approximately 1 μm long and 0.1 μm in diameter. It tapers to an extremely sharp point (radius better than the resolution of most SEMs). The long thin shape and sharp radius make it ideal for imaging within "vias" of microstructures and trenches (>0.25 μm). Because of flexing of the probe, it is unsuitable for imaging structures at the atomic level since the flexing of the probe can create image artifacts. For atomic-scale imaging, a FIB-milled probe is used which is relatively stiff yet allows for closely spaced topography. These probes start out as conventional Si_3N_4 pyramidal probes but the pyramid is FIB milled until a small cone shape is formed which has a high aspect ratio with 0.2–0.3 μm in length. The milled probes allow nanostructure resolution without sacrificing rigidity.

Carbon nanotube tips having small diameter and high aspect ratio are used for high resolution imaging of surfaces and of deep trenches, in the tapping mode or noncontact mode. Single-walled carbon nanotubes (SWNT) are microscopic graphitic cylinders that are 0.7–3 nm in diameter and up to many microns in length. Larger structures called multi-walled carbon nanotubes (MWNT) consist of nested, concentrically

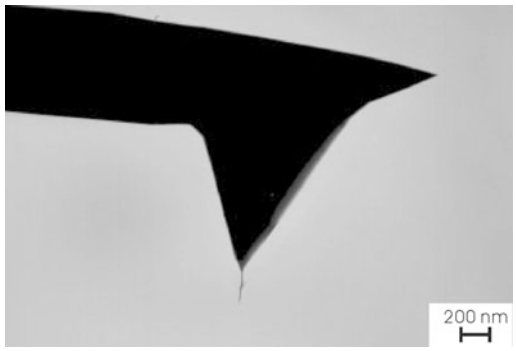

Fig. 2.18 SEM micrograph of a multi-walled carbon nanotube (MWNT) tip physically attached on the single-crystal silicon, square-pyramidal tip (Courtesy Piezomax Technologies, Inc.)

arranged SWNT and have diameters ranging from 3 to 50 nm. MWNT carbon nanotube AFM tips are produced by manual assembly (Dai et al. 1996), chemical vapor deposition (CVD) synthesis, and hybrid fabrication process (Hafner et al. 2001). Figure 2.18 shows a TEM micrograph of a carbon nanotube tip, ProbeMax™, commercially produced by mechanical assembly by Piezomax Technologies, Inc., Middleton, Wisconsin. For production of these tips, MWNT nanotubes are produced by carbon arc. They are physically attached on single-crystal silicon square-pyramidal tips in the SEM using a manipulator and the SEM stage to control the nanotubes and the tip independently. Once the nanotube is attached to the tip, it is usually too long to image with. It is shortened using an AFM applying voltage between the tip and the sample. Nanotube tips are also commercially produced by CVD synthesis by NanoDevices, Santa Barbara, California.

2.3.4 Friction Measurement Methods

Based on the work by Ruan and Bhushan (1994a), the two methods for friction measurements are now described in more detail. (Also see, Meyer and Amer 1990b; Palacio and Bhushan 2010.) A scanning angle is defined as the angle relative to the y-axis in Fig. 2.19a. This is also the long axis of the cantilever. A zero degree scanning angle corresponds to the sample scanning in the y direction, and a 90° scanning angle corresponds to the sample scanning perpendicular to this axis in the xy plane (along the x axis). If the scanning direction is in both y and -y directions, we call this "parallel scan". Similarly, a "perpendicular scan" means the scanning direction is in x and −x directions. The sample traveling direction for each of these two methods is illustrated in Fig. 2.19b.

In the method 1 (using "height" mode with parallel scans) in addition to topographic imaging, it is also possible to measure friction force when the scanning direction of the sample is parallel to y direction (parallel scan). If there were no friction force between the tip and the moving sample, the topographic feature would be the only factor which cause the cantilever to be deflected vertically. However, friction force does exist on all contact surfaces where one object is moving relative to another. The friction force between the sample and the tip will also cause a cantilever deflection. We assume that the normal force between the sample and the tip is W_0 when the sample is stationary (W_0 is typically in the range of 10 nN–200 nN), and the friction force between the sample and the tip is W_f as the sample scans against the tip. The direction of friction force (W_f) is reversed as the scanning direction of the sample is reversed from the positive (y) to the negative (−y) direction $\overrightarrow{W}_{f(y)} = -\overrightarrow{W}_{f(-y)}$.

When the vertical cantilever deflection is set at a constant level, it is the total force (normal force and friction force) applied to the cantilever that keeps the cantilever deflection at this level. Since the friction force is in opposite directions as the traveling direction of the sample is reversed, the normal force will have to be adjusted accordingly when the sample reverses its traveling direction, so that the total deflection of the cantilever will remain the same. We can calculate the difference of the normal force between the two traveling directions for a given friction force W_f. First, by means of a constant deflection, the total moment applied to the cantilever is constant. If we take the reference point

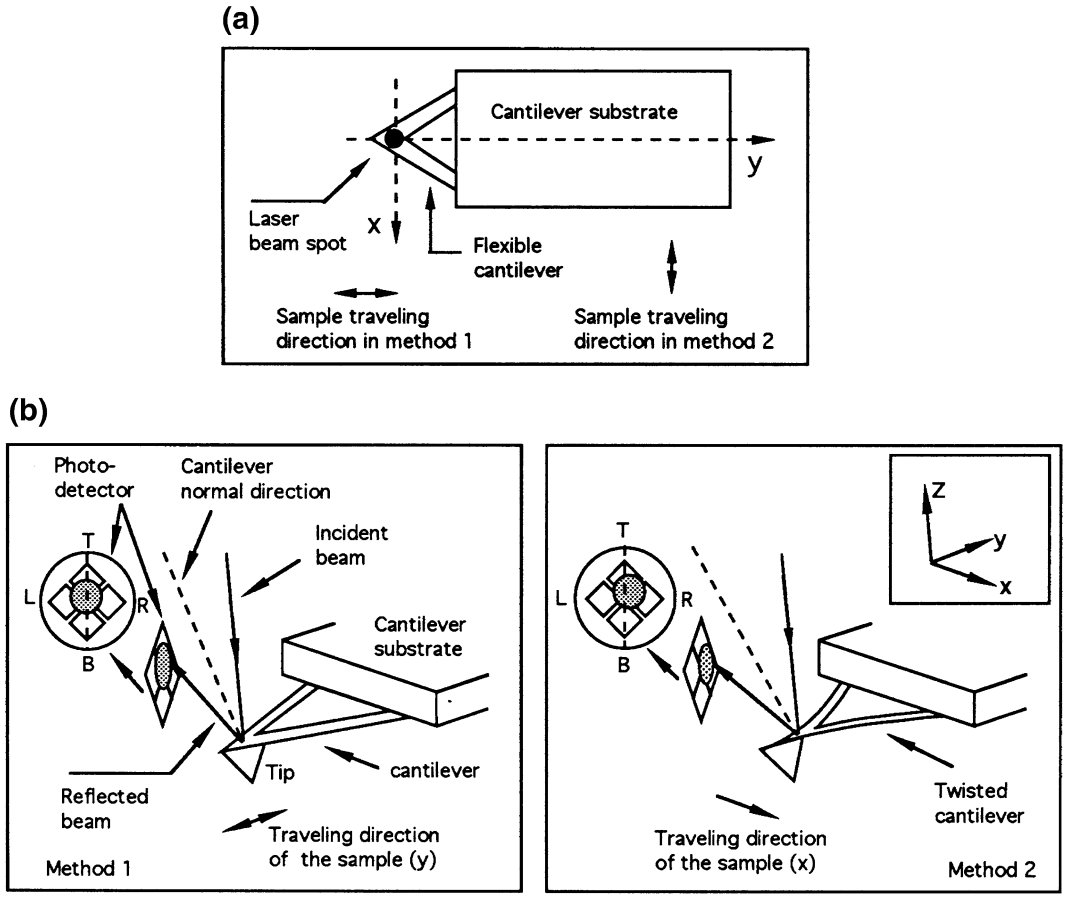

Fig. 2.19 (**a**) Schematic defining the x- and y-directions relative to the cantilever, and showing the sample traveling direction in two different measurement methods discussed in the text, (**b**) schematic of deformation of the tip and cantilever shown as a result of sliding in the x- and y-directions. A twist is introduced to the cantilever if the scanning is in the x-direction (**b**, *right*) (Ruan and Bhushan 1994a)

to be the point where the cantilever joins the cantilever holder (substrate), point P in Fig. 2.20, we have the following relationship:

$$(W_0 - \Delta W_1)L + W_f\ell = (W_0 + \Delta W_2)L - W_f\ell \tag{2.1}$$

or

$$(\Delta W_1 + \Delta W_2)L = 2W_f\ell \tag{2.2}$$

Thus

$$W_f = (\Delta W_1 + \Delta W_2)/2\ell \tag{2.3}$$

where ΔW_1 and ΔW_2 are the absolute value of the changes of normal force when the sample is traveling in −y and y directions, respectively, as shown in Fig. 2.20; L is the length of the cantilever; and ℓ is the vertical distance between the end of the tip and point P. The coefficient of friction (μ) between the tip and the sample is then given as

$$\mu = \frac{W_f}{W_0} = \left[\frac{(\Delta W_1 + \Delta W_2)}{W_0}\right]\left(\frac{L}{2\ell}\right) \tag{2.4}$$

In all circumstances, there are adhesive and interatomic attractive forces between the

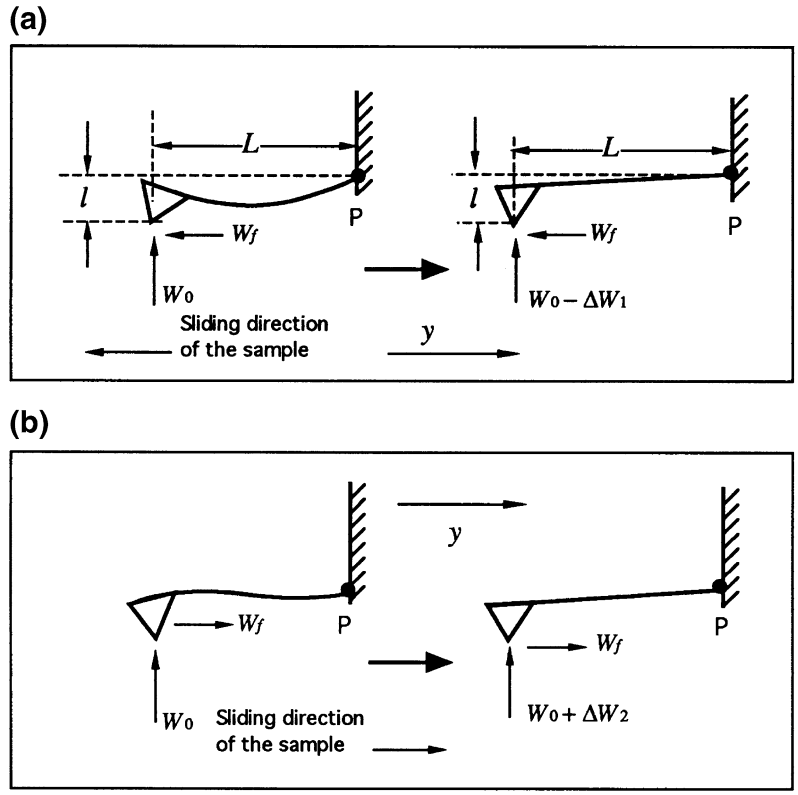

Fig. 2.20 **a** Schematic showing an additional bending of the cantilever—due to friction force when the sample is scanned in the y- or −y-direction (*left*). **b** This effect will be canceled by adjusting the piezo height by a feedback circuit (*right*) (Ruan and Bhushan 1994a)

cantilever tip and the sample. The adhesive force can be due to water from the capillary condensation and other contaminants present at the surface which form meniscus bridges (Blackman et al. 1990; O'Shea et al. 1992; Bhushan 1999a) and the interatomic attractive force includes van der Waals attraction (Burnham et al. 1991). If these forces (and indentation effect as well, which is usually small for rigid samples) can be neglected, the normal force W_0 is then equal to the initial cantilever deflection H_0 multiplied by the spring constant of the cantilever. ($\Delta W_1 + W_2$) can be measured by multiplying the same spring constant by the height difference of the piezo tube between the two traveling directions (y and −y directions) of the sample. This height difference is denoted as ($\Delta H_1 + \Delta H_2$), shown schematically in Fig. 2.21. Thus, Eq. (2.4) can be rewritten as

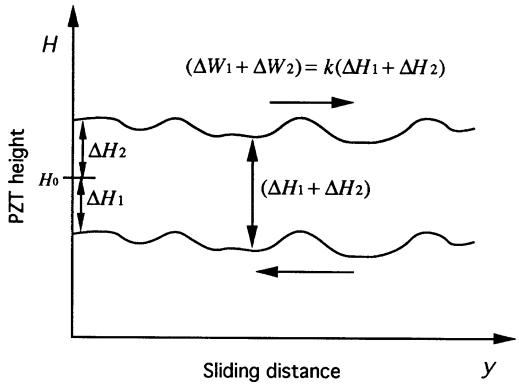

Fig. 2.21 Schematic illustration of the height difference of the piezoelectric tube scanner as the sample is scanned in y and −y directions

$$\mu = \frac{W_f}{W_0} = \left[\frac{(\Delta H_1 + \Delta H_2)}{H_0}\right]\left(\frac{L}{2\ell}\right) \qquad (2.5)$$

Since the piezo tube vertical position is affected by the surface topographic profile of the sample in addition to the friction force being applied at the tip, this difference has to be taken point by point at the same location on the sample

surface as shown in Fig. 2.21. Subtraction of point by point measurements may introduce errors, particularly for rough samples. We will come back to this point later. In addition, precise measurement of L and ℓ (which should include the cantilever angle) are also required.

If the adhesive forces between the tip and the sample are large enough that it can not be neglected, one should include it in the calculation. However, there could be a large uncertainty in determining this force, thus an uncertainty in using Eq. (2.5). An alternative approach is to make the measurements at different normal loads and to use $\Delta(H_0)$ and Δ $(\Delta H_1 + \Delta H_2)$ from the measurements in Eq. (2.5). Another comment on Eq. (2.5) is that, since only the ratio between $(\Delta H_1 + \Delta H_2)$ and H_0 comes into this equation, the piezo tube vertical position H_0 and its position difference $(\Delta H_1 + \Delta H_2)$ can be in the units of volts as long as the vertical traveling distance of the piezo tube and the voltage applied to it has a linear relationship. However, if there is a large nonlinearity between the piezo tube traveling distance and the applied voltage, this nonlinearity must be included in the calculation.

It should also be pointed out that, Eqs. (2.4) and (2.5) are derived under the assumption that the friction force W_f is the same for the two scanning directions of the sample. This is an approximation since the normal force is slightly different for the two scans and there may also be a directionality effect in friction. However, this difference is much smaller than W_0 itself. We can ignore the second order correction.

Method 2 ("aux" mode with perpendicular scan) to measure friction was suggested by Meyer and Amer (1990b). The sample is scanned perpendicular to the long axis of the cantilever beam (i.e., to scan along the x or −x direction in Fig. 2.19a) and the output of the horizontal two quadrants of the photodiode-detector is measured. In this arrangement, as the sample moves under the tip, the friction force will cause the cantilever to twist. Therefore the light intensity between the left and right (L and R in Fig. 2.19b, right) detectors will be different. The differential signal between the left and right detectors is denoted as FFM signal [(L − R)/(L + R)]. This signal can be related to the degree of twisting, hence to the magnitude of friction force. Again, because of a possible error in determining normal force due to the presence of an adhesive force at the tip-sample interface, the slope of the friction data (FFM signal vs. normal load) needs to be taken for an accurate value of coefficient of friction.

While friction force contributes to the FFM signal, friction force may not be the only contributing factor in commercial FFM instruments. One can notice this fact by simply engaging the cantilever tip with the sample. Before engaging, the left and right detectors can be balanced by adjusting the position of the detectors so that the intensity difference between these two detectors is zero (FFM signal is zero). Once the tip is engaged with the sample, this signal is no longer zero even if the sample is not moving in the xy plane with no friction force applied. This would be a detrimental effect. It has to be understood and eliminated from the data acquisition before any quantitative measurement of friction force becomes possible.

One of the fundamental reasons for this observation is the following. The detectors may not have been properly aligned with respect to the laser beam. To be precise, the vertical axis of the detector assembly (the line joining T-B in Fig. 2.22) is not in the plane defined by the incident laser beam and the beam reflected from an untwisted cantilever (we call this plane "beam plane"). When the cantilever vertical deflection changes due to a change of applied normal force (without having the sample scanned in the xy plane), the laser beam will be reflected up and down and form a projected trajectory on the detector. (Note that this trajectory is in the defined beam plane). If this trajectory is not coincident with the vertical axis of the detector, the laser beam will not evenly bisect the left and right quadrants of the detectors, even under the condition of no torsional motion of the cantilever, see Fig. 2.22. Thus when the laser beam is reflected up and down due a change of the normal force, the intensity difference between the left and right detectors will also change. In other words, the FFM signal will change as the normal

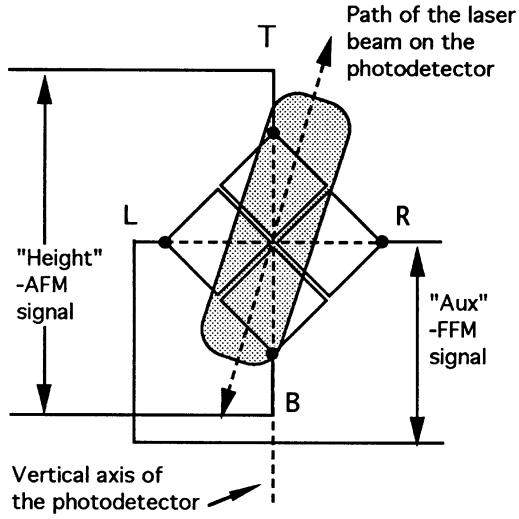

Fig. 2.22 The trajectory of the laser beam on the photodetectors in as the cantilever is vertically deflected (with no torsional motion) for a misaligned photodetector with respect to the laser beam. For a change of normal force (vertical deflection of the cantilever), the laser beam is projected at a different position on the detector. Due to a misalignment, the projected trajectory of the laser beam on the detector is not parallel with the detector vertical axis (the line joint T-B) (Ruan and Bhushan 1994a)

force applied to the tip is changed, even if the tip is not experiencing any friction force. This (FFM) signal is unrelated to friction force or to the actual twisting of the cantilever. We will call this part of FFM signal "FFM_F," and the part which is truly related to friction force "FFM_T".

The FFM_F signal can be eliminated. One way of doing this is as follows. First the sample is scanned in both x and −x directions and the FFM signal for scans in each direction is recorded. Since friction force reverses its directions when the scanning direction is reversed from x to −x direction, the FFM_T signal will have opposite signs as the scanning direction of the sample is reversed (FFM_T (x) = −FFM_T (−x)). Hence, the FFM_T signal will be canceled out if we take the sum of the FFM signals for the two scans. The average value of the two scans will be related to FFM_F due to the misalignment,

$$FFM(x) + FFM(-x) = 2FFM_F \tag{2.6}$$

This value can therefore be subtracted from the original FFM signals of each of these two scans to obtain the true FFM signal (FFM_T). Or, alternately, by taking the difference of the two FFM signals, one directly gets the FFM_T value

$$\begin{aligned} FFM(x) - FFM(-x) &= FFM_T(x) - FFM_T(-x) \\ &= 2FFM_T(x) \end{aligned} \tag{2.7}$$

Ruan and Bhushan (1994a) have been shown that error signal (FFM_F) can be very large compared to friction signal FFM_T, thus correction is required.

Now we compare the two methods. The method of using "height" mode and parallel scan (method 1) is very simple to use. Technically, this method can provide 3D friction profiles and the corresponding topographic profiles. However, there are some problems with this method. Under most circumstances, the piezo scanner displays a hysteresis when the traveling direction of the sample is reversed. Therefore the measured surface topographic profiles will be shifted relative to each other along the y-axis for the two opposite (y and −y) scans. This would make it difficult to measure the local height difference of the piezo tube for the two scans. However, the average height difference between the two scans and hence the average friction can still be measured. The measurement of average friction can serve as an internal means of friction force calibration. Method 2 is a more desirable approach. The subtraction of FFM_F signal from FFM for the two scans does not introduce error to local friction force data. An ideal approach in using this method would be to add the average value of the two profiles in order to get the error component (FFM_F) and then subtract this component from either profiles to get true friction profiles in either directions. By making measurements at various loads, we can get the average value of the

coefficient of friction which then can be used to convert the friction profile to the coefficient of friction profile. Thus any directionality and local variations in friction can be easily measured. In this method, since topography data are not affected by friction, accurate topography data can be measured simultaneously with friction data and better localized relationship between the two can be established.

2.3.5 Normal Force and Friction Force Calibrations of Cantilever Beams

Based on Ruan and Bhushan (1994a), we now discuss normal force and friction force calibrations. In order to calculate the absolute value of normal and friction forces in Newtons using the measured AFM and FFM_T voltage signals, it is necessary to first have an accurate value of the spring constant of the cantilever (k_c). The spring constant can be calculated using the geometry and the physical properties of the cantilever material (Albrecht et al. 1990; Meyer and Amer 1990b; Sarid and Elings 1991). However, the properties of the PECVD Si_3N_4 (used in fabricating cantilevers) could be different from those of bulk material. For example, by using an ultrasonic measurement, we found the Young's modulus of the cantilever beam to be about 238 ± 18 GPa which is less than that of bulk Si_3N_4 (310 GPa). Furthermore the thickness of the beam is nonuniform and difficult to measure precisely. Since the stiffness of a beam goes as the cube of thickness, minor errors in precise measurements of thickness can introduce substantial stiffness errors. Thus one should experimentally measure the spring constant of the cantilever. Cleveland et al. (1993) measured the normal spring constant by measuring resonant frequencies of the beams.

For normal spring constant measurement, Ruan and Bhushan (1994a) used a stainless steel spring sheet of known stiffness (width = 1.35 mm, thickness = 15 μm, free hanging length = 5.2 mm). One end of the spring was attached to the sample holder and the other end was made to contact with the cantilever tip during the measurement, see Fig. 2.23. They measured the piezo traveling distance for a given cantilever deflection. For a rigid sample (such as diamond), the piezo traveling distance Z_t (measured from the point where the tip touches the sample)

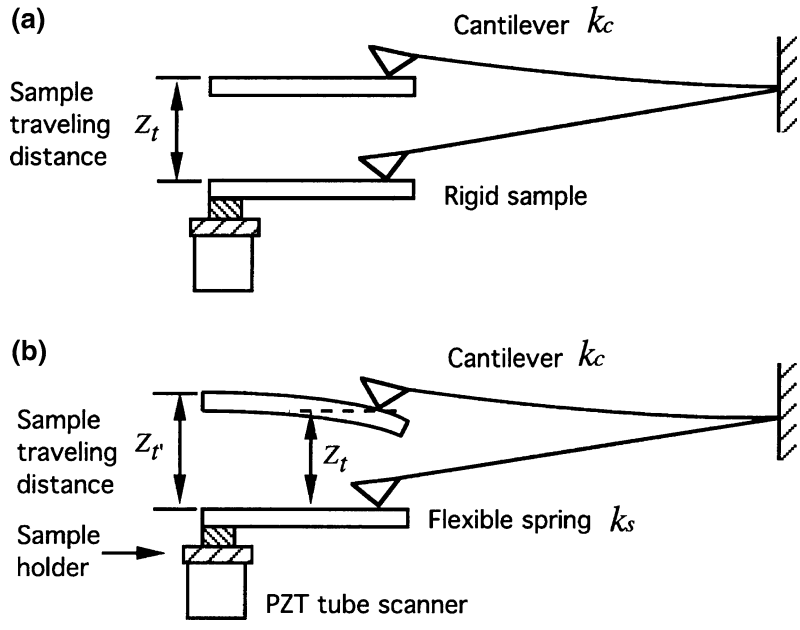

Fig. 2.23 Illustration showing the deflection of cantilever as it is pushed by (**a**) a rigid sample or by (**b**) a flexible spring sheet (Ruan and Bhushan 1994a)

should equal the cantilever deflection. To keep the cantilever deflection at the same level using a flexible spring sheet, the new piezo traveling distance $Z_{t'}$ would be different from Z_t. The difference between $Z_{t'}$ and Z_t corresponds to the deflection of the spring sheet. If the spring constant of the spring sheet is k_c, the spring constant of the cantilever k_c can be calculated by

$$(Z_{t'} - Z_t)k_s = Z_t\, k_c$$

or

$$k_c = \frac{k_S(Z_{t'} - Z_t)}{Z_t} \tag{2.8}$$

The spring constant of the spring sheet (k_s) used in this study is calculated to be 1.54 N/m. For a wide-legged cantilever used in our study (length = 115 μm, base width = 122 μm, leg width = 21 μm, and thickness = 0.6 μm), k_c was measured to be 0.40 N/m instead of 0.58 N/m reported by its manufacturer—Digital Instruments Inc. To relate photodiode detector output to the cantilever deflection in nm, they used the same rigid sample to push against the AFM tip. Since for a rigid sample the cantilever vertical deflection equals the sample traveling distance measured from the point where the tip touches the sample, the photodiode output as the tip is pushed by the sample can be converted directly to cantilever deflection. For these measurements, they found the conversion factor to be 20 nm/V.

The normal force applied to the tip can be calculated by multiplying the cantilever vertical deflection by the cantilever spring constant for samples which have very small adhesive force with the tip. If the adhesive force between the sample and the tip is large, it should be included in the normal force calculation. This is particularly important in atomic-scale force measurement because in this region, the typical normal force that is measured is in the range of a few hundreds of nN to a few mN. The adhesive force could be comparable to the applied force.

The conversion of friction signal (from FFM_T to friction force) is not as straightforward. For example, one can calculate the degree of twisting for a given friction force using the geometry and the physical properties of the cantilever (Meyer and Amer 1988; O'Shea et al. 1992). One would need the information on the detectors such as the quantum efficiency of the detector, the laser power, the instrument's gain, etc. in order to be able convert the signal into the degree of twisting. Generally speaking, this procedure cannot be accomplished without having some detailed information about the instrument. This information is not usually provided by the manufactures. Even if this information is readily available, error may still occur in using this approach because there will always be variations as a result of the instrumental set up. For example, it has been noticed that the measured FFM_T signal could be different for the same sample when different AFM microscopes of the same kind are used. The essence is that, one cannot calibrate the instrument experimentally using this calculation. O'Shea et al. (1992) did perform a calibration procedure in which the torsional signal was measured as the sample is displaced a known distance laterally while ensuring that the tip does not slide over the surface. However, it is difficult to verify if the tip sliding does not occur.

Apparently, a new method of calibration is required. There is a more direct and simpler way of doing this. The first method described (method 1) to measure friction can directly provide an absolute value of coefficient of friction. It can therefore be used just as an internal means of calibration for the data obtained using method 2. Or for a polished sample which introduces least error in friction measurement using method 1, method 1 can be used to obtain calibration for friction force for method 2. Then this calibration can be used for measurement on all samples using method 2. In method 1, the length of the cantilever required can be measured using an optical microscope; the length of the tip can be measured using a scanning electron microscope. The relative angle between the cantilever and the horizontal sample surface can be measured directly. Thus the coefficient of friction can be measured with few unknown parameters. The friction force can then be calculated by

multiplying the coefficient of friction by the normal load. The FFM_T signal obtained using method 2 can then be converted into friction force. For their instrument, they found the conversion to be 8.6 nN/V.

2.4 AFM Instrumentation and Analyses

The performance of AFMs and the quality of AFM images greatly depend on the instrument available and the probes (cantilever and tips) in use. This section describes the mechanics of cantilevers, instrumentation and analysis of force detection systems for cantilever deflections, and scanning and control systems.

2.4.1 The Mechanics of Cantilevers

2.4.1.1 Stiffness and Resonances of Lumped Mass Systems

Any one of the building blocks of an AFM, be it the body of the microscope itself or the force measuring cantilevers, are mechanical resonators. These resonances can be excited either by the surrounding or by the rapid movement of the tip or the sample. To avoid problems due to building or air induced oscillations, it is of paramount importance to optimize the design of the AFMs for high resonant frequencies. This usually means to decrease the size of the microscope (Pohl 1986). By using cube-like or sphere-like structures for the microscope, one can considerably increase the lowest eigen-frequency. The fundamental natural frequency, ω_0, of any spring is given by

$$\omega_0 = \frac{1}{2\pi}\sqrt{\frac{k}{m_{eff}}} \tag{2.9}$$

where k is the spring constant (stiffness) in the normal direction and m_{eff} is the effective mass. The spring constant k of a cantilever beam with uniform cross section (Fig. 2.24) is given by (Thomson and Dahleh 1998)

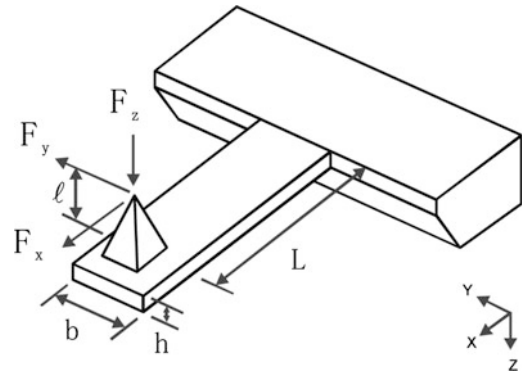

Fig. 2.24 A typical AFM cantilever with length L, width b, and height h. The height of the tip is ℓ. The material is characterized by Young's modulus E, the shear modulus G and a mass density ρ. Normal (F_z), axial (F_x), and lateral (F_y) forces exist at the end of the tip

$$k = \frac{3EI}{L^3} \tag{2.10}$$

where E is the Young's modulus of the material, L is the length of the beam and I is the moment of inertia of the cross section. For a rectangular cross section with a width b (perpendicular to the deflection) and a height h one obtains an expression for I

$$I = \frac{bh^3}{12} \tag{2.11}$$

Combining Eqs. (2.9), (2.10) and (2.11) we get an expression for ω_0

$$\omega_0 = \sqrt{\frac{Ebh^3}{4L^3 m_{eff}}} \tag{2.12}$$

The effective mass can be calculated using Raleigh's method. The general formula using Raleigh's method for the kinetic energy T of a bar is

$$T = \frac{1}{2}\int_0^L \frac{m}{L}\left(\frac{\partial z(x)}{\partial t}\right)^2 dx \tag{2.13}$$

For the case of a uniform beam with a constant cross section and length L one obtains for the deflection $z(x) = z_{max}[1 - (3x/2L) +$

$(x^3/2L^3)]$. Inserting z_{max} into Eq. (2.13) and solving the integral gives

$$T = \frac{1}{2}\int_0^L \frac{m}{L}\left[\frac{\partial z_{max}(x)}{\partial t}\left(1 - \frac{3x}{2L}\right) + \left(\frac{x^3}{L^3}\right)\right]^2 dx = \frac{1}{2} m_{eff} (z_{max} t)^2$$

which gives

$$m_{eff} = \frac{9}{20} m \tag{2.14}$$

Substituting the Eq. (2.14) into Eq. (2.12) and noting that m = ρLbh, where ρ is the mass density, one obtains the following expression

$$\omega_0 = \left(\frac{\sqrt{5}}{3}\sqrt{\frac{E}{\rho}}\right)\frac{h}{L^2} \tag{2.15}$$

It is evident from Eq. (2.15), that one way to increase the natural frequency is to choose a material with a high ratio E/ρ; see Table 2.2 for typical values of $\sqrt{E/\rho}$ of various commonly used materials. Another way to increase the lowest eigen-frequency is also evident in Eq. (2.15). By optimizing the ratio h/L^2, one can increase the resonant frequency. However it does not help to make the length of the structure smaller than the width or height. Their roles will just be interchanged. Hence the optimum structure is a cube. This leads to the design rule, that long, thin structures like sheet metal should be avoided. For a given resonant frequency, the quality factor Q should be as low as possible. This means that an inelastic medium such as rubber should be in contact with the structure to convert kinetic energy into heat.

2.4.1.2 Stiffness and Resonances of Cantilevers

Cantilevers are mechanical devices specially shaped to measure tiny forces. The analysis given in the previous section is applicable. However, to understand better the intricacies of force detection systems we will discuss the example of a cantilever beam with uniform cross section, Fig. 2.24. The bending of a beam due to a normal load on the beam is governed by the Euler equation (Thomson and Dahleh 1998)

$$M = EI(x)\frac{d^2 z}{dx^2} \tag{2.16}$$

where M is the bending moment acting on the beam cross section. I(x) the moment of inertia of the cross section with respect to the neutral axis defined by

$$I(x) = \int_z \int_y z^2 dy dz \tag{2.17}$$

For a normal force F_z acting at the tip,

$$M(x) = (L - x)F_z \tag{2.18}$$

since the moment must vanish at the endpoint of the cantilever. Integrating Eq. (2.16) for a normal force F_z acting at the tip and observing that EI is a constant for beams with a uniform cross section, one gets

$$z(x) = \frac{L^3}{6EI}\left(\frac{x}{L}\right)^2\left(3 - \frac{x}{L}\right)F_z \tag{2.19}$$

The slope of the beam is

$$z'(x) = \frac{Lx}{2EI}\left(2 - \frac{x}{L}\right)F_z \tag{2.20}$$

From Eqs. (2.19) and (2.20), at the end of the cantilever, i.e. for x = L, for a rectangular beam, and by using an expression for I in Eq. (2.11), one gets,

$$z(L) = \frac{4}{Eb}\left(\frac{L}{h}\right)^3 F_z \tag{2.21}$$

$$z'(L) = \frac{3}{2}\left(\frac{z}{L}\right) \tag{2.22}$$

Now the stiffness in the normal (z) direction, k_z, is

$$k_z = \frac{F_z}{z(L)} = \frac{Eb}{4}\left(\frac{h}{L}\right)^3 \tag{2.23}$$

and a change in angular orientation of the end of cantilever beam is

$$\Delta\alpha = \frac{3}{2}\frac{z}{L} = \frac{6}{Ebh}\left(\frac{L}{h}\right)^2 F_z \tag{2.24}$$

Now we ask what will, to first order, happen if we apply a lateral force F_y to the end of the tip (Fig. 2.24). The cantilever will bend sideways and it will twist. The stiffness in the lateral (y) direction, k_y, can be calculated with Eq. (2.23) by exchanging b and h

$$k_y = \frac{Eh}{4}\left(\frac{b}{L}\right)^3 \tag{2.25}$$

Therefore the bending stiffness in lateral direction is larger than the stiffness for bending in the normal direction by $(b/h)^2$. The twisting or torsion on the other side is more complicated to handle. For a wide, thin cantilever ($b \gg h$) we obtain torsional stiffness along y axis, k_{yT}

$$k_{yT} = \frac{Gbh^3}{3L\ell^2} \tag{2.26}$$

where G is the modulus of rigidity [=E/2(1 + ν), where ν is the Poisson's ratio]. The ratio of the torsional stiffness to the lateral bending stiffness is

$$\frac{k_{yT}}{k_y} = \frac{1}{2}\left(\frac{\ell b}{hL}\right)^2 \tag{2.27}$$

where we assume ν = 0.333. We see that thin, wide cantilevers with long tips favor torsion while cantilevers with square cross sections and short tips favor bending. Finally we calculate the ratio between the torsional stiffness and the normal bending stiffness,

$$\frac{k_{yT}}{k_z} = 2\left(\frac{L}{\ell}\right)^2 \tag{2.28}$$

Equations (2.26) to (2.28) hold in the case where the cantilever tip is exactly in the middle axis of the cantilever. Triangular cantilevers and cantilevers with tips not on the middle axis can be dealt with by finite element methods.

The third possible deflection mode is the one from the force on the end of the tip along the cantilever axis, F_x (Fig. 2.24). The bending moment at the free end of the cantilever is equal to the $F_x\ell$. This leads to the following modification of Eq. (2.18) for the case of forces F_z and F_x

$$M(x) = (L - x)F_z + F_x\ell \tag{2.29}$$

Integration of Eq. (2.16) now leads to

$$z(x) = \frac{1}{2EI}\left[Lx^2\left(1 - \frac{x}{3L}\right)F_z + \ell x^2 F_x\right] \tag{2.30}$$

and

$$z'(x) = \frac{1}{EI}\left[\frac{Lx}{2}\left(2 - \frac{x}{L}\right)F_z + \ell x F_x\right] \tag{2.31}$$

Evaluating Eqs. (2.30) and (2.31) at the end of the cantilever, we get the deflection and the tilt

$$z(L) = \frac{L^2}{EI}\left(\frac{L}{3}F_z - \frac{\ell}{2}F_x\right) \tag{2.32}$$

$$z'(x) = \frac{L}{EI}\left(\frac{L}{2}F_z + \ell F_x\right)$$

From these equations, one gets

$$F_z = \frac{12\,EI}{L^3}\left(z(L) - \frac{Lz'(L)}{2}\right) \tag{2.33}$$

$$F_x = \frac{2EI}{\ell L^2}(2Lz'(L) - 3z(L))$$

A second class of interesting properties of cantilevers is their resonance behavior. For cantilever beams one can calculate the resonant frequencies (Colchero 1993; Thomson and Dahleh 1998)

$$\omega_n^{free} = \frac{\lambda_n^2}{2\sqrt{3}} \frac{h}{L^2} \sqrt{\frac{E}{\rho}} \tag{2.34}$$

with $\lambda_0 = (0.596864\ldots)\pi$, $\lambda_1 = (1.494175\ldots)\pi$, $\lambda_n \rightarrow (n + 1/2)\pi$. The subscript n represents the order of the frequency, e.g., fundamental, second mode, and the nth mode.

A similar equation as Eq. (2.34) holds for cantilevers in rigid contact with the surface. Since there is an additional restriction on the movement of the cantilever, namely the location of its end point, the resonant frequency increases. Only the λ_n's terms change to (Colchero 1993)

$$\begin{aligned} \lambda_0' &= (1.2498763\ldots)\pi,\ \lambda_1' \\ &= (2.2499997\ldots)\pi,\ \lambda_n' \rightarrow (n + 1/4)\pi \end{aligned} \tag{2.35}$$

The ratio of the fundamental resonant frequency in contact to the fundamental resonant frequency not in contact is 4.3851.

For the torsional mode we can calculate the resonant frequencies as

$$\omega_0^{tors} = 2\pi \frac{h}{Lb} \sqrt{\frac{G}{\rho}} \tag{2.36}$$

For cantilevers in rigid contact with the surface, we obtain the expression for the fundamental resonant frequency (Colchero 1993)

$$\omega_0^{tors,contact} = \frac{\omega_0^{tors}}{\sqrt{1 + 3(2L/b)^2}} \tag{2.37}$$

The amplitude of the thermally induced vibration can be calculated from the resonant frequency using

$$\Delta z_{therm} = \sqrt{\frac{k_b T}{k}} \tag{2.38}$$

where k_b is Boltzmann's constant and T is the absolute temperature. Since AFM cantilevers are resonant structures, sometimes with rather high Q, the thermal noise is not evenly distributed as Eq. (2.38) suggests. The spectral noise density below the peak of the response curve is (Colchero 1993)

$$z_0 = \sqrt{\frac{4k_b T}{k\omega_0 Q}} \quad \left\{ in\ \mathrm{m}/\sqrt{\mathrm{Hz}} \right\} \tag{2.39}$$

where Q is the quality factor of the cantilever, described earlier.

2.4.2 Instrumentation and Analyses of Detection Systems for Cantilever Deflections

A summary of selected detection systems was provided in Fig. 2.8. Here we discuss in detail pros and cons of various systems.

2.4.2.1 Optical Interferometer Detection Systems

Interferometers

Soon after the first papers on the AFM (Binnig et al. 1986), which used a tunneling sensor, an instrument based on an interferometer was published (McClelland et al. 1987). The sensitivity of the interferometer depends on the wavelength of the light employed in the apparatus. Figure 2.25 shows the principle of such an interferometeric design. The light incident from the left is focused by a lens on the cantilever. The reflected light is collimated by the same lens and interferes with the light reflected at the flat. To separate the reflected light from the incident light a λ/4 plate converts the linear polarized incident light to circular polarization. The reflected light is made linear polarized again by the λ/4-plate, but with a polarization orthogonal to that of the incident light. The polarizing beam splitter then deflects the reflected light to the photo diode.

Homodyne Interferometer

To improve the signal to noise ratio of the interferometer the cantilever is driven by a piezo near its resonant frequency. The amplitude Δz of the cantilever as a function of driving frequency Ω is

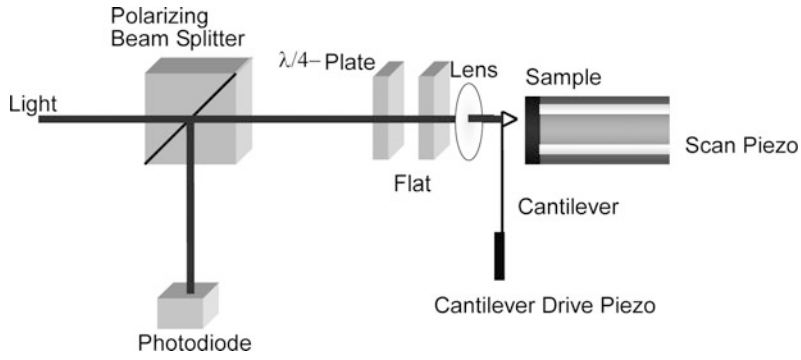

Fig. 2.25 Principle of an interferometric AFM. The light of the laser light source is polarized by the polarizing beam splitter and focused on the back of the cantilever. The light passes twice through a quarter wave plate and is hence orthogonally polarized to the incident light. The second arm of the interferometer is formed by the flat. The interference pattern is modulated by the oscillating cantilever

$$\Delta z(\Omega) = \Delta z_0 \frac{\Omega_0^2}{\sqrt{\left(\Omega^2 - \Omega_0^2\right)^2 + \frac{\Omega^2 \Omega_0^2}{Q^2}}} \tag{2.40}$$

where Δz_0 is the constant drive amplitude and Ω_0 the resonant frequency of the cantilever. The resonant frequency of the cantilever is given by the effective potential

$$\Omega_0 = \sqrt{\left(k + \frac{\partial^2 U}{\partial z^2}\right)\frac{1}{m_{eff}}} \tag{2.41}$$

where U is the interaction potential between the tip and the sample. Equation (2.41) shows that an attractive potential decreases Ω_0. The change in Ω_0 in turn results in a change of the Δz (see Eq. (2.40)). The movement of the cantilever changes the path difference in the interferometer. The light reflected from the cantilever with the amplitude $A_{\ell,0}$ and the reference light with the amplitude $A_{r,0}$ interfere on the detector. The detected intensity $I(t) = \{A_\ell(t) + A_r(t)\}^2$ consists of two constant terms and a fluctuating term

$$2A_\ell(t)A_r(t) = A_{\ell,0}A_{r,0}\sin\left[\omega t + \frac{4\pi\delta}{\lambda} + \frac{4\pi\Delta z}{\lambda}\sin(\Omega t)\right]\sin(\omega t) \tag{2.42}$$

Here ω is the frequency of the light, λ is the wavelength of the light, δ is the path difference in the interferometer, and Δz is the instantaneous amplitude of the cantilever, given according to Eqs. (2.40) and (2.41) as a function of Ω, k, and U. The time average of Eq. (2.42) then becomes

$$\begin{aligned}\langle 2A_\ell(t)A_r(t)\rangle_T &\propto \cos\left[\frac{4\pi\delta}{\lambda} + \frac{4\pi\Delta z}{\lambda}\sin(\Omega t)\right] \\ &\approx \cos\left(\frac{4\pi\delta}{\lambda}\right) - \sin\left[\frac{4\pi\Delta z}{\lambda}\sin(\Omega t)\right] \\ &\approx \cos\left(\frac{4\pi\delta}{\lambda}\right) - \frac{4\pi\Delta z}{\lambda}\sin(\Omega t)\end{aligned} \tag{2.43}$$

Here all small quantities have been omitted and functions with small arguments have been linearized. The amplitude of Δz can be recovered with a lock-in technique. However, Eq. (2.43) shows that the measured amplitude is also a function of the path difference δ in the interferometer. Hence this path difference δ must be very stable. The best sensitivity is obtained when $\sin(4\delta/\lambda) \approx 0$.

Heterodyne Interferometer

This influence is not present in the heterodyne detection scheme shown in Fig. 2.26. Light incident from the left with a frequency ω is split in a reference path (upper path in Fig. 2.26) and a

measurement path. Light in the measurement path is shifted in frequency to $\omega_1 = \omega + \Delta\omega$ and focused on the cantilever. The cantilever oscillates at the frequency Ω, as in the homodyne detection scheme. The reflected light $A_\ell(t)$ is collimated by the same lens and interferes on the photo diode with the reference light $A_r(t)$. The fluctuating term of the intensity is given by

$$2A_\ell(t)A_r(t) = A_{\ell,0}A_{r,0}\,\sin\left[(\omega+\Delta\omega)t + \frac{4\pi\delta}{\lambda} + \frac{4\pi\Delta z}{\lambda}\sin(\Omega t)\right]\,\sin(\omega t) \quad (2.44)$$

where the variables are defined as in Eq. (2.42). Setting the path difference $\sin(4\pi\delta/\lambda) \approx 0$ and taking the time average, omitting small quantities and linearizing functions with small arguments we get

$$\begin{aligned}
\langle 2A_\ell(t)A_r(t)\rangle_T &\propto \cos\left[\Delta\omega t + \frac{4\pi\delta}{\lambda} + \frac{4\pi\Delta z}{\lambda}\sin(\Omega t)\right]\\
&= \cos\left(\Delta\omega t + \frac{4\pi\delta}{\lambda}\right)\cos\left[\frac{4\pi\Delta z}{\lambda}\sin(\Omega t)\right]\\
&\quad - \sin\left(\Delta\omega t + \frac{4\pi\delta}{\lambda}\right)\sin\left[\frac{4\pi\Delta z}{\lambda}\sin(\Omega t)\right]\\
&\approx \cos\left(\frac{4\pi\delta}{\lambda}\right) - \sin\left[\frac{4\pi\Delta z}{\lambda}\sin(\Omega t)\right]\\
&\approx \cos\left(\Delta\omega t + \frac{4\pi\delta}{\lambda}\right)\left[1 - \frac{8\pi^2\Delta z^2}{\lambda^2}\sin(\Omega t)\right]\\
&\quad - \frac{4\pi\Delta z}{\lambda}\sin\left(\Delta\omega t + \frac{4\pi\delta}{\lambda}\right)\sin(\Omega t)\\
&= \cos\left(\Delta\omega t + \frac{4\pi\delta}{\lambda}\right) - \frac{8\pi^2\Delta z^2}{\lambda^2}\cos\left(\Delta\omega t + \frac{4\pi\delta}{\lambda}\right)\sin(\Omega t)\\
&\quad - \frac{4\pi\Delta z}{\lambda}\sin\left(\Delta\omega t + \frac{4\pi\delta}{\lambda}\right)\sin(\Omega t)\\
&= \cos\left(\Delta\omega t + \frac{4\pi\delta}{\lambda}\right) - \frac{4\pi^2\Delta z^2}{\lambda^2}\cos\left(\Delta\omega t + \frac{4\pi\delta}{\lambda}\right)\\
&\quad + \frac{4\pi^2\Delta z^2}{\lambda^2}\cos\left(\Delta\omega t + \frac{4\pi\delta}{\lambda}\right)\cos(2\Omega t)\\
&\quad - \frac{4\pi\Delta z}{\lambda}\sin\left(\Delta\omega t + \frac{4\pi\delta}{\lambda}\right)\sin(\Omega t)\\
&= \cos\left(\Delta\omega t + \frac{4\pi\delta}{\lambda}\right)\left(1 - \frac{4\pi^2\Delta z^2}{\lambda^2}\right)\\
&\quad + \frac{2\pi^2\Delta z^2}{\lambda^2}\left\{\cos\left[(\Delta\omega+2\Omega)t + \frac{4\pi\delta}{\lambda}\right]\right.\\
&\quad \left. + \cos\left[(\Delta\omega-2\Omega)t + \frac{4\pi\delta}{\lambda}\right]\right\}\\
&\quad + \frac{2\pi\Delta z}{\lambda}\left\{\cos\left[(\Delta\omega+\Omega)t + \frac{4\pi\delta}{\lambda}\right] + \cos\left[(\Delta\omega-\Omega)t + \frac{4\pi\delta}{\lambda}\right]\right\}
\end{aligned} \quad (2.45)$$

Multiplying electronically the components oscillating at $\Delta\omega$ and $\Delta\omega + \Omega$ and rejecting any product except the one oscillating at Ω we obtain

$$\begin{aligned}
A &= \frac{2\Delta z}{\lambda}\left(1 - \frac{4\pi^2\Delta z^2}{\lambda^2}\right)\cos\left[(\Delta\omega+2\Omega)t + \frac{4\pi\delta}{\lambda}\right]\cos\left(\Delta\omega t + \frac{4\pi\delta}{\lambda}\right)\\
&= \frac{\Delta z}{\lambda}\left(1 - \frac{4\pi^2\Delta z^2}{\lambda^2}\right)\left\{\cos\left[(2\Delta\omega+\Omega)t + \frac{8\pi\delta}{\lambda}\right] + \cos(\Omega t)\right\}\\
&\approx \frac{\pi\Delta z}{\lambda}\cos(\Omega t)
\end{aligned} \quad (2.46)$$

Unlike in the homodyne detection scheme the recovered signal is independent from the path difference δ of the interferometer. Furthermore a lock-in amplifier with the reference set $\sin(\Delta\omega t)$ can measure the path difference δ independent of the cantilever oscillation. If necessary, a feedback circuit can keep $\delta = 0$.

Fiber-optical Interferometer

The fiber-optical interferometer (Rugar et al. 1989) is one of the simplest interferometers to build and use. Its principle is sketched in Fig. 2.27. The light of a laser is fed into an optical fiber. Laser diodes with integrated fiber pigtails are convenient light sources. The light is split in a fiber-optic beam splitter into two fibers. One fiber is terminated by index matching oil to avoid any reflections back into the fiber. The end of the other fiber is brought close to the cantilever in the AFM. The emerging light is partially reflected back into the fiber by the cantilever. Most of the light, however, is lost. This is not a big problem since only 4% of the light is reflected at the end of the fiber, at the glass-air interface. The two reflected light waves interfere with each other. The product is guided back into the fiber coupler and again split into two parts. One half is analyzed by the photodiode. The other half is fed back into the laser. Communications grade laser diodes are sufficiently resistant against feedback to be operated in this environment. They have, however, a bad coherence length, which in this case does not matter, since the optical path difference is in any case no larger than 5 µm. Again the end of the fiber has to be positioned on a piezo drive to set the distance between the fiber and the cantilever to $\lambda(n + 1/4)$.

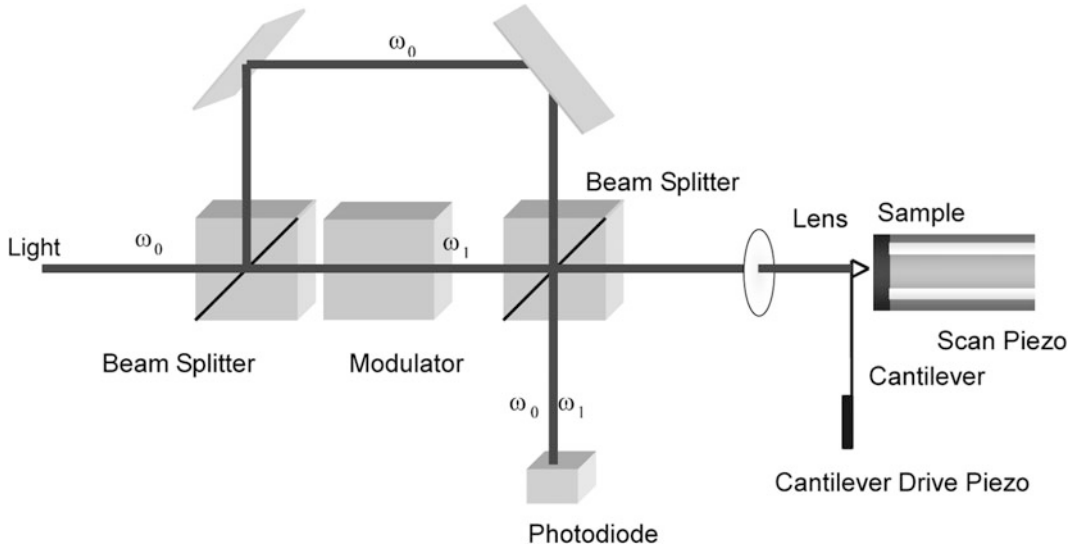

Fig. 2.26 Principle of a heterodyne interferometric AFM. Light with the frequency ω_0 is split into a reference path (upper path) and a measurement path. The light in the measurement path is frequency shifted to ω_1 by an acousto-optical modulator (or an electro-optical modulator). The light reflected from the oscillating cantilever interferes with the reference beam on the detector

Nomarski-Interferometer

Another solution to minimize the optical path difference is to use the Nomarski interferometer (Schoenenberger and Alvarado 1989). Figure 2.28 shows a schematic of the microscope. The light of a laser is focused on the cantilever by lens. A birefringent crystal (for instance calcite) between the cantilever and the lens with its optical axis 45° off the polarization direction of the light splits the light beam into two paths, offset by a distance given by the length of the crystal. Birefringent crystals have varying indexes of refraction. In calcite, one crystal axis has a lower index than the other two. This means, that certain light rays will propagate at a different speed through the crystal than the others. By choosing a correct polarization, one can select the ordinary ray, the extraordinary ray

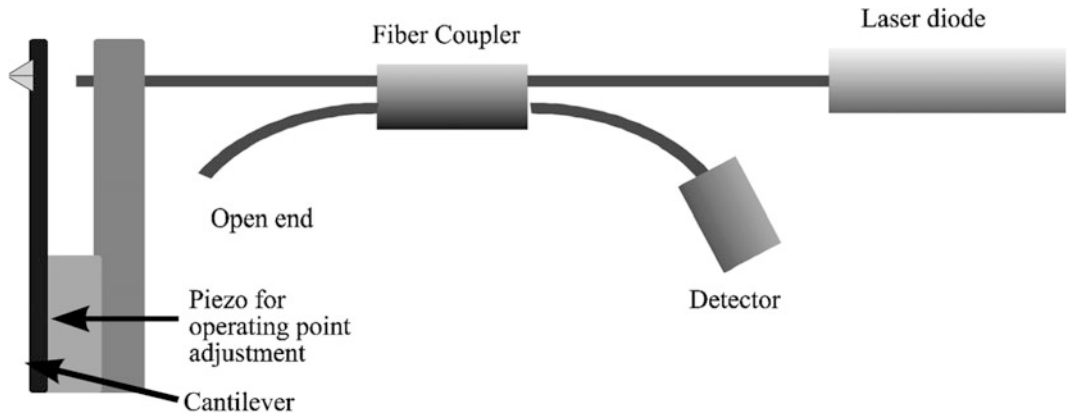

Fig. 2.27 A typical setup for a fiber optic interferometer readout

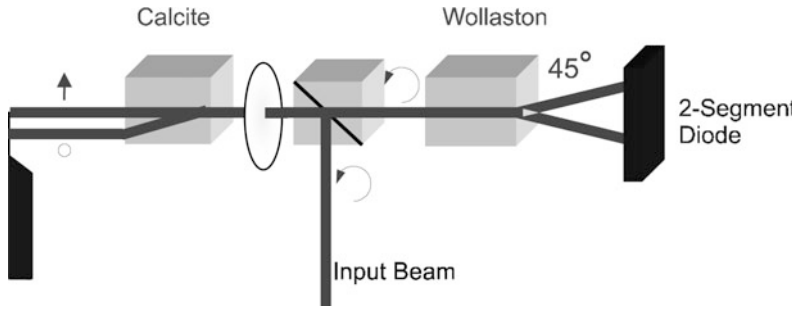

Fig. 2.28 Principle of Nomarski AFM. The circular polarized input beam is deflected to the *left* by a non-polarizing beam splitter. The light is focused onto a cantilever. The calcite crystal between the lens and the cantilever splits the circular polarized light into two spatially separated beams with orthogonal polarizations. The two light beams reflected from the lever are superimposed by the calcite crystal and collected by the lens. The resulting beam is again circular polarized. A Wollaston prism produces two interfering beams with π/2 phase shift between them. The minimal path difference accounts for the excellent stability of this microscope

or one can get any distribution of the intensity amongst those two rays. A detailed description of birefringence can be found in textbooks (e.g., Shen 1984). A calcite crystal deflects the extraordinary ray at an angle of 6° within the crystal. By choosing a suitable length of the calcite crystal, any separation can be set.

The focus of one light ray is positioned near the free end of the cantilever while the other is placed close to the clamped end. Both arms of the interferometer pass through the same space, except for the distance between the calcite crystal and the lever. The closer the calcite crystal is placed to the lever, the less influence disturbances like air currents have.

Sensitivity

Sarid (1991) has given values for the sensitivity of the different interferometeric detection systems. Table 2.5 presents a summary of his results.

2.4.2.2 Optical Lever

The most common cantilever deflection detection system is the optical lever (Meyer and Amer 1988; Alexander et al. 1989). This method, depicted in Fig. 2.29, employs the same technique as light beam deflection galvanometers. A fairly well collimated light beam is reflected off a mirror and projected to a receiving target. Any change in the angular position of the mirror will change the position, where the light ray hits

Table 2.5 Noise in Interferometers

	Homodyne interferometer, fiber optic interferometer	Heterodyne interferometer	Nomarski interferometer
Laser noise $\langle \delta i^2 \rangle_L$	$\frac{1}{4}\eta^2 F^2 P_i^2\, RIN$	$\eta^2\left(P_R^2 + P_S^2\right) RIN$	$\frac{1}{16}\eta^2 P^2 \delta\theta$
Thermal noise $\langle \delta i^2 \rangle_T$	$\frac{16\pi^2}{\lambda^2}\eta^2 F^2 P_i^2 \frac{4k_B TBQ}{\omega_0 k}$	$\frac{4\pi^2}{\lambda^2}\eta^2 P_d^2 \frac{4k_B TBQ}{\omega_0 k}$	$\frac{\pi^2}{\lambda^2}\eta^2 P^2 \frac{4k_B TBQ}{\omega_0 k}$
Shot Noise $\langle \delta i^2 \rangle_S$	$4e\eta P_d B$	$2e\eta(P_R + P_S)B$	$\frac{1}{2}e\eta PB$

F is the finesse of the cavity in the homodyne interferometer, P_i the incident power, P_d is the power on the detector, η is the sensitivity of the photodetector and RIN is the relative intensity noise of the laser. P_R and P_S are the power in the reference and sample beam in the heterodyne interferometer. P is the power in the Nomarski interferometer, δθ is the phase difference between the reference and the probe beam in the Nomarski interferometer. B is the bandwidth, e is the electron charge, λ is the wavelength of the laser, k the cantilever stiffness, ω_o is the resonant frequency of the cantilever, Q is the quality factor of the cantilever, T is the temperature, and δi is the variation of current i

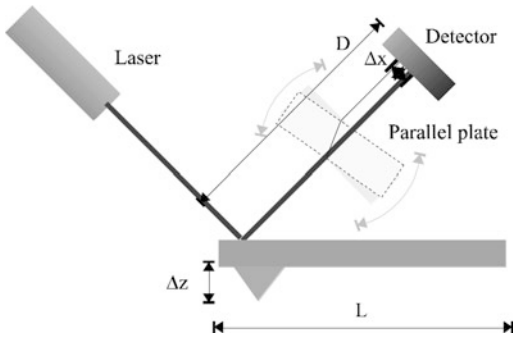

Fig. 2.29 The setup of optical lever detection microscope

the target. Galvanometers use optical path lengths of several meters and scales projected to the target wall as a read-out help.

For the AFM using the optical lever method a photodiode segmented into two (or four) closely spaced devices detects the orientation of the end of the cantilever. Initially, the light ray is set to hit the photodiodes in the middle of the two sub-diodes. Any deflection of the cantilever will cause an imbalance of the number of photons reaching the two halves. Hence the electrical currents in the photodiodes will be unbalanced too. The difference signal is further amplified and is the input signal to the feedback loop. Unlike the interferometeric AFMs, where often a modulation technique is necessary to get a sufficient signal to noise ratio, most AFMs employing the optical lever method are operated in a static mode. AFMs based on the optical lever method are universally used. It is the simplest method to construct an optical readout and it can be confined in volumes smaller than 5 cm on the side.

The optical lever detection system is a simple yet elegant way to detect normal and lateral force signals simultaneously (Meyer and Amer 1988, 1990b; Alexander et al. 1989; Marti et al. 1990). It has the additional advantage that it is the fact that it is a remote detection system.

Implementations

Light from a laser diode or from a super luminescent diode is focused on the end of the cantilever. The reflected light is directed onto a quadrant diode that measures the direction of the light beam. A Gaussian light beam far from its waist is characterized by an opening angle β. The deflection of the light beam by the cantilever surface tilted by an angle α is 2α. The intensity on the detector then shifts to the side by the product of 2α and the separation between the detector and the cantilever. The readout electronics calculates the difference of the photocurrents. The photocurrents in turn are proportional to the intensity incident on the diode.

The output signal is hence proportional to the change in intensity on the segments

$$I_{sig} \propto 4\frac{\alpha}{\beta} I_{tot} \tag{2.47}$$

For the sake of simplicity, we assume that the light beam is of uniform intensity with its cross section increasing proportional to the distance between the cantilever and the quadrant detector. The movement of the center of the light beam is then given by

$$\Delta x_{Det} = \Delta z \frac{D}{L} \tag{2.48}$$

The photocurrent generated in a photodiode is proportional to the number of incoming photons hitting it. If the light beam contains a total number of N_0 photons then the change in difference current becomes

$$\Delta(I_R - I_L) = \Delta I = const\, \Delta z D N_0 \tag{2.49}$$

Combining Eqs. (2.48) and (2.49), one obtains that the difference current ΔI is independent of the separation of the quadrant detector and the cantilever. This relation is true, if the light spot is smaller than the quadrant detector. If it is greater, the difference current ΔI becomes smaller with increasing distance. In reality the light beam has a Gaussian intensity profile. For small movements Δx (compared to the diameter of the light spot at the quadrant detector), Eq. (2.49) still holds. Larger movements Δx, however, will introduce a nonlinear response. If the AFM is operated in a constant force mode, only small movements Δx of the light spot will

occur. The feedback loop will cancel out all other movements.

The scanning of a sample with an AFM can twist the microfabricated cantilevers because of lateral forces (Mate et al. 1987; Marti et al. 1990; Meyer and Amer 1990b) and affect the images (den Boef 1991). When the tip is subjected to lateral forces, it will twist the cantilever and the light beam reflected from the end of the cantilever will be deflected perpendicular to the ordinary deflection direction. For many investigations this influence of lateral forces is unwanted. The design of the triangular cantilevers stems from the desire, to minimize the torsion effects. However, lateral forces open up a new dimension in force measurements. They allow, for instance, a distinction of two materials because of the different friction coefficient, or the determination of adhesion energies. To measure lateral forces the original optical lever AFM has to be modified. The only modification compared with Fig. 2.29 is the use of a quadrant detector photodiode instead of a two-segment photodiode and the necessary readout electronics, see Fig. 2.9a. The electronics calculates the following signals:

$$\begin{aligned} U_{Normal\ Force} &= \alpha\left[\left(I_{Upper\ Left} + I_{Upper\ Right}\right)\right. \\ &\quad \left. - \left(I_{Lower\ Left} + I_{Lower\ Right}\right)\right] \\ U_{Lateral\ Force} &= \beta\left[\left(I_{Upper\ Left} + I_{Lower\ Left}\right)\right. \\ &\quad \left. - \left(I_{Upper\ Right} + I_{Lower\ Right}\right)\right] \end{aligned} \tag{2.50}$$

The calculation of the lateral force as a function of the deflection angle does not have a simple solution for cross-sections other than circles. An approximate formula for the angle of twist for rectangular beams is (Baumeister and Marks 1967)

$$\theta = \frac{M_t L}{\beta G b^3 h} \tag{2.51}$$

where $M_t = F_y \ell$ is the external twisting moment due to lateral force, F_y, and β a constant determined by the value of h/b. For the equation to hold, h has to be larger than b.

Inserting the values for a typical microfabricated cantilever with integrated tips

$$\begin{aligned} b &= 6 \times 10^{-7}\ \text{m} \\ h &= 10^{-5}\ \text{m} \\ L &= 10^{-4}\ \text{m} \\ \ell &= 3.3 \times 10^{-6}\ \text{m} \\ G &= 5 \times 10^{10}\ \text{Pa} \\ \beta &= 0.333 \end{aligned} \tag{2.52}$$

into Eq. (2.51) we obtain the relation

$$F_y = 1.1 \times 10^{-4}\, N \times \theta \tag{2.53}$$

Typical lateral forces are of order 10^{-10} N.

Sensitivity

The sensitivity of this setup has been calculated in various papers (Colchero et al. 1991; Sarid 1991; Colchero 1993). Assuming a Gaussian beam the resulting output signal as a function of the deflection angle is dispersion like. Equation (2.47) shows that the sensitivity can be increased by increasing the intensity of the light beam I_{tot} or by decreasing the divergence of the laser beam. The upper bound of the intensity of the light I_{tot} is given by saturation effects on the photodiode. If we decrease the divergence of a laser beam we automatically increase the beam waist. If the beam waist becomes larger than the width of the cantilever we start to get diffraction. Diffraction sets a lower bound on the divergence angle. Hence one can calculate the optimal beam waist w_{opt} and the optimal divergence angle β (Colchero et al. 1991; Colchero 1993)

$$\begin{aligned} w_{opt} &\approx 0.36\, b \\ \theta_{opt} &\approx 0.89 \frac{\lambda}{b} \end{aligned} \tag{2.54}$$

The optimal sensitivity of the optical lever then becomes

$$\varepsilon[\text{mW/rad}] = 1.8 \frac{b}{\lambda} I_{tot}[\text{mW}] \tag{2.55}$$

The angular sensitivity optical lever can be measured by introducing a parallel plate into the beam. A tilt of the parallel plate results in a displacement of the beam, mimicking an angular deflection.

Additional noise source can be considered. Of little importance is the quantum mechanical uncertainty of the position (Colchero et al. 1991; Colchero 1993), which is for typical cantilevers at room temperature

$$\Delta z = \sqrt{\frac{\hbar}{2m\omega_0}} = 0.05 \text{ fm} \qquad (2.56)$$

where $\hbar$ is the Planck constant (=6.626 × 10^{-34} Js). At very low temperatures and for high frequency cantilevers this could become the dominant noise source. A second noise source is the shot noise of the light. The shot noise is related to the particle number. We can calculate the number of photons incident on the detector

$$n = \frac{I\tau}{\hbar\omega} = \frac{I\lambda}{2\pi B\hbar c} = 1.8 \times 10^9 \frac{I[\text{W}]}{B[\text{Hz}]} \qquad (2.57)$$

where I is the intensity of the light, τ the measurement time, B = 1/τ the bandwidth, and c the speed of light. The shot noise is proportional to the square root of the number of particles. Equating the shot noise signal with the signal resulting for the deflection of the cantilever one obtains

$$\Delta z_{shot} = 68 \frac{L}{w} \sqrt{\frac{B[\text{kHz}]}{I[\text{mW}]}} [\text{fm}] \qquad (2.58)$$

where w is the diameter of the focal spot. Typical AFM setups have a shot noise of 2 pm. The thermal noise can be calculated from the equipartition principle. The amplitude at the resonant frequency is

$$\Delta z_{therm} = 129 \sqrt{\frac{B}{k[\text{N/m}]\omega_0 Q}} [\text{pm}] \qquad (2.59)$$

A typical value is 16 pm. Upon touching the surface, the cantilever increases its resonant frequency by a factor of 4.39. This results in a new thermal noise amplitude of 3.2 pm for the cantilever in contact with the sample.

2.4.2.3 Piezoresistive Detection

Implementations

An alternative detection system which is not as widely spread as the optical detection schemes are piezoresistive cantilevers (Ashcroft and Mermin 1976; Stahl et al. 1994; Kassing and Oesterschulze 1997). These cantilevers are based on the fact that the resistivity of certain materials, in particular of Si, changes with the applied stress. Figure 2.30 shows a typical implementation of a piezo-resistive cantilever. Four resistances are integrated on the chip, forming a Wheatstone bridge. Two of the resistors are in unstrained parts of the cantilever, the other two are measuring the bending at the point of the maximal deflection. For instance when an AC voltage is applied between terminals a and c one can measure the detuning of the bridge between terminals b and d. With such a connection the output signal varies only due to bending, but not due to changing of the ambient temperature and thus the coefficient of the piezoresistance.

Sensitivity

The resistance change is (Kassing and Oesterschulze 1997)

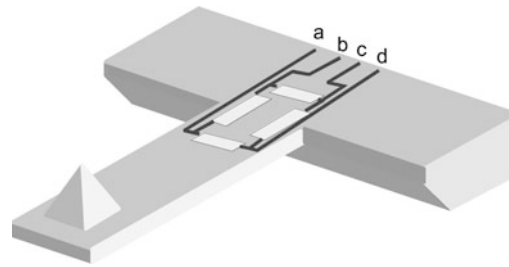

Fig. 2.30 A typical setup for a piezoresistive readout

$$\frac{\Delta R}{R_0} = \Pi\delta \tag{2.60}$$

where Π is the tensor element of the piezo-resistive coefficients, δ the mechanical stress tensor element and R_0 the equilibrium resistance. For a single resistor they separate the mechanical stress and the tensor element in longitudinal and transversal components

$$\frac{\Delta R}{R_0} = \Pi_t\delta_t + \Pi_\ell\delta_\ell \tag{2.61}$$

The maximum value of the stress components are $\Pi_t = -64.0 \times 10^{-11}$ m^2/N and $\Pi_\ell = -71.4\ 10^{-11}$ m^2/N for a resistor oriented along the (110) direction in silicon (Kassing and Oesterschulze 1997). In the resistor arrangement of Fig. 2.30, two of the resistors are subject to the longitudinal piezo-resistive effect and two of them are subject to the transverse piezo-resistive effect. The sensitivity of that setup is about four times that of a single resistor, with the advantage that temperature effects cancel to first order. The resistance change is then calculated as

$$\frac{\Delta R}{R_0} = \Pi\frac{3Eh}{2L^2}\Delta z = \Pi\frac{6L}{bh^2}F_z \tag{2.62}$$

where $\Pi = 67.7 \times 10^{-11}$ m^2/N is the averaged piezo-resistive coefficient. Plugging in typical values for the dimensions (Fig. 2.24) (L = 100 µm, b = 10 µm, h = 1 µm) one obtains

$$\frac{\Delta R}{R_0} = \frac{4 \times 10^{-5}}{nN}F_z \tag{2.63}$$

The sensitivity can be tailored by optimizing the dimensions of the cantilever.

2.4.2.4 Capacitance Detection

The capacitance of an arrangement of conductors depends on the geometry. Generally speaking, the capacitance increases for decreasing separations. Two parallel plates form a simple capacitor (see Fig. 2.31, upper left), with the capacitance

$$C = \frac{\varepsilon\varepsilon_0 A}{x} \tag{2.64}$$

where A is the area of the plates, assumed equal, and x is the separation. Alternatively, one can consider a sphere versus an infinite plane (see Fig. 2.31, lower left). Here the capacitance is (Sarid 1991)

$$C = 4\pi\varepsilon_0 R\sum_{n=2}^{\infty}\frac{\sin h(\alpha)}{\sin h(n\alpha)} \tag{2.65}$$

where R is the radius of the sphere, and α is defined by

$$\alpha = \ln\left[1 + \frac{z}{R} + \sqrt{\frac{z^2}{R^2} + 2\frac{z}{R}}\right] \tag{2.66}$$

One has to keep in mind that capacitance of a parallel plate capacitor is a nonlinear function of the separation. Using a voltage divider one can circumvent this problem. Figure 2.32a shows a low pass filter. The output voltage is given by

$$U_{out} = U_{\approx}\frac{\frac{1}{j\omega C}}{R + \frac{1}{j\omega C}} = U_{\approx}\frac{1}{J\omega CR + 1} \cong \frac{U_{\approx}}{J\omega CR} \tag{2.67}$$

Here, $U_{\approx}$ is the driving voltage, C is given by Eq. (2.64), ω is the excitation frequency and j is

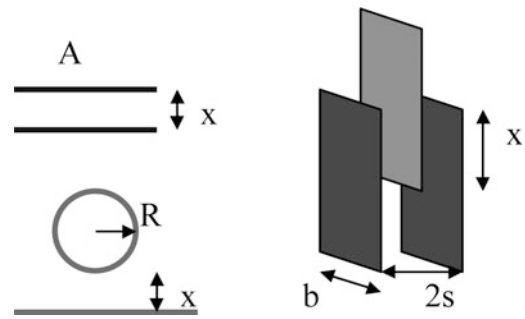

Fig. 2.31 Three possible arrangements of a capacitive readout. The *upper left* shows the cross section through a parallel plate capacitor. The *lower left* shows the geometry sphere versus plane. The *right side* shows the more complicated, but linear capacitive readout

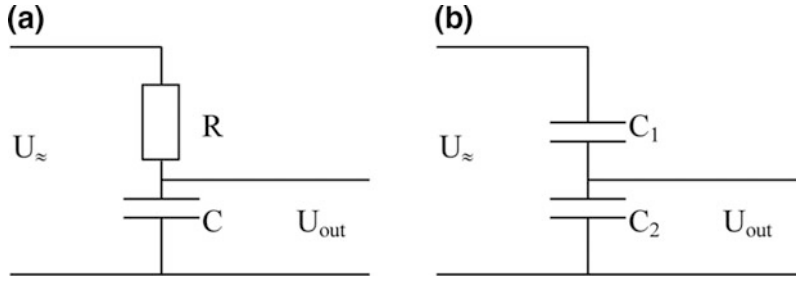

Fig. 2.32 Measuring the capacitance. The *left side*, (**a**) shows a low pass filter, the *right side*, (**b**) shows a capacitive divider. C (*left*) or C_2 (*right*) are the capacitances under test

the imaginary unit. The approximate relation in the end is true when $\omega CR \gg 1$. This is equivalent to the statement that C is fed by a current source, since R must be large in this setup. Plugging Eq. (2.64) into Eq. (2.67) and neglecting the phase information one obtains

$$U_{out} = \frac{U_{\approx} x}{\omega R \varepsilon \varepsilon_0 A} \tag{2.68}$$

which is linear in the displacement x.

Figure 2.32b shows a capacitive divider. Again the output voltage U_{out} is given by

$$U_{out} = U_{\approx} \frac{C_1}{C_2 + C_1} = U_{\approx} \frac{C_1}{\frac{\varepsilon \varepsilon_0 A}{x} + C_1} \tag{2.69}$$

If there is a stray capacitance C_s then Eq. (2.69) is modified as

$$U_{out} = U_{\approx} \frac{C_1}{\frac{\varepsilon \varepsilon_0 A}{x} + C_s + C_1} \tag{2.70}$$

Provided $C_s + C_1 \ll C_2$ one has a system which is linear in x. The driving voltage $U_{\approx}$ has to be large (more than 100 V) to have the output voltage in the range of 1 V. The linearity of the readout depends on the capacitance C_1 (Fig. 2.33).

Another idea is to keep the distance constant and to change the relative overlap of the plates (see Fig. 2.31, right side). The capacitance of the

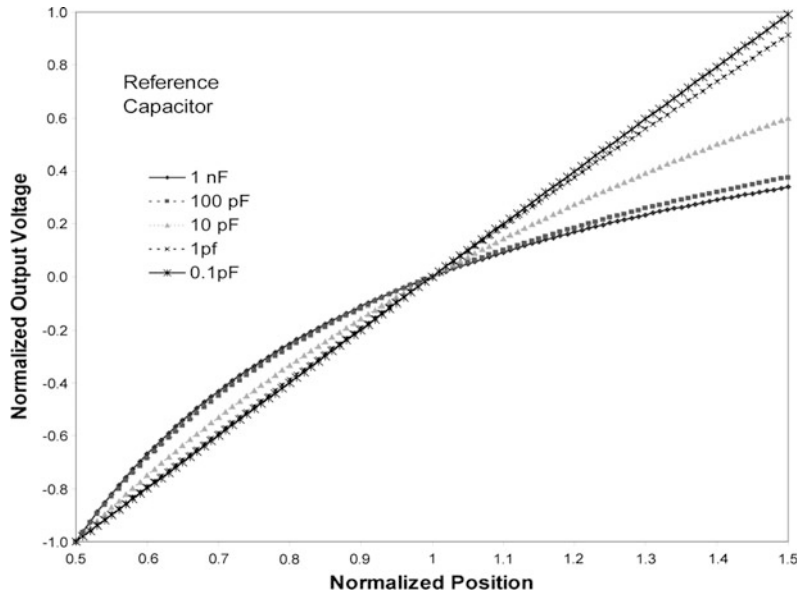

Fig. 2.33 Linearity of the capacitance readout as a function of the reference capacitor

moving center plate versus the stationary outer plates becomes

$$C = C_s + 2\frac{\varepsilon\,\varepsilon_0 bx}{S} \tag{2.71}$$

where the variables are defined in Fig. 2.31. The stray capacitance comprises all effects, including the capacitance of the fringe fields. When length x is comparable to the width b of the plates one can safely assume that the stray capacitance is constant, independent of x. The main disadvantage of this setup is that it is not as easily incorporated in a microfabricated device as the others.

Sensitivity

The capacitance itself is not a measure of the sensitivity, but its derivative is indicative of the signals one can expect. Using the situation described in Fig. 2.31, upper left, and in Eq. (2.64) one obtains for the parallel plate capacitor

$$\frac{dC}{dx} = -\frac{\varepsilon\,\varepsilon_0 A}{x^2} \tag{2.72}$$

Assuming a plate area A of 20 µm by 40 µm and a separation of 1 µm one obtains a capacitance of 31 fF (neglecting stray capacitance and the capacitance of the connection leads) and a dC/dx of 3.1×10^{-8} F/m = 31 fF/µm. Hence it is of paramount importance to maximize the area between the two contacts and to minimize the distance x. The latter however is far from being trivial. One has to go to the limits of microfabrication to achieve a decent sensitivity.

If the capacitance is measured by the circuit shown in Fig. 2.32 one obtains for the sensitivity

$$\frac{dU_{out}}{U_{\approx}} = \frac{dx}{\omega R\varepsilon\,\varepsilon_0 A} \tag{2.73}$$

Using the same value for A as above, setting the reference frequency to 100 kHz, and selecting R = 1 GΩ, we get the relative change of the output voltage U_{out} to

$$\frac{dU_{out}}{U_{\approx}} = \frac{22.5 \times 10^{-6}}{\mathring{\mathrm{A}}} \times dx \tag{2.74}$$

A driving voltage of 45 V then translates to a sensitivity of 1 mV/Å. A problem in this setup is the stray capacitances. They are in parallel to the original capacitance and decrease the sensitivity considerably.

Alternatively one could build an oscillator with this capacitance and measure the frequency. RC-oscillators typically have an oscillation frequency of

$$f_{res} \propto \frac{1}{RC} = \frac{x}{R\varepsilon\,\varepsilon_0 A} \tag{2.75}$$

Again the resistance R must be of the order of 1 GΩ, when stray capacitances C_s are neglected. However C_s is of the order of 1 pF. Therefore one gets R = 10 MΩ. Using these values the sensitivity becomes

$$df_{res} = \frac{Cdx}{R(C + C_s)^2 x} \approx \frac{0.1\,\mathrm{Hz}}{\mathring{\mathrm{A}}} dx \tag{2.76}$$

The bad thing is that the stray capacitances have made the signal nonlinear again. The linearized setup in Fig. 2.31 has a sensitivity of

$$\frac{dC}{dx} = 2\frac{\varepsilon\,\varepsilon_0 b}{s} \tag{2.77}$$

Substituting typical values, b = 10 µm, s = 1 µm one gets dC/dx = 1.8×10^{-10} F/m. It is noteworthy that the sensitivity remains constant for scaled devices.

Implementations

The readout of the capacitance can be done in different ways (Neubauer et al. 1990; Goddenhenrich et al. 1990). All include an alternating current or voltage with frequencies in the 100 kHz to the 100 MHz range. One possibility is to build a tuned circuit with the capacitance of the cantilever determining the frequency. The resonance frequency of a high quality Q tuned circuit is

$$\omega_0 = (LC)^{-\frac{1}{2}} \tag{2.78}$$

where L is the inductance of the circuit. The capacitance C includes not only the sensor capacitance but also the capacitance of the leads. The precision of a frequency measurement is mainly determined by the ratio of L and C

$$Q = \left(\frac{L}{C}\right)^{\frac{1}{2}} \frac{1}{R} \tag{2.79}$$

Here R symbolizes the losses in the circuit. The higher the quality the more precise the frequency measurement. For instance a frequency of 100 MHz and a capacitance of 1 pF gives an inductance of 250 μH. The quality becomes then 2.5×10^8. This value is an upper limit, since losses are usually too high.

Using a value of dC/dx = 31 fF/μm one gets ΔC/Å = 3.1 aF/Å. With a capacitance of 1 pF one gets

$$\frac{\Delta\omega}{\omega} = \frac{1}{2}\frac{\Delta C}{C}$$
$$\Delta\omega = 100\ \text{MHz} \times \frac{1}{2}\frac{3.1\ \text{aF}}{1\ \text{pF}} = 155\ \text{Hz} \tag{2.80}$$

This is the frequency shift for 1 Å deflection. The calculation shows, that this is a measurable quantity. The quality also indicates that there is no physical reason why this scheme should not work.

2.4.3 Combinations for 3D-Force Measurements

Three dimensional force measurements are essential if one wants to know all the details of the interaction between the tip and the cantilever. The straightforward attempt to measure three forces is complicated, since force sensors such as interferometers or capacitive sensors need a minimal detection volume, which often is too large. The second problem is that the force-sensing tip has to be held by some means. This implies that one of the three Cartesian axes is stiffer than the others.

However by the combination of different sensors one can achieve this goal. Straight cantilevers are employed for these measurements, because they can be handled analytically. The key observation is, that the optical lever method does not determine the position of the end of the cantilever. It measures the orientation. In the previous sections, one has always made use of the fact, that for a force along one of the orthogonal symmetry directions at the end of the cantilever (normal force, lateral force, force along the cantilever beam axis) there is a one to one correspondence of the tilt angle and the deflection. The problem is, that the force along the cantilever beam axis and the normal force create a deflection in the same direction. Hence what is called the normal force component is actually a mixture of two forces. The deflection of the cantilever is the third quantity, which is not considered in most of the AFMs. A fiber optic interferometer in parallel to the optical lever measures the deflection. Three measured quantities then allow the separation of the three orthonormal force directions, as is evident from Eqs. (2.27) and (2.33) (Fujisawa et al. 1994a, b; Grafstrom et al. 1994; Overney et al. 1994; Warmack et al. 1994).

Alternatively one can put the fast scanning direction along the axis of the cantilever. Forward and backward scans then exert opposite forces F_x. If the piezo movement is linearized, both force components in AFM based on the optical lever detection can be determined. In this case, the normal force is simply the average of the forces in the forward and backward direction. The force form the front, F_x, is the difference of the forces measured in forward and backward direction.

2.4.4 Scanning and Control Systems

Almost all SPMs use piezo translators to scan the tip or the sample. Even the first STM (Binnig et al. 1982; Binnig and Rohrer 1983) and some of the predecessor instruments (Young et al. 1971, 1972) used them. Other materials or setups

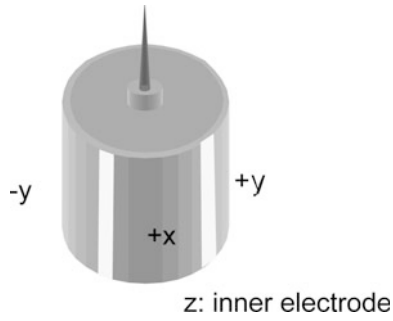

Fig. 2.34 Schematic drawing of a piezoelectric tube scanner. The piezo ceramic is molded into a tube form. The outer electrode is separated into four segments and connected to the scanning voltages. The z-voltage is applied to the inner electrode

for nano-positioning have been proposed, but were not successful (Gerber and Marti 1985; Garcìa Cantù and Huerta Garnica 1990).

2.4.4.1 Piezo Tubes

A popular solution is tube scanners (Fig. 2.34). They are now widely used in SPMs due to their simplicity and their small size (Binnig and Smith 1986; Chen 1992a). The outer electrode is segmented in four equal sectors of 90°. Opposite sectors are driven by signals of the same magnitude, but opposite sign. This gives, through bending, a two-dimensional movement on, approximately, a sphere. The inner electrode is normally driven by the z signal. It is possible, however, to use only the outer electrodes for scanning and for the z-movement. The main drawback of applying the z-signal to the outer electrodes is, that the applied voltage is the sum of both the x- or y-movement and the z-movement. Hence a larger scan size effectively reduces the available range for the z-control.

2.4.4.2 Piezo Effect

An electric field applied across a piezoelectric material causes a change in the crystal structure, with expansion in some directions and contraction in others. Also, a net volume change occurs (Ashcroft and Mermin 1976). Many SPMs use the transverse piezo electric effect, where the applied electric field $\overrightarrow{E}$ is perpendicular to the expansion/contraction direction.

$$\Delta L = L\left(\overrightarrow{E} \cdot \vec{n}\right) d_{31} = L\frac{V}{t} d_{31} \tag{2.81}$$

where d_{31} is the transverse piezoelectric constant, V is the applied voltage, t is the thickness of the piezo slab or the distance between the electrodes where the voltage is applied, L is the free length of the piezo slab, and $\vec{n}$ is the direction of polarization. Piezo translators based on the transverse piezoelectric effect have a wide range of sensitivities, limited mainly by mechanical stability and breakdown voltage.

2.4.4.3 Scan Range

The calculation of the scanning range of a piezotube is difficult (Carr 1988; Chen 1992a, b). The bending of the tube depends on the electric fields and the nonuniform strain induced. A finite element calculation where the piezo tube was divided into 218 identical elements was used (Carr 1988) to calculate the deflection. On each node the mechanical stress, stiffness, strain and piezoelectric stress was calculated when a voltage was applied on one electrode. The results were found to be linear on the first iteration and higher-order corrections were very small even for large electrode voltages. It was found that to first order the x- and z-movement of the tube could be reasonably well approximated by assuming that the piezo tube is a segment of a torus. Using this model one obtains

$$dx = (V_+ - V_-)|d_{31}|\frac{L^2}{2td} \tag{2.82}$$

$$dz = (V_+ + V_- - 2V_z)|d_{31}|\frac{L}{2t} \tag{2.83}$$

where $|d_{31}|$ is the coefficient of the transversal piezoelectric effect, L is tube's free length, t is tube's wall thickness, d is tube's diameter, V_+ is voltage on positive outer electrode while V_- is voltage of the opposite quadrant negative electrode, and V_z is voltage of inner electrode. The

cantilever or sample mounted on the piezotube has an additional lateral movement because the point of measurement is not in the end plane of the piezotube. The additional lateral displacement of the end of the tip is $\ell \sin\varphi \approx \ell\varphi$, where ℓ is the tip length and φ is the deflection angle of the end surface. Assuming that the sample or cantilever are always perpendicular to the end of the walls of the tube and calculating with the torus model one gets for the angle

$$\varphi = \frac{L}{R} = \frac{2dx}{L} \tag{2.84}$$

where R is the radius of curvature the piezo tube. Using the result of Eq. (2.84) one obtains for the additional x-movement

$$dx_{add} = \ell\varphi = \frac{2dx\ell}{L} = (V_+ - V_-)|d_{31}|\frac{\ell L}{td} \tag{2.85}$$

and for the additional z-movement due to the x-movement

$$dz_{add} = \ell - \ell\cos\varphi = \frac{\ell\varphi^2}{2} = \frac{2\ell(dx)^2}{L^2} = (V_+ - V_-)^2|d_{31}|^2\frac{\ell L^2}{2t^2d^2} \tag{2.86}$$

Carr (1988) assumed for his finite element calculations that the top of the tube was completely free to move and, as a consequence, the top surface was distorted, leading to a deflection angle about half that of the geometrical model. Depending on the attachment of the sample or the cantilever this distortion may be smaller, leading to a deflection angle in-between that of the geometrical model and the one of the finite element calculation.

2.4.4.4 Nonlinearities and Creep

Piezo materials with a high conversion ratio, i.e. a large d_{31} or small electrode separations, with large scanning ranges are hampered by substantial hysteresis resulting in a deviation from linearity by more than 10%. The sensitivity of the piezo ceramic material (mechanical displacement divided by driving voltage) decreases with reduced scanning range, whereas the hysteresis is reduced. A careful selection of the material for the piezo scanners, the design of the scanners, and of the operating conditions is necessary to get optimum performance.

2.4.4.5 Linearization Strategies

Passive Linearization: Calculation

The analysis of images affected by piezo nonlinearities (Libioulle et al. 1991; Stoll 1991; Durselen et al. 1995; Fu 1995) shows that the dominant term is

$$x = AV + BV^2 \tag{2.87}$$

where x is the excursion of the piezo, V the applied voltage and A and B two coefficients describing the sensitivity of the material. Equation (2.87) holds for scanning from V = 0 to large V. For the reverse direction the equation becomes

$$x = \widetilde{A}V - \widetilde{B}(V - V_{max})^2 \tag{2.88}$$

where $\widetilde{A}$ and $\widetilde{B}$ are the coefficients for the back scan, and V_{max} is the applied voltage at the turning point. Both equations demonstrate the true x-travel is small at the beginning of the scan and becomes larger towards the end. Therefore images are stretched at the beginning and compressed at the end.

Similar equation hold for the slow scan direction. The coefficients, however, are different. The combined action causes a greatly distorted image. This distortion can be calculated. The data acquisition systems record the signal as a function of V. However the data is measured as a function of x. Therefore we have to distribute the x-values evenly across the image this can be done by inverting an approximation of Eq. (2.87). First we write

$$x = AV\left(1 - \frac{B}{A}V\right) \tag{2.89}$$

For B ≪ A we can approximate

$$V = \frac{x}{A} \tag{2.90}$$

We now substitute Eq. (2.90) into the non-linear term of Eq. (2.89). This gives

$$\begin{aligned} x &= AV\left(1 + \frac{Bx}{A^2}\right) \\ V &= \frac{x}{A}\frac{1}{(1 + Bx/A^2)} \approx \frac{x}{A}\left(1 - \frac{Bx}{A^2}\right) \end{aligned} \tag{2.91}$$

Hence an equation of the type

$$x_{true} = x(\alpha - \beta x/x_{max}) \quad \text{with } 1 = \alpha - \beta \tag{2.92}$$

takes out the distortion of an image. α and β are dependent on the scan range, the scan speed and on the scan history and have to be determined with exactly the same settings as for the measurement. x_{max} is the maximal scanning range. The condition for α and β guarantees that the image is transformed onto itself.

Similar equations as the empirical one shown above Eq. (2.92) can be derived by analyzing the movements of domain walls in piezo ceramics.

Passive Linearization: Measuring the Position

An alternative strategy is to measure the position of the piezo translators. Several possibilities exist.

(1) The interferometers described above can be used to measure the elongation of the piezo elongation. Especially the fiber optic interferometer is easy to implement. The coherence length of the laser only limits the measurement range. However the signal is of periodic nature. Hence a direct use of the signal in a feedback circuit for the position is not possible. However as a measurement tool and, especially, as a calibration tool the interferometer is without competition. The wavelength of the light, for instance in a HeNe laser is so well defined that the precision of the other components determines the error of the calibration or measurement.

(2) The movement of the light spot on the quadrant detector can be used to measure the position of a piezo (Barrett and Quate 1991). The output current changes by $0.5\,\frac{\mathrm{A}}{\mathrm{cm}} \times \frac{P[\mathrm{W}]}{R[\mathrm{cm}]}$. Typical values (P = 1 mW, R = 0.001 cm) give 0.5 A/cm. The noise limit is typically $0.15\,\mathrm{nm} \times \sqrt{\frac{\Delta f[\mathrm{Hz}]}{H[\mathrm{W/cm^2}]}}$. Again this means that the laser beam above would have a 0.1 nm noise limitation for a bandwidth of 21 Hz. The advantage of this method is that, in principle, one can linearize two axes with only one detector.

(3) A knife-edge blocking part of a light beam incident on a photodiode can be used to measure the position of the piezo. This technique, commonly used in optical shear force detection (Betzig et al. 1992; Toledo-Crow et al. 1992), has a sensitivity of better than 0.1 nm.

(4) The capacitive detection (Griffith et al. 1990; Holman et al. 1996) of the cantilever deflection can be applied to the measurement of the piezo elongation. Equations (2.64) to (2.79) apply to the problem. This technique is used in some commercial instruments. The difficulties lie in the avoidance of fringe effects at the borders of the two plates. While conceptually simple, one needs the latest technology in surface preparation to get a decent linearity. The electronic circuits used for the readout are often proprietary.

(5) Linear Variable Differential Transformers (LVDT) are a convenient means to measure positions down to 1 nm. They can be used together with a solid state joint setup, as often used for large scan range stages. Unlike the capacitive detection there are few difficulties to implementation. The sensors and the detection circuits LVDTs are available commercially.

(6) A popular measurement technique is the use of strain gauges. They are especially sensitive when mounted on a solid state joint where the curvature is maximal. The resolution depends mainly on the induced curvature. A precision of 1 nm is attainable. The signals are low—a Wheatstone bridge is needed for the readout.

Active Linearization

Active linearization is done with feedback systems. Sensors need to be monotonic. Hence all the systems described above, with the exception of the interferometers are suitable. The most common solutions include the strain gauge approach, the capacitance measurement or the LVDT, which are all electronic solutions. Optical detection systems have the disadvantage that the intensity enters into the calibration.

2.4.4.6 Alternative Scanning Systems

The first STMs were based on piezo tripods (Binnig et al. 1982). The piezo tripod (Fig. 2.35) is an intuitive way to generate the three dimensional movement of a tip attached to its center. However, to get a suitable stability and scanning range, the tripod needs to be fairly large (about 50 mm). Some instruments use piezo stacks instead of monolithic piezoactuators. They are arranged in the tripod arrangement. Piezo stacks are thin layers of piezoactive materials glued together to form a device with up to 200 µm of actuation range. Preloading with a suitable metal casing reduces the nonlinearity.

If one tries to construct a homebuilt scanning system, the use of linearized scanning tables is recommended. They are built around solid state joints and actuated by piezo stacks. The joints guarantee that the movement is parallel with little deviation from the predefined scanning plane. Due to the construction it is easy to add measurement devices such as capacitive sensors, LVDTs or strain gauges which are essential for a closed loop linearization. Two-dimensional tables can be bought from several manufacturers. They have a linearity of better than 0.1% and a noise level of 10^{-4}–10^{-5} of the maximal scanning range.

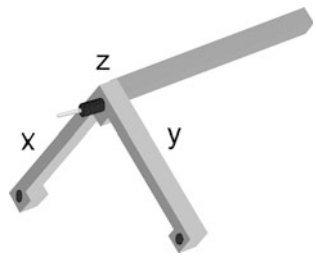

Fig. 2.35 An alternative type of piezo scanners: the tripod

2.4.4.7 Control Systems

Basics

The electronics and software play an important role in the optimal performance of an SPM. Control electronics and software are supplied with commercial SPMs. Control electronic systems can use either analog or digital feedback. While digital feedback offers greater flexibility and the ease of configuration, analog feedback circuits might be better suited for ultralow noise operation. We will describe here the basic setups for AFM.

Figure 2.36 shows a block schematic of a typical AFM feedback loop. The signal from the force transducer is fed into the feedback loop consisting mainly of a subtraction stage to get an error signal and an integrator. The gain of the integrator (high gain corresponds to short integration times) is set as high as possible without generating more than 1% overshoot. High gain minimizes the error margin of the current and forces the tip to follow the contours of constant density of states as good as possible. This operating mode is known as Constant Force Mode. A high voltage amplifier amplifies the outputs of the integrator. As AFMs using piezotubes usually require ±150 V at the output, the output of the integrator needs to be amplified by a high voltage amplifier.

In order to scan the sample, additional voltages at high tension are required to drive the piezo. For example, with a tube scanner, four scanning voltages are required, namely $+V_x$, $-V_x$, $+V_y$ and $-V_y$. The x- and y-scanning voltages are generated in a scan generator (analog or computer controlled). Both voltages are

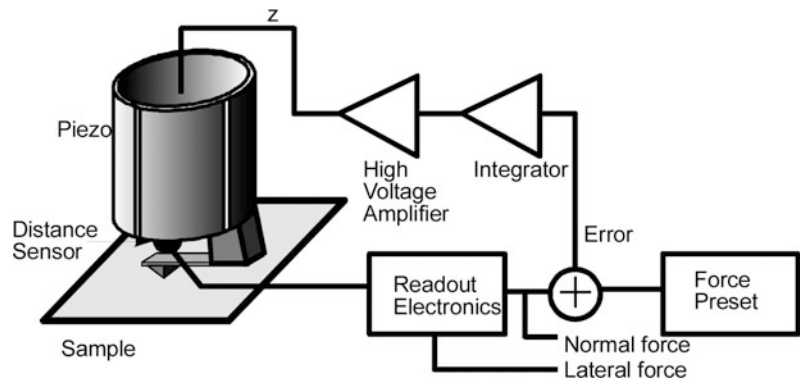

Fig. 2.36 Block schematic of the feedback control loop of an AFM

input to the two respective power amplifiers. Two inverting amplifiers generate the input voltages for the other two power amplifiers. The topography of the sample surface is determined by recording the input-voltage to the high voltage amplifier for the z-channel as a function of x and y (Constant Force Mode).

Another operating mode is the Variable Force Mode. The gain in the feedback loop is lowered and the scanning speed increased such that the force on the cantilever is not any more constant. Here the force is recorded as a function of x and y.

Force Spectroscopy

Four modes of spectroscopic imaging are in common use with force microscopes: measuring lateral forces, $\partial F/\partial z$, $\partial F/\partial x$ spatially resolved, and measuring force versus distance curves. Lateral forces can be measured by detecting the deflection of a cantilever in a direction orthogonal to the normal direction. The optical lever deflection method most easily does this. Lateral force measurements give indications of adhesion forces between the tip and the sample.

$\partial F/\partial z$ measurements probe the local elasticity of the sample surface. In many cases the measured quantity originates from a volume of a few cubic nanometers. The $\partial F/\partial z$ or local stiffness signal is proportional to Young's modulus, as far as one can define this quantity. Local stiffness is measured by vibrating the cantilever by a small amount in z-direction. The expected signal for very stiff samples is zero: for very soft samples one gets, independent of the stiffness, also a constant signal. This signal is again zero for the optical lever deflection and equal to the driving amplitude for interferometeric measurements. The best sensitivity is obtained when the compliance of the cantilever matches the stiffness of the sample.

A third spectroscopic quantity is the lateral stiffness. It is measured by applying a small modulation in the x-direction on the cantilever. The signal is again optimal when the lateral compliance of the cantilever matches the lateral stiffness of the sample. The lateral stiffness is, in turn, related to the shear modulus of the sample.

Detailed information on the interaction of the tip and the sample can be gained by measuring force versus distance curves. It is necessary to have cantilevers with high enough compliance to avoid instabilities due to the attractive forces on the sample.

Using the Control Electronics as a Two-Dimensional Measurement Tool

Usually the control electronics of an AFM is used to control the x- and y-piezo signals while several data acquisition channels record the position dependent signals. The control electronics can be used in another way: it can be viewed as a two-dimensional function generator. What is normally the x- and y-signal can be used to control two independent variables of an experiment. The control logic of the AFM then ensures that the available parameter space is systematically probed at equally spaced points.

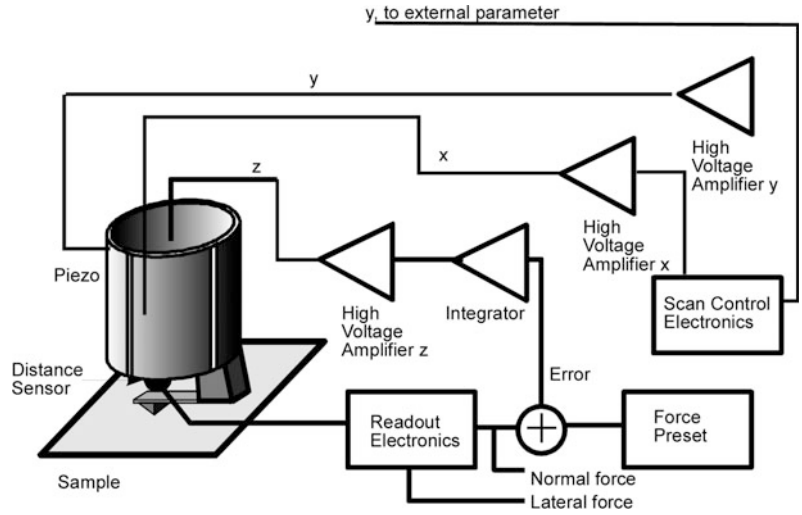

Fig. 2.37 Wiring of an AFM to measure friction force curves along a line

An example is friction force curves measured along a line across a step on graphite.

Figure 2.37 shows the connections. The z-piezo is connected as usual, like the x-piezo. However the y-output is used to command the desired input parameter. The offset of the y-channel determines the position of the tip on the sample surface, together with the x-channel.

2.4.4.8 Some Imaging Processing Methods

The visualization and interpretation of images from AFMs is intimately connected to the processing of these images. An ideal AFM is a noise-free device that images a sample with perfect tips of known shape and has perfect linear scanning piezos. In reality, AFMs are not that ideal. The scanning device in AFMs is affected by distortions. The distortions are both linear and nonlinear. Linear distortions mainly result from imperfections in the machining of the piezotranslators causing crosstalk from the Z-piezo to the X- and Y-piezos, and vice versa. Among the linear distortions, there are two kinds which are very important. First, scanning piezos invariably have different sensitivities along the different scan axes due to the variation of the piezo material and uneven sizes of the electrode areas. Second, the same reasons might cause the scanning axes not to be orthogonal. Furthermore, the plane in which the piezoscanner moves for constant height z is hardly ever coincident with the sample plane. Hence, a linear ramp is added to the sample data. This ramp is especially bothersome when the height z is displayed as an intensity map.

The nonlinear distortions are harder to deal with. They can affect AFM data for a variety of reasons. First, piezoelectric ceramics do have a hysteresis loop, much like ferromagnetic materials. The deviations of piezoceramic materials from linearity increase with increasing amplitude of the driving voltage. The mechanical position for one voltage depends on the previously applied voltages to the piezo. Hence, to get the best position accuracy, one should always approach a point on the sample from the same direction. Another type of nonlinear distortion of the images occurs when the scan frequency approaches the upper frequency limit of the X- and Y-drive amplifiers or the upper frequency limit of the feedback loop (z-component). This distortion, due to feedback loop, can only be minimized by reducing the scan frequency. On the other hand, there is a simple way to reduce distortions due to the X- and Y-piezo drive amplifiers. To keep the system as simple as possible, one normally uses a triangular waveform for driving the scanning piezos. However, triangular waves contain frequency components as multiples of the scan frequency. If the cutoff frequency of the X- and Y-drive electronics or of

the feedback loop is too close to the scanning frequency (two or three times the scanning frequency), the triangular drive voltage is rounded off at the turning points. This rounding error causes, first, a distortion of the scan linearity and, second, through phase lags, the projection of part of the backward scan onto the forward scan. This type of distortion can be minimized by carefully selecting the scanning frequency and by using driving voltages for the X- and Y-piezos with waveforms like trapezoidal waves, which are closer to a sine wave. The values measured for X, Y, or Z piezos are affected by noise. The origin of this noise can be either electronic, some disturbances, or a property of the sample surface due to adsorbates. In addition to this incoherent noise, interference with main and other equipment nearby might be present. Depending on the type of noise, one can filter it in the real space or in Fourier space. The most important part of image processing is to visualize the measured data. Typical AFM data sets can consist of many thousands to over a million points per plane. There may be more than one image plane present. The AFM data represents a topography in various data spaces.

Most commercial data acquisition systems use implicitly some kind of data processing. Since the original data is commonly subject to slopes on the surface, most programs use some kind of slope correction. The least disturbing way is to substrate a plane $z(x, y) = Ax + By + C$ from the data. The coefficients are determined by fitting $z(x, y)$ to the data. Another operation is to subtract a second order function such as $z(x, y) = Ax^2 + By^2 + Cxy + Dx + Ey + F$. Again, the parameters are determined with a fit. This function is appropriate for almost plane data, where the nonlinearity of the piezos caused such a distortion.

In the image processing software from Digital Instruments, up to three operations are performed on the raw data. First, a zero-order flatten is applied. The flatten operation is used to eliminate image bow in the slow scan direction (caused by physical bow in the instrument itself), slope in the slow scan direction, bands in the image (caused by differences in the scan height from one scan line to the next). The flatten operation takes each scan line and subtracts the average value of the height along each scan line from each point in that scan line. This brings each scan line to the same height. Next, a first-order planefit is applied in the fast scan direction. The planefit operation is used to eliminate bow and slope in the fast scan direction. The planefit operation calculated a best-fit plane for the image and subtracts it from the image. This plane has a constant non-zero slope in the fast scan direction. In some cases, higher-order polynomial "plane" may be required. Depending upon the quality of the raw data, the flatten operation and/or the planefit operation may not be required at all.

2.5 Closure

Since introduction of the STM in 1981 and AFM in 1985, many variations of probe-based microscopies, referred to as SPMs, have been developed. While the pure imaging capabilities of SPM techniques are dominated by the application of these methods at their early development stages, the physics of probe-sample interactions and the quantitative analyses of tribological, electronic, magnetic, biological, and chemical surfaces have now become of increasing interest. Nanoscale science and technology are strongly driven by SPMs which allow investigation and manipulation of surfaces down to the atomic scale. With growing understanding of the underlying interaction mechanisms, SPMs have found application in many fields outside basic research fields. In addition, various derivatives of all these methods have been developed for special applications, some of them targeting far beyond microscopy.

References

Abraham DW, Mamin HJ, Ganz E, Clark J (1986) Surface modification with the scanning tunneling microscope. IBM J Res Dev 30:492–499

Albrecht TR, Quate CF (1987) Atomic resolution imaging of a nonconductor by atomic force microscopy. J Appl Phys 62:2599–2602

Albrecht TR, Akamine S, Carver TE, Quate CF (1990) Microfabrication of cantilever styli for the atomic force microscope. J Vac Sci Technol A 8:3386–3396

Albrecht TR, Grutter P, Rugar D, Smith DPE (1992) Low temperature force microscope with all-fiber interferometer. Ultramicroscopy 42–44:1638–1646

Alexander S, Hellemans L, Marti O, Schneir J, Elings V, Hansma PK (1989) An atomic-resolution atomic-force microscope implemented using an optical lever. J Appl Phys 65:164–167

Amelio S, Goldade AV, Rabe U, Scherer V, Bhushan B, Arnold W (2001) Measurements of mechanical properties of ultra-thin diamond-like carbon coatings using atomic force acoustic microscopy. Thin Solid Films 392:75–84

Anczykowski B, Krueger D, Babcock KL, Fuchs H (1996) Basic properties of dynamic force spectroscopy with the scanning force microscope in experiment and simulation. Ultramicroscopy 66:251–259

Andoh Y, Oguchi S, Kaneko R, Miyamoto T (1992) Evaluation of very thin lubricant films. J Phys D Appl Phys 25:A71–A75

Ashcroft NW, Mermin ND (1976) Solid state physics. Holt Reinhart and Winston, New York

Avila A, Bhushan B (2010) "Electrical measurement techniques in atomic force microscopy", (Invited). Crit Rev Solid State Mater Sci 35:38–51

Barbara PF, Adams DM, O'Connor DB (1999) Characterization of organic thin film materials with near-field scanning optical microscopy (NSOM). Annu Rev Mater Sci 29:433–469

Barrett RC, Quate CF (1991) Optical scan-correction system applied to atomic force microscopy. Rev Sci Instrum 62:1393

Basire C, Ivanov DA (2000) Evolution of the lamellar structure during crystallization of a semicrystalline-amorphous polymer blend: time-resolved hot-stage SPM study. Phys Rev Lett 85:5587–5590

Baumeister T, Marks SL (1967) Standard handbook for mechanical engineers, 7th edn. McGraw-Hill, New York

Betzig E, Troutman JK, Harris TD, Weiner JS, Kostelak RL (1991) Breaking the diffraction barrier—optical microscopy on a nanometric scale. Science 251:1468–1470

Betzig E, Finn PL, Weiner JS (1992) Combined shear force and near-field scanning optical microscopy. Appl Phys Lett 60:2484

Bhushan B (1995) Micro/nanotribology and its applications to magnetic storage devices and MEMS. Tribol Int 28:85–96

Bhushan B (1997) Micro/nanotribology and its applications, vol E330. Kluwer Academic Pub, Dordrecht, Netherlands

Bhushan B (1999a) Handbook of micro/nanotribology, 2nd edn. CRC Press, Boca Raton, Florida

Bhushan B (1999b) Wear and mechanical characterisation on micro-to picoscales using AFM. Int Mat Rev 44:105–117

Bhushan B (2001a) Modern tribology handbook, Vol. 1: principles of tribology. CRC Press, Boca Raton, Florida

Bhushan B (2001b) Fundamentals of tribology and bridging the gap between the macro- and micro/nanoscales. NATO Science Series II, vol 10. Kluwer Academic Pub., Dordrecht, Netherlands

Bhushan B (2001c) Nano- to microscale wear and mechanical characterization studies using scanning probe microscopy. Wear 251:1105–1123

Bhushan B (2005) Nanotribology and nanomechanics. Wear 259:1507–1531

Bhushan B (2008) Nanotribology, nanomechanics and nanomaterials characterization. Phil Trans R Soc A 366:1351–1381

Bhushan B (2010–2013) Scanning probe microscopy in nanoscience and nanotechnology, vols 1–3. Springer, Heidelberg, Germany

Bhushan B (2011) Nanotribology and Nanomechanics I & II, 3rd edn. Springer, Heidelberg, Germany

Bhushan B (2013a) Principles and applications of tribology, 2nd edn. Wiley, New York

Bhushan B (2013b) Introduction to tribology, 2nd edn. Wiley, New York

Bhushan B, Blackman GS (1991) Atomic force microscopy of magnetic rigid disks and sliders and its applications to tribology. ASME J Tribol 113:452–458

Bhushan B, Dandavate C (2000) Thin-film friction and adhesion studies using atomic force microscopy. J Appl Phys 87:1201–1210

Bhushan B, Fuchs H (2006) Applied scanning probe methods II—scanning probe microscopy techniques, III—characterization, and IV—industrial applications. Springer, Heidelberg, Germany

Bhushan B, Fuchs H (2007) Applied scanning probe methods VII—biomimetics and industrial applications. Springer, Heidelberg, Germany

Bhushan B, Fuchs H (2009) Applied scanning probe methods XI—scanning probe microscopy techniques; XII—characterization; and XIII—biomimetics and industrial applications. Springer, Heidelberg, Germany

Bhushan B, Goldade AV (2000) Measurements and analysis of surface potential change during wear of single-crystal silicon (100) at ultralow loads using Kelvin probe microscopy. Appl Surf Sci 157:373–381

Bhushan B, Kawata S (2007) Applied scanning probe methods VI—characterization. Springer, Heidelberg, Germany

Bhushan B, Koinkar VN (1994) Nanoindentation hardness measurements using atomic force microscopy. Appl Phys Lett 75:5741–5746

Bhushan B, Qi J (2003) Phase contrast imaging of nanocomposites and molecularly-thick lubricant films in magnetic media. Nanotechnology 14:886–895

Bhushan B, Ruan J (1994) Atomic-scale friction measurements using friction force microscopy: Part II—application to magnetic media. ASME J Tribol 116:389–396

Bhushan B, Sundararajan S (1998) Micro/nanoscale friction and wear mechanisms of thin films using atomic force and friction force microscopy. Acta Mater 46:3793–3804

Bhushan B, Ruan J, Gupta BK (1993) A scanning tunnelling microscopy study of fullerene films. J Phys D Appl Phys 26:1319–1322

Bhushan B, Koinkar VN, Ruan J (1994) Microtribology of magnetic media. Proc Inst Mech Eng Part J: J Eng Tribol 208:17–29

Bhushan B, Israelachvili JN, Landman U (1995) Nanotribology: friction, wear, and lubrication at the atomic scale. Nature 374:607–616

Bhushan B, Kulkarni AV, Bonin W, Wyrobek JT (1996) Nano/Picoindentation measurements using capacitive transducer in atomic force microscopy. Philos Mag A 74:1117–1128

Bhushan B, Fuchs H, Hosaka S (2004) Applied scanning probe methods. Springer, Heidelberg, Germany

Bhushan B, Fuchs H, Kawata S (2007) Applied scanning probe methods V—scanning probe microscopy techniques. Springer, Heidelberg, Germany

Bhushan B, Fuchs H, Tomitori M (2008) Applied scanning probe methods VIII—scanning probe microscopy techniques; IX—characterization; and X—biomimetics and industrial applications. Springer, Heidelberg, Germany

Binggeli M, Christoph R, Hintermann HE, Colchero J, Marti O (1993) Friction force measurements on potential controlled graphite in an electrolytic environment. Nanotechnology 4:59–63

Binnig G (1992) Force microscopy. Ultramicroscopy 42–44:7–15

Binnig G, Rohrer H (1983) Scanning tunnelling microscopy. Surf Sci 126:236–244

Binnig G, Smith DPE (1986) Single-tube three-dimensional scanner for scanning tunneling microscopy. Rev Sci Instrum 57:1688

Binnig G, Rohrer H, Gerber C, Weibel E (1982) Surface studies by scanning tunneling microscopy. Phys Rev Lett 49:57–61

Binnig G, Quate CF, Gerber Ch (1986) Atomic force microscope. Phys Rev Lett 56:930–933

Binnig G, Gerber Ch, Stoll E, Albrecht TR, Quate CF (1987) Atomic resolution with atomic force microscope. Europhys Lett 3:1281–1286

Blackman GS, Mate CM, Philpott MR (1990) Interaction forces of a sharp tungsten tip with molecular films on silicon surface. Phys Rev Lett 65:2270–2273

Bonnell DA (ed) (1993) Scanning tunneling microscopy and spectroscopy—theory, techniques, and applications. VCH, New York

Burham NA, Colton RJ, Pollock HM (1991) Interpretation issues in force microscopy. J Vac Sci Technol A 9:2548–2556

Burnham NA, Colton RJ (1989) Measuring the nanomechanical properties and surface forces of materials using an atomic force microscope. J Vac Sci Technol A 7:2906–2913

Burnham NA, Domiguez DD, Mowery RL, Colton RJ (1990) Probing the surface forces of monolayer films with an atomic force microscope. Phys Rev Lett 64:1931–1934

Carr RG (1988) Finite element analysis of PZT tube scanner motion for scanning tunneling microscopy. J Microsc 152:379–385

Chen CJ (1992a) In situ testing and calibration of tube piezoelectric scanners. Ultramicroscopy 42–44:1653–1658

Chen CJ (1992b) Electromechanical deflections of piezoelectric tubes with quartered electrodes. App Phys Lett 60:132

Cleveland JP, Manne S, Bocek D, Hansma PK (1993) A nondestructive method for determining the spring constant of cantilevers for scanning force microscopy. Rev Sci Instrum 64:403–405

Colchero J (1993) Reibungskraftmikroskopie, Ph.D. Dissertation, Physics Faculty, University of Konstanz, Konstanz, Germany

Colchero J, Marti O, Bielefeldt H, Mlynek J (1991) Scanning force and friction microscopy. Phys Stat Sol 131:73–75

Cooley JW, Tukey JW (1965) An algorithm for machine calculation of complex fourier series. Math Comput 19:297

Coombs JH, Pethica JB (1986) Properties of vacuum tunneling currents: anomalous barrier heights. IBM J Res Dev 30:455–459

Dai HJ, Hafner JH, Rinzler AG, Colbert DT, Smalley RE (1996) Nanotubes as nanoprobes in scanning probe microscopy. Nature 384:147–150

Delawski E, Parkinson BA (1992) Layer-by-layer etching of two-dimensional metal chalcogenides with the atomic force microscope. J Am Chem Soc 114:1661–1667

den Boef AJ (1991) The influence of lateral forces in scanning force microscopy. Rev Sci Instrum 62:88–92

DeVecchio D, Bhushan B (1997) Localized surface elasticity measurements using an atomic force microscope. Rev Sci Instrum 68:4498–4505

DeVecchio D, Bhushan B (1998) Use of a nanoscale kelvin probe for detecting wear precursors. Rev Sci Instrum 69:3618–3624

Drake B, Prater CB, Weisenhorn AL, Gould SAC, Albrecht TR, Quate CF, Cannell DS, Hansma HG, Hansma PK (1989) Imaging crystals, polymers and processes in water with the atomic force microscope. Science 243:1586–1589

Durig U, Zuger O, Stalder A (1992) Interaction force detection in scanning probe microscopy: methods and applications. J Appl Phys 72:1778–1797

Durselen R, Grunewald U, Preuss W (1995) Calibration and applications of a high precision piezo scanner for nanometrology. Scanning 17:91–96

Eigler DM, Schweizer EK (1990) Positioning single atoms with a scanning tunnelling microscope. Nature 344:524–528

Erlandsson R, McClelland GM, Mate CM, Chiang S (1988) Atomic force microscopy using optical interferometry. J Vac Sci Technol A 6:266–270

Foster J, Frommer J (1988) Imaging of liquid crystal using a tunneling microscope. Nature 333: 542–547

Frisbie CD, Rozsnyai LF, Noy A, Wrighton MS, Lieber CM (1994) Functional group imaging by chemical force microscopy. Science 265:2071–2074

Frommer J (1992) Scanning tunneling microscopy and atomic force microscopy in organic chemistry. Angew Chem Int Ed Engl 31:1298–1328

Fu J (1995) In situ testing and calibrating of Z-Piezo of an atomic force microscope. Rev Sci Instrum 66:3785–3788

Fuchs H, Bhushan B (2010) Biosystems—investigated by scanning probe microscopy. Springer, Heidelberg, Germany

Fujisawa S, Ohta M, Konishi T, Sugawara Y, Morita S (1994a) Difference between the forces measured by an optical lever deflection and by an optical interferometer in an atomic force microscope. Rev Sci Instrum 65:644–647

Fujisawa S, Kishi E, Sugawara Y, Morita S (1994b) Fluctuation in 2-dimensional stick-slip phenomenon observed with 2-dimensional frictional force microscope. Jpn J Appl Phys (Part 1) 33:3752–3755

Garcìa Cantù R, Huerta Garnica MA (1990) Long-scan imaging by STM. J Vac Sci Technol A 8:354

Gerber C, Marti O (1985) Magnetostrictive positioner. IBM Tech Discl Bull 27:6373

Giaever I (1960) Energy gap in superconductors measured by electron tunneling. Phys Rev Lett 5:147–148

Giessibl FJ (1995) Atomic resolution of the silicon (111)-(7×7) surface by atomic force microscopy. Science 267:68–71

Giessibl FJ, Gerber Ch, Binnig G (1991) A low-temperature atomic force/scanning tunneling microscope for ultrahigh vacuum. J Vac Sci Technol B 9:984–988

Giessibl FJ, Sugawara Y, Morita S, Hosoi H, Sueoka K, Mukasa K, Sasahara A, Onishi H (2011) Noncontact atomic force microscopy and related topics. In: Bhushan B (ed) Nanotriology and nanomechanics I, 3rd edn. Springer, Heidelberg, Germany, pp 195–237

Goddenhenrich T, Lemke H, Hartmann U, Heiden C (1990) Force microscope with capacitive displacement detection. J Vac Sci Technol A 8:383–387

Grafstrom S, Ackermann J, Hagen T, Neumann R, Probst O (1994) Analysis of lateral force effects on the topography in scanning force microscopy. J Vac Sci Technol B 12:1559–1564

Griffith JE, Miller GL, Green CA (1990) A scanning tunneling microscope with a capacitance-based position monitor. J Vac Sci Technol B 8:2023–2027

Guntherodt HJ, Wiesendanger R (eds) (1992) Scanning tunneling microscopy I: general principles and applications to clean and adsorbate-covered surfaces. Springer, Berlin

Guntherodt HJ, Anselmetti D, Meyer E (eds) (1995) Forces in scanning probe methods, vol E286. Kluwer Academic Publishers, Dordrecht, Netherlands

Hafner JH, Cheung CL, Woolley AT, Lieber CM (2001) Structural and functional imaging with carbon nanotube AFM probes. Prog Biophys Mol Biol 77:73–110

Hansma PK, Tersoff J (1987) Scanning tunneling microscopy. J Appl Phys 61:R1–R23

Hansma PK, Drake B, Marti O, Gould SAC, Prater CB (1989) The scanning ion-conductance microscope. Science 243:641–643

Hartmann U (1999) Magnetic force microscopy. Annu Rev Mater Sci 29:53–87

Holman AE, Laman CD, Scholte PMLO, Heerens WC, Tuinstra F (1996) A calibrated scanning tunneling microscope equipped with capacitive sensors. Rev Sci Instrum 67:2274–2280

Hug HJ, Moser A, Jung Th, Fritz O, Wadas A, Parashikor I, Guntherodt HJ (1993) Low temperature magnetic force microscopy. Rev Sci Instrum 64:2920–2925

Husser OE, Craston DH, Bard AJ (1989) Scanning electrochemical microscopy—high resolution deposition and etching of materials. J Electrochem Soc 136:3222–3229

Ibe JP, Bey PP, Brandon SL, Brizzolara RA, Burnham NA, DiLella DP, Lee KP, Marrian CRK, Colton RJ (1990) On the electrochemical etching of tips for scanning tunneling microscopy. J Vac Sci Technol A 8:3570–3575

Jarvis SP, Oral A, Weihs TP, Pethica JB (1993) A novel force microscope and point contact probe. Rev Sci Instrum 64:3515–3520

Kaneko R, Oguchi S (1990) Ion-implanted diamond tip for a scanning tunneling microscope. Jap J Appl Phys 28:1854–1855

Kasai T, Bhushan B, Huang L, Su C (2004) Topography and phase imaging using the torsional resonance mode. Nanotechnology 15:731–742

Kassing R, Oesterschulze E (1997) Sensors for scanning probe microscopy. In: Bhushan B (ed) Micro/nanotribology and its applications. Kluwer Academic Publishers, Dordrecht, Netherlands, pp 35–54

Kirk MD, Albrecht T, Quate CF (1988) Low-temperature atomic force microscopy. Rev Sci Instrum 59:833–835

Kobayashi A, Grey F, Williams RS, Ano M (1993) Formation of nanometer-scale grooves in silicon with a scanning tunneling microscope. Science 259:1724–1726

Koinkar VN, Bhushan B (1996) Microtribological studies of unlubricated and lubricated surfaces using atomic force/friction force microscopy. J Vac Sci Technol A 14:2378–2391

Krotil U, Stifter T, Waschipky H, Weishaupt K, Hild S, Marti O (1999) Pulse force mode: a new method for the investigation of surface properties. Surf Interface Anal 27:336–340

Lee DT, Pelz JP, Bhushan B (2002) Instrumentation for direct, low frequency scanning capacitance

microscopy, and analysis of position dependent stray capacitance. Rev Sci Instrum 73:3523–3533
Leung OM, Goh MC (1992) Orientation ordering of polymers by atomic force microscope tip-surface interactions. Science 225:64–66
Libioulle N, Ronda A, Taborelli M, Gilles JM (1991) Deformations and nonlinearity in scanning tunneling microscope images. J Vac Sci Technol B 9:655–658
Liu H, Bhushan B (2002) Investigation of nanotribological properties of self-assembled monolayers with alkyl and biphenyl spacer chains. Ultramicroscopy 91:185–202
Lyo IW, Avouris Ph (1991) Field-induced nanometer-to-atomic-scale manipulation of silicon surfaces with the STM. Science 253:173–176
Maivald P, Butt HJ, Gould SAC, Prater CB, Drake B, Gurley JA, Elings VB, Hansma PK (1991) Using force modulation to image surface elasticities with the atomic force microscope. Nanotechnology 2:103–106
Majumdar A (1999) Scanning thermal microscopy. Annu Rev Mater Sci 29:505–585
Majumdar A, Oden PI, Carrejo JP, Nagahara LA, Graham JJ, Alexander J (1992) Nanometer-scale lithography using the atomic force microscope. Appl Phys Lett 61:2293–2295
Marti O, Amrein M (eds) (1993) STM and SFM in biology. Academic Press, San Diego
Marti O, Drake B, Hansma PK (1987) Atomic force microscopy of liquid-covered surfaces: atomic resolution images. Appl Phys Lett 51:484–486
Marti O, Gould S, Hansma PK (1988) Control electronics for atomic force microscopy. Rev Sci Instrum 59:836–839
Marti O, Colchero J, Mlynek J (1990) Combined scanning force and friction microscopy of mica. Nanotechnology 1:141–144
Martin Y, Wickramasinghe HK (1987) Magnetic imaging by force microscopy with 1000 Å resolution. Appl Phys Lett 50:1455–1457
Martin Y, Williams CC, Wickramasinghe HK (1987) Atomic force microscope-force mapping and profiling on a sub 100-Å scale. J Appl Phys 61: 4723–4729
Martin Y, Abraham DW, Wickramasinghe HK (1988) High-resolution capacitance measurement and potentiometry by force microscopy. Appl Phys Lett 52:1103–1105
Mate CM (1992) Atomic-force-microscope study of polymer lubricants on silicon surfaces. Phys Rev Lett 68:3323–3326
Mate CM, McClelland GM, Erlandsson R, Chiang S (1987) Atomic-scale friction of a tungsten tip on a graphite surface. Phys Rev Lett 59:1942–1945
Matey J, Blanc J (1985) Scanning capacitance microscopy. J Appl Phys 57:1437–1444
McClelland GM, Erlandsson R, Chiang S (1987) Atomic force microscopy: general principles and a new implementation. In: Thompson DO, Chimenti DE (eds) Review of progress in quantitative nondestructive evaluation, vol 6B, Plenum, New York, pp 1307–1314
Meyer E (1992) Atomic force microscopy. Surf Sci 41:3–49
Meyer G, Amer NM (1988) Novel optical approach to atomic force microscopy. Appl Phys Lett 53:1045–1047
Meyer G, Amer NM (1990a) Optical-beam-deflection atomic force microscopy: the NaCl (001) surface. Appl Phys Lett 56:2100–2101
Meyer G, Amer NM (1990b) Simultaneous measurement of lateral and normal forces with an optical-beam-deflection atomic force microscope. Appl Phys Lett 57:2089–2091
Meyer E, Overney R, Luthi R, Brodbeck D et al (1992) Friction force microscopy of mixed Langmuir-Blodgett films. Thin Solid Films 220:132–137
Neubauer G, Coben SR, McClelland GM, Horne D, Mate CM (1990) Force microscopy with a bidirectional capacitance sensor. Rev Sci Instrum 61:2296–2308
Nicolaides RL, Yong WE, Packard WF, Zhou HA et al (1988) Scanning tunneling microscope tip structures. J Vac Sci Technol A 6:445–447
Nonnenmacher M, O'Boyle MP, Wickramasinghe HK (1991) Kelvin probe force microscopy. Appl Phys Lett 58:2921–2923
O'Shea SJ, Welland ME, Rayment T (1992) Atomic force microscope study of boundary layer lubrication. Appl Phys Lett 61:2240–2242
Ohnesorge F, Binnig G (1993) True atomic resolution by atomic force microscopy through repulsive and attractive forces. Science 260:1451–1456
Overney RM, Takano H, Fujihira M, Paulus W, Ringsdorf H (1994) Anisotropy in friction and molecular stick-slip motion. Phys Rev Lett 72:3546–3549
Palacio M, Bhushan B (2010) Normal and lateral force calibration techniques for AFM cantilevers. Crit Rev Solid State 35:73–104
Park SI, Quate CF (1987) Digital filtering of STM images. J Appl Phys 62:312
Parkinson B (1990) Layer-by-layer nanometer scale etching of two-dimensional substrates using the scanning tunneling microscopy. J Am Chem Soc 112:7498–7502
Pohl DW (1986) Some design criteria in STM. IBM J Res Dev 30:417
Pohl DW, Denk W, Lanz M (1984) Optical stethoscopy-image recording with resolution lambda/20. Appl Phys Lett 44:651–653
Prater CB, Hansma PK, Tortonese M, Quate CF (1991) Improved scanning ion-conductance microscope using microfabricated probes. Rev Sci Instrum 62:2634–2638
Rabe U, Janser K, Arnold W (1996) Vibrations of free and surface-coupled atomic force microscope: theory and experiment. Rev Sci Instrum 67:3281–3293
Radmacher M, Tillman RW, Fritz M, Gaub HE (1992) From molecules to cells: imaging soft samples with the atomic force microscope. Science 257: 1900–1905
Reinstaedtler M, Rabe U, Scherer V, Hartmann U, Goldade A, Bhushan B, Arnold W (2003) On the

nanoscale measurement of friction using atomic force microscope cantilever torsional resonances. Appl Phys Lett 82:2604–2606
Reinstaedtler M, Kasai T, Rabe U, Bhushan B, Arnold W (2005) Imaging and measurement of elasticity and friction using the TR mode. J Phys D Appl Phys 38: R269–R282
Ruan J, Bhushan B (1994a) Atomic-scale friction measurements using friction force microscopy: part I—general principles and new measurement techniques. ASME J Tribol 116:378–388
Ruan J, Bhushan B (1994b) Atomic-scale and microscale friction of graphite and diamond using friction force microscopy. J Appl Phys 76:5022–5035
Rugar D, Hansma PK (1990) Atomic force microscopy. Phys Today 43:23–30
Rugar D, Mamin HJ, Guethner P (1989) Improved fiber-optical interferometer for atomic force microscopy. Appl Phys Lett 55:2588–2590
Rugar D, Mamin HJ, Guethner P, Lambert SE, Stern JE, McFadyen I, Yogi T (1990) Magnetic force microscopy—general principles and application to longitudinal recording media. J Appl Phys 63:1169–1183
Sarid D (1991) Scanning force microscopy. Oxford University Press, New York
Sarid D, Elings V (1991) Review of scanning force microscopy. J Vac Sci Technol B 9:431–437
Sarid D, Iams D, Weissenberger V, Bell LS (1988) Compact scanning-force microscope using laser diode. Opt Lett 13:1057–1059
Scherer V, Bhushan B, Rabe U, Arnold W (1997) Local elasticity and lubrication measurements using atomic force and friction force microscopy at ultrasonic frequencies. IEEE Trans Mag 33:4077–4079
Scherer V, Arnold W, Bhushan B (1999) Lateral force microscopy using acoustic friction force microscopy. Surf Interface Anal 27:578–587
Schirmeisen A, Anczykowski B, Hoelscher H, Fuchs F (2011) Dynamic modes of atomic force microscopy. In: Bhushan B (ed) Nanotriology and nanomechanics I, 3rd edn. Springer, Heidelberg, Germany, pp 307–353
Schoenenberger C, Alvarado SF (1989) A differential interferometer for force microscopy. Rev Sci Instrum 60:3131–3135
Schoenenberger C, Alvarado SF (1990) Understanding magnetic force microscopy. Z Phys B 80:373–383
Shen YR (1984) The principles of nonlinear optics. Wiley, New York
Silver RM, Ehrichs EE, de Lozanne AL (1987) Direct writing of submicron metallic features with a scanning tunnelling microscope. Appl Phys Lett 51:247–249
Smith D, Horber H, Gerber C, Binnig G (1989) Smectic liquid crystal monolayers on graphite observed by scanning tunneling microscopy. Science 245:43–45
Smith D, Horber J, Binnig G, Nejoh H (1990) Structure, registry and imaging mechanism of alkyl-cyanobiphenyl molecules by tunnelling microscopy. Nature 344:641–644
Stahl U, Yuan CW, Delozanne AL, Tortonese M (1994) Atomic force microscope using piezoresistive cantilevers and combined with a scanning electron microscope. Appl Phys Lett 65:2878–2880
Stern JE, Terris BD, Mamin HJ, Rugar D (1988) Deposition and imaging of localized charge on insulator surfaces using a force microscope. Appl Phys Lett 53:2717–2719
Stoll EP (1991) Restoration of STM images distorted by time-dependent piezo driver aftereffects. Ultramicroscopy 42–44:1585–1589
Stroscio JA, Kaiser WJ (eds) (1993) Scanning tunneling microscopy. Academic Press, Boston
Thomson WT, Dahleh MD (1998) Theory of vibration with applications, 5th Edn. Prentice Hall, Upper Saddle River, New Jersey
Toledo-Crow R, Yang PC, Chen Y, Vaez-Iravani M (1992) Near-field differential scanning optical microscope with atomic force regulation. Appl Phys Lett 60:2957–2959
Tsau L, Wang D, Wang KL (1994) Nanometer scale patterning of silicon (100) surface by an atomic force microscope operating in air. Appl Phys Lett 64:2133–2135
Warmack RJ, Zheng XY, Thundat T, Allison DP (1994) Friction effects in the deflection of atomic force microscope cantilevers. Rev Sci Instrum 65:394–399
Weaver JMR, Abraham DW (1991) High resolution atomic force microscopy potentiometry. J Vac Sci Technol B 9:1559–1561
Weisenhorn AL, MacDougall JE, Gould JAC, Cox SD, Wise WS, Massie J, Maivald P, Elings VB, Stucky GD, Hansma PK (1990) Imaging and manipulating of molecules on a zeolite surface with an atomic force microscope. Science 247:1330–1333
Weisenhorn AL, Egger M, Ohnesorge F, Gould SAC, Heyn SP, Hansma HG, Sinsheimer RL, Gaub HE, Hansma PK (1991) Molecular resolution images of Langmuir-Blodgett films and DNA by atomic force microscopy. Langmuir 7:8–12
Wickramasinghe HK (2000) Progress in scanning probe microscopy. Acta Mater 48:347–358
Wiesendanger R, Guntherodt HJ (eds) (1992) Scanning tunneling microscopy, II: further applications and related scanning techniques. Springer, Berlin
Williams CC (1999) Two-dimensional dopant profiling by scanning capacitance microscopy. Annu Rev Mater Sci 29:471–504
Williams CC, Wickramasinghe HK (1986) Scanning thermal profiler. Appl Phys Lett 49:1587–1589
Williams CC, Wickramasinghe HK (1990) Microscopy of chemical-potential variations on an atomic scale. Nature 344:317–319
Wolter O, Bayer T, Greschner J (1991) Micromachined silicon sensors for scanning force microscopy. J Vac Sci Technol B 9:1353–1357

Yamanaka K, Tomita E (1995) Lateral force modulation atomic force microscope for selective imaging of friction forces. Jpn J Appl Phys 34:2879–2882

Yamanaka K, Ogisco H, Kolosov O (1994) Ultrasonic force microscopy for nanometer resolution subsurface imaging. Appl Phys Lett 64:178–180

Young R, Ward J, Scire F (1971) Observation of metal-vacuum-metal tunneling, field emission, and the transition region. Phys Rev Lett 27:922

Young R, Ward J, Scire F (1972) The Topographiner: an instrument for measuring surface microtopography. Rev Sci Instrum 43:999

http://www.springer.com/978-3-319-51432-1

Nanotribology and Nanomechanics
An Introduction
Bhushan, B. (Ed.)
2017, XVI, 928 p. 656 illus., 156 illus. in color.,
Hardcover
ISBN: 978-3-319-51432-1